Università degli Studi di Cagliari

# DOTTORATO DI RICERCA

Scienze e Tecnologie Chimiche

Ciclo XXX

## TITOLO TESI

**Chemical Recycling of Carbon Dioxide to Chemicals and Fuels**

Settore scientifico disciplinare di afferenza

CHIM/04

| | |
|---|---|
| Presentata da: | Luciano Atzori |
| Coordinatore Dottorato | Prof. Stefano Enzo |
| Tutor | Dott.ssa Elisabetta Rombi |

Esame finale anno accademico 2016 – 2017
Tesi discussa nella sessione d'esame Marzo 2018

Università degli Studi di Cagliari

Corso di Dottorato di ricerca in

"Scienze e Tecnologie Chimiche"

## Acknowledgments

**Foreword**

The increasing attention toward climate changes is promoting research in the development of suitable strategies for $CO_2$ emissions mitigation. Among these, *Carbon Capture and Utilisation* technologies (CCUs) appear as the most promising, as they permit to reduce the carbon dioxide emitted in atmosphere, at same time preserving natural resources for the future generations, so as to meet the criteria of sustainability. However, since CCUs require energy, carbon dioxide utilisation cannot be considered sustainable at priori, and the implementation of technologies making use of renewable energy is needed. Currently, the amount of carbon dioxide consumed in chemical recycling processes represents a very small fraction of the total emissions, thus a net increase in $CO_2$ exploitation through the development of efficient processes and catalysts is required.

In this context, the present work deals with the study of different processes aiming to convert $CO_2$ into cyclic carbonates, methane, and methanol, which can cover a very important role in terms of CCUs impact. Cyclic carbonates, produced by $CO_2$ cycloaddition to epoxides, find wide use in numerous technological and industrial applications, while the synthesis of methane and methanol through $CO_2$ hydrogenation are considered as promising processes in order to get viable alternatives to fossil fuels.

For each process, suitable heterogeneous catalysts have been prepared and extensively characterised by means of different techniques.

The work has been mainly carried out at the Laboratory of Industrial Chemistry, at the Department of Chemical and Geological Sciences of the University of Cagliari. Catalytic tests for the $CO_2$ conversion to cyclic carbonates were carried out under the supervision of Prof. Carmela Aprile at the University of Namur (Belgium). Methanation processes were studied at the Laboratory of Industrial Chemistry in Cagliari, while those for the $CO_2$ hydrogenation to methanol were performed in the Laboratories of the SOTACARBO S.p.A. in Carbonia (Cagliari, Italy).

This thesis is structured as follows: after an introduction (*Chapter I*) on the main strategies viable for alleviating $CO_2$ emissions, *Chapter II* is dedicated to the description of the adopted preparation and characterisation techniques, as well as to the description of the catalytic tests. *Chapter III* is devoted to the study of the $CO_2$ cycloaddition reaction to epoxides. In *Chapter IV* the work on the methanation process is described, while in *Chapter V* the results on the $CO_2$ to methanol processes are discussed. Finally, general *Conclusions and Perspectives* on the entire work are given.

# Summary

# Chapter I


# *Introduction*

## 1.1. Carbon dioxide emissions and Sustainability

Several studies have clearly stated the connection between the greenhouse gases (GHGs) emissions and the climate system [1]. Carbon dioxide ($CO_2$) is estimated to account for 77% of GHGs emissions and is thus considered the main cause of climate change. The major contribution to this massive emission of $CO_2$ can be associated with the use of carbon-based fuels that currently provide about 80-85 % of the global *Total Primary Energy Supply* (TPES) [2,3]. Since the Industrial Revolution, the annual $CO_2$ emissions have dramatically increased from near zero to about 34 $Gt_{CO_2}$ in 2014 (Fig. 1.1) and, as a consequence, the atmospheric concentration of $CO_2$ has currently achieved the value of 400 ppm [4].
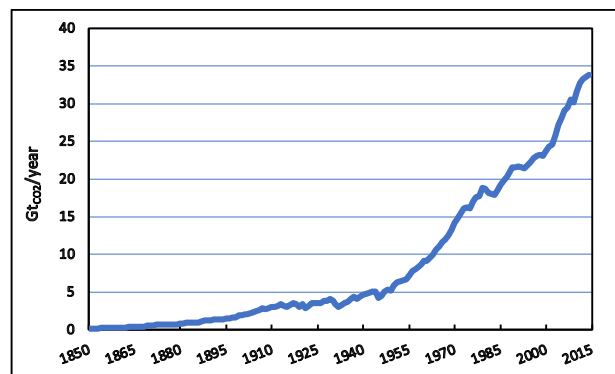


**Fig. 1.1.** Trend in $CO_2$ emissions from fossil fuel combustion.

Such $CO_2$ concentration is also expected to increase in the next decades, especially because of the robust economic growth of emerging economies, such as China and India, which are today the biggest energy consumers, together with USA. Moreover, it is worthy of note that these emerging countries have an unfavourable energy structure dominated by coal, which is the most impacting raw material from an environmental point of view, as its combustion produces the highest $CO_2$ amount per unit of heat compared to the other carbon-based fuels [5,6].

Although a clear future trend about $CO_2$ emissions cannot be estimated, due to the unpredictable economy evolution for some countries in large areas of the Earth (including Eastern Europe and Russia, Southern America, other Asian countries in addition to China and India, and almost the whole Africa), it can be reasonably foretold that a rise in carbon dioxide

emissions up to 50-60 $Gt_{CO_2}$/year will happen in the next years, bringing the actual atmospheric concentration of $CO_2$ at the unsustainable value of 500 ppm within 2050 [7]. The *International Energy Agency* (IEA) and the *Intergovernmental Panel on Climate Change* (IPCC) pointed out the necessity to reduce the total anthropogenic $CO_2$ emissions to less than 20 $Gt_{CO_2}$/year by 2050, in order to avoid an increase in the global warming above 2 °C (*two-degree scenario* or 2DS), and therefore irreversible consequences for the ecosystem [8].

In the light of this alarming scenario, there is a need for a great effort from the scientific community, industries and governments in order to develop technologies and strategies that can contribute not only to mitigate the $CO_2$ emissions but also to preserve the natural resources of fossil fuels, making possible to meet the "sustainability" criteria. Sustainable development is defined as a way of "meeting the needs of current generations without compromising the ability of future generations to meet their own needs" [9]. In this light, social, economic, and especially environmental issues have to be taken into account as inseparable and interdependent components of the progress (Fig. 1.2).
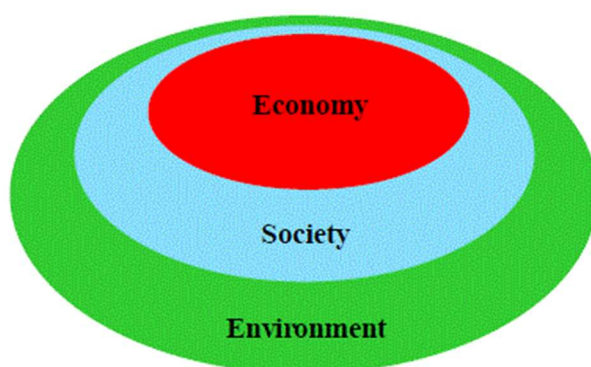


**Fig. 1.2.** The three aspects of the sustainable development.

Chemistry has played a primary function in the progress of our society. Today its role appears increasingly crucial for the development of strategies addressed to mitigate $CO_2$ emissions, since chemical processes are involved in technologies for its capture and utilisation. In particular, the concept of "Green Chemistry", defined for the first time in 1991 by Anastas and well described by the 12 principles of Green Chemistry, clearly highlights the prominent

necessity to design products and processes aiming at mitigating environmental issues and preserving natural resources [10].

A key concept of Green Chemistry is represented by the role of catalysis, which is also at the basis of efficient $CO_2$ conversion technologies, as will be discussed later. Catalysis is one the most important tools for the implementation of a sustainable production; in fact, the use of catalysts permits an energy requirement reduction (principle VI), an increase in selectivity (principle II), and a decrease in the use of processing and separation agents (principle V) [11,12].

## 1.2. CO₂ properties

Carbon dioxide is a gas at standard pressure and temperature, with a density of about 1.98 kg m$^{-3}$ at 0 °C. $CO_2$ has no liquid state at pressure below 5.1 bar and this is the reason why $CO_2$ sublimates at atmospheric pressure. By observing the p-T phase diagram (Fig. 1.3), it can be seen that $CO_2$ exists as supercritical fluid at relatively low pressure and temperature (critical point at 73.8 bar and 31 °C), making its use particularly interesting as a green solvent for catalytic reactions, chromatography, and extraction applications [13].
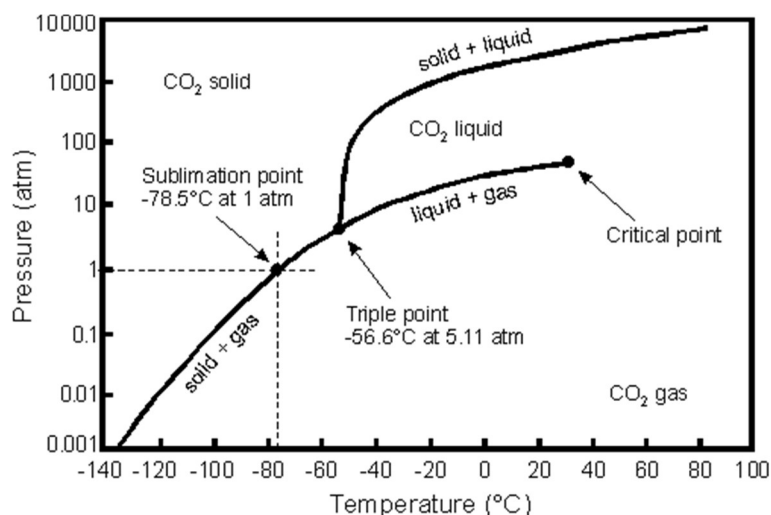


**Fig. 1.3.** p-T phase diagram of carbon dioxide.

Carbon dioxide is a non-flammable and relatively inert species and, together with water, is the final product of all the combustion processes that involve carbon- and hydrogen-containing molecules. Because of its properties, it is widely used in fire extinguishers and fire suppressing systems. $CO_2$ is naturally present in Earth's atmosphere as a consequence of volcanic eruptions, forest fires and plant and animal respiration. The natural carbon cycle has the ability to recycle about 203 $Gt_{CO_2}$/year; although man-made emissions account for only 7Gt per year, the natural carbon cycle is not able to recycle this apparently small excess, so that the concentration of $CO_2$ in atmosphere is building up (Fig. 1.4) [14].
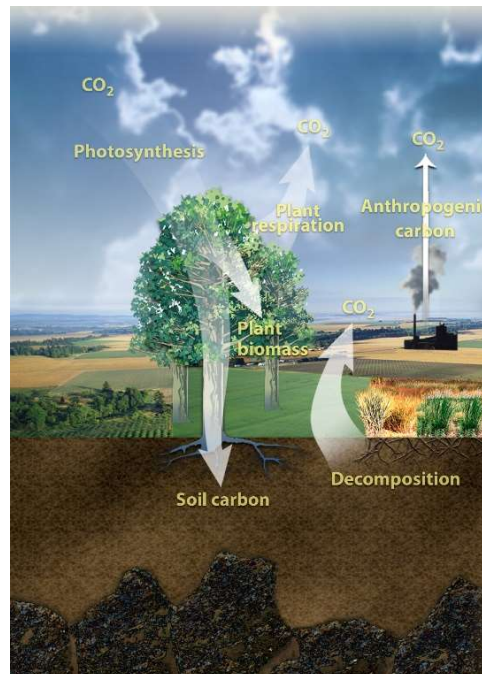


**Fig. 1.4.** Natural Carbon Cycle.

The infrared active vibrational modes of $CO_2$ (the anti-symmetric bending and stretching modes) are directly responsible for its role as a greenhouse gas [14]. The greenhouse effect is an important phenomenon for our planet since it permits to trap the solar energy, keeping the global temperature constant. However, a rise in GHGs concentration in Earth's atmosphere is leading to an increase in temperature with detrimental effects on our ecosystem. Although not the most potent greenhouse gas, $CO_2$ is known as the main responsible for global

warming, by virtue of its high concentration in the atmosphere compared to that of the other GHGs such as water vapour, methane and nitrous oxide [15].

The chemical reactivity of carbon dioxide is mainly dominated by two key features. The first is related to the polarization of the carbon-oxygen bonds, due to the higher electronegativity of oxygen in comparison with carbon; the central carbon of $CO_2$ can hence easily react with nucleophiles such as amines, phenolates, and Grignard's reagents. The second property is instead associated with the ability of some metals to coordinate carbon dioxide. Indeed, $CO_2$ can be coordinated by one or more metallic centres in different ways, that can involve either carbon or oxygen atoms. This feature is the basis for many metal-induced and metal-catalysed reactions in which carbon dioxide can be favourably activated for reacting with other species [16].

From a thermodynamic point of view, carbon dioxide is a very stable molecule with a heat of formation ($\Delta_f H°$) of -394 kJ mol$^{-1}$, thus its transformation is generally considered a challenging goal. However, there are a lot of exothermic reactions that makes $CO_2$ conversion perfectly feasible, such as, for example, the organic carbonates production (by reaction between $CO_2$ and epoxides) and the carbon dioxide hydrogenation into methane and methanol. Actually, equilibrium position in a reaction depends on the free energy value ($\Delta_f G° = \Delta_f H° - T\Delta_f S°$), which has to decrease in spontaneous processes; this means that changes in both entropy and enthalpy have to be considered. Chemical reactions involving carbon dioxide as the reactant are usually characterized by a decrease in entropy, as the process occurs with formation of liquids or solids, and sometimes it results in a decrease in the number of molecules. Accordingly, the process feasibility will be strictly dependent on the reaction temperature, in order to make $\Delta_f G° < 0$ and shift the equilibrium position towards the products [13].

Also for thermodynamically spontaneous processes which involve $CO_2$, kinetic aspects must be taken into account; indeed, a high activation energy barrier needs to be overcame in some cases to make reaction processes feasible. A remarkable decrease in activation energy can be obtained by using a suitable catalyst, which allows processes to be performed at reasonable temperatures. This also permits principles of "Green Chemistry" concerning catalysis to be met. In this light, a great effort from scientific community is needed, aiming at developing proper catalysts for each process related to $CO_2$ chemical recycle to chemicals and fuels.

## 1.3. Strategies for CO$_2$ emissions alleviation

Reduction of carbon dioxide emissions is a challenging global goal that requires the participation of different areas of research and the implementation of innovative strategies from governments and industries. Obviously, a unique solution to such a difficult problem does not exist; thus, different approaches are needed, which require to invest in several technologies in order to cover all the alternatives [17].

In principle, there are three possible strategies regarding the reduction of CO$_2$ emissions: mitigation of produced CO$_2$ by improvements in electric energy production and utilisation; *Carbon Capture and Storage* technologies (CCSs); *Carbon Capture and Utilisation* technologies (CCUs).

### 1.3.1. Direct reduction of emitted CO$_2$

A partial solution of the climatic issues due to the large amount of CO$_2$ emitted can be achieved by improvements in efficiency of electric energy production. For example, the use of an innovative technology, such as the *Integrated Gasification Combined Cycle* (IGCC), can bring the current average efficiency value of 30% to about 50%, with a useful contribution in reducing carbon dioxide emissions. Nevertheless, as the conversion of all the existing power plants is impossible, due to high costs and long implementation times, a more practicable strategy would be the design and construction of new low-emission power plants, even if some technological and economical aspects should be solved. In addition, from the point of view of natural resources exploitation, switching from coal towards less carbon-intensive feedstock, such as natural gas, can also be useful.

In addition, an improved efficiency in energy utilization would allow limiting emissions and preserving natural resources. In this respect, a better insulation of buildings, the use of more fuel-efficient vehicles, and a more diligent behaviour of people are all factors that can contribute to a more sustainable society [5].

### 1.3.2. Carbon Capture and Storage technologies

The amount of carbon dioxide emitted from industrial and utility plants plays a significant role in the climate change issues. The main sources of waste carbon dioxide are

listed in Tab. 1.1; the 2008 data highlight the prominent effect of power generation plants on the $CO_2$ global emissions, with the use of coal providing the largest contribution [18].

**Tab. 1.1.** Major sources of waste carbon dioxide.

| Source | 2008 global $CO_2$ emissions ($10^6$ t $CO_2$ per year) |
|---|---|
| Coal | 14200 |
| Natural gas | 6320 |
| Refineries | 850 |
| Cement production | 2000 |
| Iron and steel production | 1000 |
| Ethylene production | 260 |
| Ammonia production | 150 |

Carbon Capture and Storage (CCS) is defined as the removal of $CO_2$ directly from industrial punctual sources or atmosphere and its subsequent storage in geological sites, such as depleted oil and gas fields, aquifers, and coal beds [19]. Implementation of CCS technologies allows carbon dioxide to be stored away from the atmosphere for relatively long time, with obvious environmental benefits. CCSs permit today the storage of about 4.7 $Mt_{CO_2}$/year. However, some aspects still remain debated, especially due to the overall energy requirements for separation, pumping, and housing of $CO_2$. From this point of view, efficient pipeline systems are needed to transport $CO_2$ from the source points to the disposal location, the total cost of the system being affected by capacity and length of the pipelines [20,21]. Furthermore, the nature of the disposal sites must be carefully evaluated in order to ensure the storage of carbon dioxide for a long time. Lastly, a major challenge is the public acceptance, which will also condition political attitudes [22].

Since the applicability of the CCS strategies is strongly dependent on the cost of the $CO_2$ capture processes, some of the main used and studied capture agents will be detailed below.

### 1.3.2.1. Carbon Capture processes

Most of the capture agents currently used are based on liquid systems, either pure liquids, mixtures or solutions in solvents such as water. Different mechanisms can be at the

basis of gas-liquid separation, e.g. absorption and adsorption, for which the $CO_2$-capture agent interactions can be directed by physisorption or chemisorption. Commercially, solvents such as monoethanolamine (MEA) and diethanolamine (DEA) represent the most used compounds in $CO_2$ capture technologies. The chemical interaction between such species and $CO_2$ leads to the formation of a carbamate-ammonium ion pair, whereas the presence of -OH groups is considered crucial thanks to the establishment of hydrogen bonds which favour the $CO_2$ sorption. With monoethanolamine, the industrial process is performed at 50 °C and does not require high partial pressures of $CO_2$; however, MEA has to be used in solution with large amount of water (up to 70% w/w), which makes needed large plants, with a consequent increase in the initial capital expenditure (CAPEX). In addition, regeneration processes typically occur at 120 °C, making the costs increased [13]. Moreover, the high temperature of the desorption-regeneration processes brings to additional operational expenditure cost (OPEX), deriving from the chemical degradation of MEA with time, which makes indispensable a continuous replacement of the spent MEA with fresh solvent [23,24]. In addition, MEA decomposition can lead to the formation of compounds such as ammonia and aldehydes, which are more harmful to the environment than the captured $CO_2$, whereby post-stripper scrubbers could be needed.

Although MEA is the most widespread solvent for $CO_2$ capture, alternative compounds can be used. Poly-(ethylene glycol) dimethyl ether is a non-toxic and stable polymer that shows high $CO_2$ solubility and low vapour pressure; however, it suffers of some disadvantages such as high cost and hygroscopic properties [25].

Alkyl carbonates are an interesting class of compounds because they can adsorb carbon dioxide and they can be also produced from $CO_2$, with obvious positive effects in reducing their carbon footprint. Dimethyl carbonate (DMC) is a typical example, as it can be obtained by transesterification of cyclic carbonates, which in turn are produced by reaction between $CO_2$ and suitable epoxides. The adsorption capacity of DMC strictly depends on the capture conditions, and enhances with increasing pressures [26].

Recently, ionic liquids (ILs) have attracted growing attention as they exhibit very low vapor pressure and high polarity, are non-corrosive and resistant to chemical and thermal degradation. ILs characterised by the presence of amino groups are able to interact with carbon dioxide through the formation of C-N bonds, whose strength can be fine-tuned in order to increase the $CO_2$-uptake and to allow desorption processes to occur in relatively bland

conditions [27,28]. If compared to typical amine sorbents, ILs work at much lower $CO_2$-desorption temperature and can be used as pure liquids, allowing smaller size for the strippers. Since the high viscosity of ILs is probably the main technological disadvantage of these materials (diffusion-controlled mass transfer limitation), researches have been focused on porous solid polymers that have the typical properties of ionic liquids (P-ILs). In this respect, an interesting option is represented by the polymerisation of [VBMA][PF$_6$], a monomer with remarkable capturing properties, which is solid at room temperature (Fig. 1.5). The resulting polymer has the great benefit of being a porous solid that allows high $CO_2$-uptakes; in addition, being the capture mechanism based on physisorption, the desorption processes can be performed at relative low temperatures (about 80 °C). Nevertheless, even though P-ILs and ILs materials appear very promising for carbon dioxide capture processes, a wide utilisation is hindered by their high cost and lack of clear industrial scale-up proofs [13].
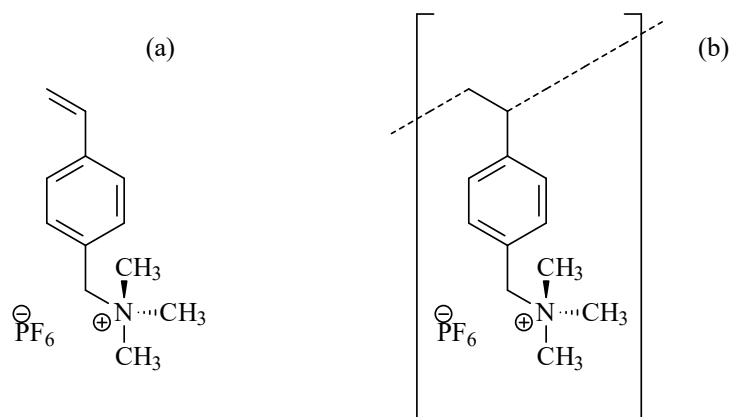


**Fig. 1.5.** Structures of [VBTMA][PF$_6$] (a) and its solid polymer P[VBMA][PF$_6$] (b).

Another important class of solid porous materials potentially suitable for capturing $CO_2$ are the Metal-Organics Frameworks (MOF). These materials have attracted great interest in the last decades thanks to their high surface area and controllable pore structure. In addition, functionalisation with amine can also be achieved to increase their adsorption capacities. MOFs exhibit remarkably $CO_2$ uptakes with pure carbon dioxide and high pressures, while they performance decreases drastically when they are exposed to a gas mixture [23,29,30].

### 1.3.3. Carbon Capture and Utilisation technologies

The carbon dioxide captured by using suitable capture agents can be converted through CCU technologies with the dual goal of reducing greenhouse emissions and, at same time, exploiting a waste such as carbon dioxide for technological and chemical applications. It is worth noting that CCUs and CCSs are not in conflict, but they are part of a family of technologies addressed to minimize $CO_2$ emissions into the atmosphere. Both are useful, although CCUs seems to be preferable, especially in the medium-long term [17]. In fact, $CO_2$ conversion into chemicals and fuels can help to meet the sustainability criteria, as it provides an effective strategy to preserve non-renewable fossil natural resources. Companies who decide to invest in CCU technologies would gain important benefits, such as improving the public image, decreasing costs for $CO_2$ disposal or obtaining emission reduction credits [31]. Notwithstanding, CCU technologies cannot be considered sustainable a priori. In this regard, an important distinction has to be done between "avoided" and "used" carbon dioxide [2]. Using $CO_2$ in chemical processes does not guarantee to avoid carbon dioxide emissions. Indeed, both capture and utilisation processes require energy (which is still largely derived from fossil sources), and the overall $CO_2$ production could thus be larger than its consumption. For this reason, perennial and renewable energy sources (such as solar, wind, hydro, and geothermal energy) should be preferentially used, and the sustainability of all chemicals involved in the utilisation process should be critically considered.

Even though technologies for $CO_2$ transformation already exist, the current consumption of carbon dioxide represents a minor fraction of the total emissions (0.62%), then a net increase in the conversion of "spent carbon" into "working carbon" is needed in order to make the extent of $CO_2$ exploitation significant. In general, carbon dioxide can be used in three different ways:

- technological applications;
- conversion into chemicals;
- conversion into fuels.

Continuous-point sources are probably the most suitable for CCU technologies, provided that facilities for $CO_2$ conversion are built in proximity of the source, thus limiting transport and storage costs. From this point of view, the capture of $CO_2$ from a relatively

constant source like atmosphere should be preferable, though $CO_2$ recovery is not easily practicable in this case, due to its low concentration in air [5].

It is worth highlighting that, depending on the CCU application, carbon dioxide feed requires particular specification in terms of concentration and impurities; in Tab. 1.2 such features are reported for the main emitting sources [13].

**Tab.1.2.** Features of the major $CO_2$ sources.

| Source | $CO_2$ concentrations (%) | Typical impurities |
|---|---|---|
| Power generation | 10-15 | $N_2$, $H_2O$, $SO_x$, $NO_x$ |
| Steel making | 18-20 | $N_2$, $SO_x$, $NO_x$, $O_2$ |
| Cement production | > 99 | $N_2$, $O_2$ |
| Fermentation | > 99 | $H_2O$, $H_2S$ |
| Natural gas streams | 0-8 | $N_2$, $O_2$, $H_2S$, $C_1$-$C_4$ hydrocarbons |
| Natural deposit | 90-100 | $N_2$, $O_2$, He |
| Atmosphere | 0.04 | $N_2$, $O_2$, $SO_x$, $NO_x$, particulates |

The presence of contaminants, such as $O_2$, $SO_x$, and $NO_x$, which are usually contained in the flue gases from power plants, might be deleterious since they can cause poisoning of the catalysts needed for the subsequent $CO_2$ conversion. In this context, the proper sources of carbon dioxide should be evaluated critically, as the required separation and purification processes can heavily affect the overall cost of the CCU technologies.

### 1.3.3.1. Use of $CO_2$ for technological applications

The utilisation of carbon dioxide in technological applications amounts to *ca.* 18Mt/year. A panoramic of the different industrial sectors in which $CO_2$ is used is listed in Tab. 1.3. Apart from water treatments and agricultural applications, technological uses do not convert carbon dioxide in other chemicals, thus it can be recycled at the end of the process and reused. For many of the applications reported in Tab. 1.3, $CO_2$ replaces inorganic and organic compounds with a significant reduction in the environmental impact, allowing the processes to be more sustainable [32].

**Tab. 1.3.** Technological uses of $CO_2$.

| Industrial sector | Use |
|---|---|
| Food industry | ● Food processing and conservation<br>● Carbonated beverages |
| Agriculture | ● Fumigating agent in silos<br>● Additive to irrigation water<br>● Uses in greenhouses |
| Water treatment | ● Neutralization of alkaline industrial effluent |
| Metal fabrication | ● Welding, moulding, manufacturing operations |
| Other applications | ● Rubber and plastic blowing agent<br>● Electronic industry, lasers, glass industry and fire extinguishers<br>● Refrigerators |

Other technological applications of $CO_2$ can be directly correlated to the relatively simple conditions in which it exists as a supercritical fluid. In particular, great benefits spring by the use of carbon dioxide as a solvent in substitution of harmful organic compounds. Supercritical carbon dioxide finds use in many chemical applications such as extraction of fragrances, decaffeination of coffee beans, dyeing, as a reactant or solvent, as an agent for polymers modification, material preparations, and waste treatments [14].

### 1.3.3.2. CO₂ conversion to chemicals

The use of carbon dioxide as a building block in the synthesis of chemicals is a strategy known since the second half of the 19th century. In general, the processes of carbon dioxide conversion into chemicals can be classified in thermal- and catalytic-routes. Thermal processes mainly concern $CO_2$ conversion into urea, salicylic acid and inorganic carbonates, while organic carbonates and methanol production covers a prominent role in the catalytic transformation.

Nowadays, the largest chemical use of carbon dioxide is in the synthesis of urea, that can be used, for example, as fertilizer or as a reactant for polymer production. Currently, about 155 Mt/year of urea are produced, with an estimated growth per year of about 5 -7 % being foreseen for the next 20 years [33]. Urea is produced through a well-known two-step thermal process, in which $CO_2$ and $NH_3$ react to give ammonium carbamate (exothermic step), followed by its dehydration to urea (endothermic step) (Scheme 1.1). Since the overall process is exothermic ($\Delta_r H$ = -101 kJ mol$^{-1}$), the evolved heat can be efficiently recovered and used [34].
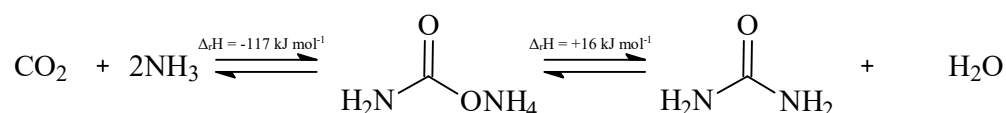
**Scheme 1.1.** Synthesis of Urea by thermal two-step process.

Another important process that can occur without using catalysts is the synthesis of salicylic acid. Nowadays, a relatively low amount of carbon dioxide is recycled to salicylic acid, with an annual production of roughly 90 kt. The process is relatively exothermic and concerns the reaction between phenol salts and $CO_2$ (Scheme 1.2). Industrially, the process is performed under pressure, with temperatures ranging from 100 to 160 °C. [35,36].
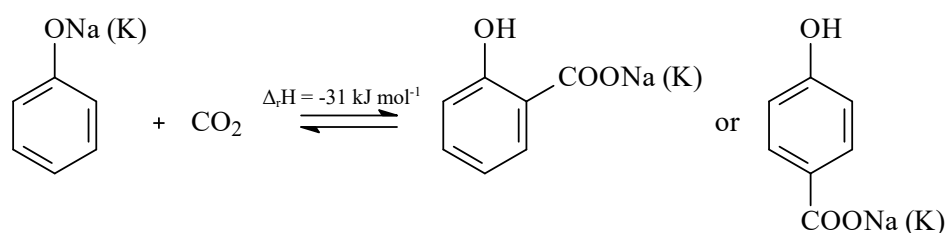


**Scheme 1.2.** Synthesis of salycilic acid.

Carbonation is a thermal process used to produce inorganic carbonates. The current market of inorganics carbonates is close to 200 Mt/year, with $CaCO_3$ playing the main role. An important application related to the carbonation processes is the "mineral carbonation", through which the storage of carbon dioxide as calcium and magnesium carbonates can be achieved. $CO_2$ storage through carbonation of minerals such as olivine (a magnesium iron silicate) and wollastonite (a calcium inosilicate) results particularly interesting as an option for geological storage, especially in regions where underground storage is not practicable. In addition, the mineral carbonation is an exothermic process and the heat recovered can be advantageously recovered and used. However, since the natural carbonation is a very slow process, mechanical and chemical pretreatments of the mineral are needed in order to accelerate the reaction and make its industrial use possible [5].

Among the catalytic processes for chemical recycling of $CO_2$ into chemicals, the synthesis of organic carbonates from carbon dioxide and epoxides is the most established and commercialised reaction. Depending on the type of catalysts, cyclic carbonates [37] or aliphatic polycarbonates [38] can be obtained (Scheme 1.3).
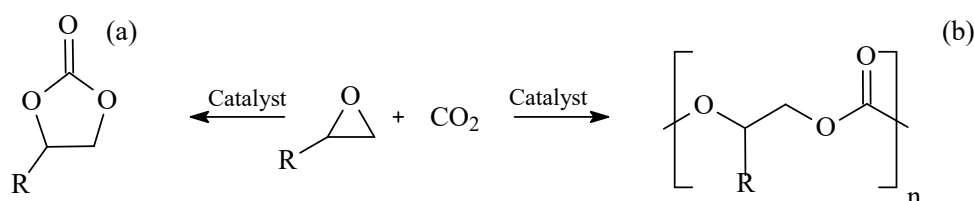


**Scheme 1.3.** Catalytic conversion of $CO_2$ to organic carbonates (a) and aliphatic polycarbonates (b).

Today, the market of cyclic carbonates is expanding (100 kt/year), as they are used in different applications, such as solvents [39,40], electrolytes for lithium ion batteries [41], and as reactants for the synthesis of polymers and dimethyl carbonate (DMC). The latter is industrially produced through transesterification of cyclic carbonates with methanol, finding a large utilisation in the production of aromatic polycarbonates (605 kt/year) as substitutes of phosgene [42]. Moreover, potential applications of aliphatic polycarbonates are currently evaluated, as they display interesting properties, such as transparency and impact resistance, which allow them to be used in substitution of classical polymers derived from fossil fuels [43].

Catalytic hydrogenation is another interesting way to convert carbon dioxide, since it leads to the production of methanol by using suitable catalysts. Methanol has the double role of chemical and fuel, therefore it potentially covers a prominent role in $CO_2$ recycling. Methanol is used in numerous industrial processes as the methylating agent, as well as for the production of formaldehyde, acid acetic, methylamine, and DMC. In addition, it can also be used directly as a solvent or antifreeze, as well as in waste water treatments. Although methanol is mainly produced from syngas (about 4 kt/year) [36], its production from $CO_2$ is attracting growing attention, due to the possibility to achieve higher selectivity.

### 1.3.3.3. $CO_2$ conversion to fuels

The conversion of carbon dioxide into chemicals represents a useful option for CCU technologies, however their market is relatively limited compared to that of fuels. Moreover,

since the amount of $CO_2$ emitted from fuels combustion is remarkably larger than that which can be converted into chemicals, a considerable amount of carbon dioxide needs to be used for fuels production so as to allow for a significant impact in terms of sustainability.

Among the possible routes to convert $CO_2$ into fuels, carbon dioxide deoxygenation to CO can be performed through very energy-demanding thermal or radiative processes (Scheme 1.4).

$$CO_2 \longrightarrow CO + 1/2\ O_2 \qquad \Delta_rG_{1000K} = 190.5\ kJ\ mol^{-1}$$
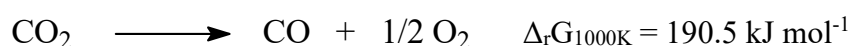
**Scheme 1.4.** Deoxygenation of carbon dioxide into CO.

The formed CO can be burnt with air to give energy and obviously carbon dioxide. Researches in this field are focused on the possibility to perform the reaction under catalytic condition; in this light, some studies showed that when $CO_2$ is coordinated to a metallic centre the process may occur at room temperature [44]. On this basis, great benefits will be possible by combining the abstraction of oxygen from $CO_2$ with the oxidation of organic substrates, with a particular interest addressed to epoxidation reactions [45].

The most relevant industrial processes for $CO_2$ conversion into fuels require hydrogen as a reactant and suitable catalysts (Scheme 1.5). It is worth pointing out that though $H_2$ can be directly used as an energy carrier, its conversion to carbon-based fuels clearly shows some benefits, mainly related to its lower energy density in comparison with methanol, methane, and hydrocarbons. From a thermodynamic point of view, $CO_2$ reduction to any carbon-based fuels is always feasible ($\Delta_rH < 0$). However, severe kinetic limitations, originated from the high energetic barrier, need to be overcome for activating carbon dioxide, making essential the development of highly efficient catalysts.

$$CO_2 + 3H_2 \longrightarrow CH_3OH + H_2O$$
$$CO_2 + 4H_2 \longrightarrow CH_4 + 2H_2O$$
$$(n+2)\ CO_2 + [3(n+2) + 1]\ H_2 \longrightarrow CH_3(CH_2)_n\ CH_3 + 2(n+2)\ H_2O$$
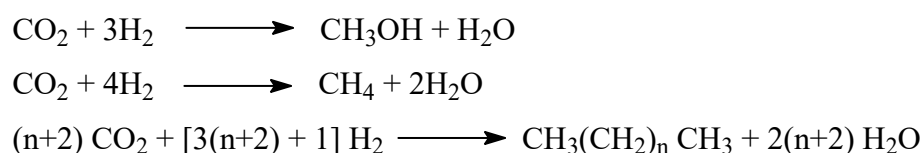
**Scheme 1.5.** $CO_2$ conversion into methanol, methane, and hydrocarbons.

Both *indirect* and *direct* routes are possible for the $CO_2$ chemical recycling into fuels. In the first case, a preliminary conversion of carbon dioxide to CO/syngas, through the *Reverse Water Gas Shift* (RWGS), methane dry reforming [46], or gasification, is needed [47,48], followed by the CO/syngas conversion into methanol or hydrocarbons. Instead, the second strategy consists in the direct reaction of $CO_2$ with hydrogen, that can occur with different mechanisms, depending on the catalyst. The development of suitable catalysts for the direct conversion of carbon dioxide into fuels is a challenging goal, for which an intensive research must be done.

For the production of methanol from carbon dioxide, Cu/ZnO-based catalysts are used, the higher $H_2$ consumption and the formation of water being the main disadvantages with respect to the classical synthesis from syngas. As already mentioned, methanol can be efficiently used as a fuel, and different relevant scientists have highlighted its prominent role for a future sustainable economy (known as the "*methanol economy*") [49,50]. In addition, methanol can be transformed in other important species having relevance in the energetic sector: through the use of suitable catalysts having acidic properties (typically ZSM-5), methanol can be dehydrated into DME and, by subsequent reactions, can be transformed into olefins (MTO process) or hydrocarbons (MTG process) (Scheme 1.6) [50-52].
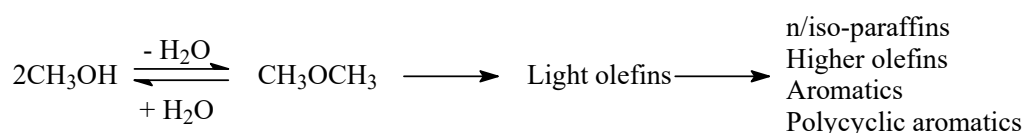


**Scheme 1.6.** Methanol as feedstock for DME, MTO, and MTG processes.

$CO_2$ hydrogenation to methane, known as the "*Sabatier reaction*", is another interesting process to convert carbon dioxide. Different catalysts based on Ru, Rh, and Ni have been used, although improvements in their formulation are still needed in order to achieve higher $CO_2$ conversion at mid-temperature conditions. Compared to methanol, methane is characterised by a lower energetic density and its formation requires a larger amount of hydrogen. However, methanation reaction allows $CO_2$ to be converted in a higher extent; moreover, methane can be promptly used in the conventional energy distribution grid without any modification needed, making the development of efficient processes for its production from $CO_2$ a central topic in the scheme of CCU technologies [53].

The direct conversion of $CO_2$ to higher hydrocarbons occurs through the "*Fischer-Tropsch*" (FT) process (on the whole, similar to the classic process starting from syngas), for which the classic FT catalysts based on cobalt or iron are used. It has been reported in the literature that, by using Co-based catalysts, $CO_2$ hydrogenation produces $CH_4$ as the main product [54,55]; on the other hand, a mix of hydrocarbons, quite similar to that obtained by using syngas as the feedstock, is obtained on iron-based catalysts [56].

Although the chemical recycling of carbon dioxide to fuels is potentially the best way to meet the criteria of sustainability, the key issue remains the high consume of energy and hydrogen. In fact, since this energy is currently produced from fossil fuels, the overall amount of $CO_2$ emitted for *biofuels* production can be higher than that used as the feedstock. Currently, about 90% of hydrogen is produced from fossil fuels by highly energy-demanding processes, through which a sustainable catalytic reduction of carbon dioxide into fuels is not feasible. Perennial sources of energy such as solar light, wind, hydro-, and geothermal energy, are the main resources towards which scientists, industries, and governments, have to concentrate their investments for a sustainable future. Such renewable energy sources can be used to convert water to hydrogen through electrochemical and photo-electrochemical processes, though technological improvements are still needed in order to make these processes competitive with respect to the classical route. In fact, the economic analyses concerning $H_2$ production from various technologies (Tab. 1.4) [5], clearly show how the production of hydrogen from renewable energy sources, such as solar light and wind, still remains more expensive with respect to the production from fossil fuel.

**Tab. 1.4.** Costs of production of 1 kg of $H_2$ using various technologies.

| Technology | Cost |
|---|---|
| Gas reforming | 1.10 -1.15 € |
| Electrolysis with nuclear | 1.45 – 1.50 € |
| Electrolysis with electricity from oil power station | 2.20 – 3.50 € |
| Electrolysis with photovoltaic | 2.8 – 4.0 € |
| Electrolysis with wind | 3.80 – 5.20 € |
| Electrolysis with SPC | 3.50 € |

Photovoltaic (PV) technologies are potentially very interesting to convert solar energy in $H_2$ through the electrolysis of water. This is especially true by considering the remarkable increase in efficiency that could be achieved with the advent of thin film-based technologies, in substitution of the classic ones based on monocrystalline Si. The key parameters for the PV systems are related to the overvoltage for the hydrogen production and to the electrolysis efficiency, for which some technological issues needed to be solved in order to make this approach mature enough to be competitive from an economic point of view.

*References*

[1]  IPCC (2013), *Working Group I Contribution to the IPCC Fifth Assessment Report, Climate Change 2013: The Physical Science Basis, Summary for Policy Makers*, available at: www.ipcc.ch/.

[2]  M. Aresta, A. Dibenedetto, A. Angelini, *Phil. Trans R. Soc. A* 371 (2013) 20120111.

[3]  International Energy Agency (IEA), *$CO_2$ EMISSION FROM FUEL COMBUSTION Highlights*, (2016) Paris.

[4]  Carbon Dioxide Information Analysis Center, Oak Ridge National Laboratory, US Department of Energy, Oak Ridge, Tenn., United States.

[5]  M. Aresta, A. Dibenedetto, A. Angelini, *Chem. Rev.* 114 (3) (2014) 1709.

[6]  Y. Wolde-Rufael, S. Idowu, *Renew. Sust. Energ. Rev.* 74 (2017) 1336.

[7]  T. P. Senftle, E. A. Carter, *Acc. Chem. Res.* 50 (2017) 472.

[8]  N. Mac Dowell, P. S. Fennell, N. Shah, G. C. Maitland, *Nat. Clim. Change*, 7 (2017) 243.

[9]  World Commission on Environment and Development*, Our Common Future*, Oxford University Press (1987) New York.

[10]  P.T. Anastas, J.C. Warner, *Green Chemistry: Theory and Practice*, Oxford University Press (1998) New York.

[11]  P.T. Anastas, L.B. Bartlett, M.M. Kirchhoff, T.C. Williamson, *Catal. Today* 55 (2000) 11.

[12]  P.T. Anastas, M.M. Kirchhoff, T.C. Williamson, *Appl. Catal. A: Gen*. 221 (2001) 3.

[13]  P. Styring, E. A. Quadrelli, K. Armstrong, *Carbon Dioxide Utilisation-Closing the carbon cycle*, ELSEVIER (2015) Amsterdam.

[14]  M. Aresta, A. Dibenedetto, *Dalton Trans.* (2007) 2975.

[15]    F.A. Rahman, M.M.A. Aziz, R. Saidur, W.A.W.A. Bakar, M.R. Hainin, R. Putrajaya, N.A. Hassan, *Ren. and Sust. En. Rev.* 71 (2017) 112.

[16]    D. H. Gibson, *Coordin. Chem. Rev.* 185-186 (1999) 335.

[17]    M. North, P. Styring, *Faraday Discuss.* 183 (2015) 489.

[18]    J. Wilcox, *Carbon Capture*, Springer (2012) New York.

[19]    International Energy Agency (IEA), *Energy Technology Perspectives 2012 (ETP 2012)*, OECD/IEA (2012) Paris.

[20]    S.T. McCoy, E.S. Rubin, *Int. J. Green. Gas Control* 2 (2008) 219.

[21]    Y. Huang, S. Rebennack, Q.P. Zheng, *Energy Syst.* 4 (2013) 315.

[22]    R. Wennersten, Q. Sun, H. Li, *J. Clean Prod.* 103 (2015) 724.

[23]    C.-H. Yu, C.-H. Huang, C.-S. Tan, *Aerosol Air Qual. Res.* 12 (2012) 745.

[24]    L. Zhu, G.W Schade, C.J. Nielsen. *Environ. Sci. Technol.* 47 (2013) 14306.

[25]    A. Henni, P. Tontiwachwuthikul, A. Chakma, *Can. J. Chem. Eng.* 83 (2005) 358.

[26]    X. Gui, Z. Tang, W. Fei, *J. Chem. Data* 55 (2010) 3736.

[27]    E.D. Bates, R.D. Mayton, I. Ntai, J.H. Davis, *J. Am. Chem. Soc.* 124 (2002) 926.

[28]    K.A. Mumford, N.R. Mirza, G.W. Stevens, *En. Procedia*, 114 (2017) 2671.

[29]    P. Bollini, S.A. Didas, C.W. Jones, *J. Mater. Chem*. 21 (2011) 15100.

[30]    A. Schoedel, Z. Ji, O.M. Yaghi, *Nature Energy* 1 (2016) 16034.

[31]    G. Centi, S. Perathoner, *Catal. Today* 148 (2009) 191.

[32]    M. Aresta, *Carbon Dioxide Recovery and Utilization*, Springer (2003) Dordrecht.

[33]     M. Aresta, A. Dibenedetto, L.-N. He, *Analysis of demand for captured CO₂ and products from CO₂ conversion. Report exclusively for Members of the Carbon Dioxide Capture and Conversion (CO₂CC) Program of The Catalyst Group* (2002).

[34]     P. Brinckerhoff, *Accelerating the Uptake of CCS: Industrial Use of Captured Carbon Dioxide-Urea Synthesis* Global CCS Institute (2011) Docklands Australia, www.globalccsinstitute.com.

[35]     A.S. Lindsay, H. Jeskey, *Chem Rev.* 57 (1957) 583.

[36]     I. Omae, *Coord. Chem. Rev.* 256 (2012) 1384.

[37]     M. North, R. Pasquale, C. Young, *Green Chem.* 12 (2010) 1514.

[38]     M.R. Kember, A. Buchard, C.K. Williams, *Chem. Commun.* 47 (2011) 141.

[39]     B. Schaffner, F. Schaffner, S.P. Verevkin, A. Borner, *Chem. Rev.* 110 (2010) 4554.

[40]     A.E. Díaz-Álvarez, J. Francos, B. Lastra-Barreira, P. Crochet, V. Cadierno, *Chem. Commun. (Camb.)* 47 (2011) 6208.

[41]     K. Xu, *Chem. Rev.* 104 (2004) 4303.

[42]     W.-L. Dai, S.-L. Luo, S.-F. Yin, C.-T. Au, *Appl. Catal A: Gen.* 366 (2009) 2.

[43]     S.H Lee, A. Cyriac, J.Y. Jeon, B.Y. Lee, *Polym. Chem.* 3 (2012) 1215.

[44]     M. Aresta, C.F. Nobile, V.G. Albano, E.Forni, M. Manassero, *J. Chem. Soc. Chem. Commun.* (1975) 636.

[45]     M. Aresta, A. Dibenedetto, *J. Mol. Catal.* 399 (2002) 182.

[46]     L. Shi, G. Yang, K. Tao, Y. Yoneyama, Y. Tan, N. Tsubaki, *Ace. Chem. Res.* 46 (2012) 1838.

[47]     R.C. Shurtz, T.H. Fletcher, *Energ. Fuels* 27 (2013) 3022.

[48]     R. Silbermann, A. Gomez, I. Gates, N. Mahinpey, *lnd. Eng. Chem. Res.* 52 (2013) 14787.

[49]     G. A. Olah, A. Goeppert, G. K. S Prakash, *Beyond Oil and Gas: The Methanol Economy*; WILEY-VCH (2006) Weinheim.

[50]   G. A. Olah, A. Goeppert, G. K. S Prakash, *J. Org. Chem.* 74 (2009) 487.

[51]   C. Chang, A. Silvestri, *Chem Technol.* 10 (1987) 624.

[52]   M. Bjorgen, S. Svelle, F. Joensen, J. Nerlov, S. Kolboe, L. Palumbo, S. Bordiga, U. Olsbye, *J. Catal.* 249 (2007) 195.

[53]   P. Frontera, A. Macario, M. Ferraro, P. Antonucci, *Catalysts* 7 (2017) 59.

[54]   Y. Zhang, G. Jacobs, D.E. Sparks, M.E. Dry, B.H. Davis, *Catal. Today* 71 (3–4) (2002) 411.

[55]   X. Zhang, B. Dai, A. Zhu, W. Gong, C.J. Liu, *Catal. Today* 72 (2002) 223.

[56]   T. Riedel, M. Claeys, H. Schulz, G. Schaub, S.-S. Nam, K.-W. Jun, M.-J. Choi, G.  Kishan, K.-W. Lee, *Appl. Catal., A: Gen.* 186 (1–2) (1999) 201.

<u>*Chapter II*</u>

# *Experimental procedures*

# *and*

# *instrumentation*

## 2.1. Synthesis procedures

### 2.1.1 Catalysts for CO$_2$ conversion to cyclic carbonates

A series of imidazolium-based (Imi) catalysts was prepared by functionalization of mesostructured Al_SBA-15 aluminosilicates with different aluminium contents (Si/Al molar ratio = 80, 20, and 5 mol mol$^{-1}$). The catalysts were used for CO$_2$ conversion into cyclic carbonates by using different epoxides.

### 2.1.1.1. Materials

Tetraethylorthosilicate (TEOS, 98 %), Pluronic P123 triblock copolymer (EO$_{20}$PO$_{70}$EO$_{20}$), Al(NO$_3$)$_3$·9H$_2$O ($\geq$ 98%), 1-methylimidazole (99%), 3-(chloropropyl)-trimethoxysilane (97%), Methanol (99.8%, anhydrous), and Toluene (99.8%, anhydrous) were purchased from Aldrich. HCl (37%) was provided by Merck.

### 2.1.1.2. Imi/*x*Al_SBA-15

The Imi/*x*Al_SBA-15 catalysts, where *x* is referred to the Si/Al molar ratio, were synthesised through a one-pot functionalization of Al_SBA-15 with 1-methylimidazole and 3-(chloropropyl)-trimethoxysilane.

First, three different *x*Al_SBA-15 supports were prepared (*x* =5, 20, and 80 mol mol$^{-1}$) by a modified two-step "pH-adjusting" method [1] by using Al(NO$_3$)$_3$·9H$_2$O as the aluminium source. In a typical synthesis 4 g of Pluronic P123 and 126 mL of a 2 M HCl aqueous solution were stirred at 40 °C until complete dissolution of the surfactant. Next, 8.5 g of TEOS was added drop-wise to the above solution and the mixture was kept under magnetic stirring at 40 °C for 4 h. The amount of Al(NO$_3$)$_3$·9H$_2$O required to obtain the desired Si/Al molar ratio was then added, followed by magnetic stirring for 20 h at 40 °C. The resulting gel was introduced into a 250 mL Teflon-lined stainless-steel autoclave and submitted to a first hydrothermal treatment at 100 °C overnight. Next, the resulting suspension was cooled to ambient temperature and then the pH value of the mother liquor was adjusted to 7.5 with ammonia under stirring. The mixture was then submitted to a second hydrothermal treatment in autoclave at 100 °C for 48 h. Finally, the solid was separated by filtration, washed with distilled water, dried at 60 °C overnight, and calcined in an oven at 550 °C for 5 h (heating rate, 4 °C min$^{-1}$).

Functionalization of the *x*Al_SBA-15 surface to obtain an imidazolium-based catalyst, was performed via a one-pot procedure by reacting the previously synthesised supports with a mixture of 1-methylimidazole and 3-(chloropropyl)-trimethoxysilane (Scheme 2.1). This procedure, compared to the standard approach [2-4], presents the multiple advantages of a fast functionalization together with a limited number of separation and purification steps.
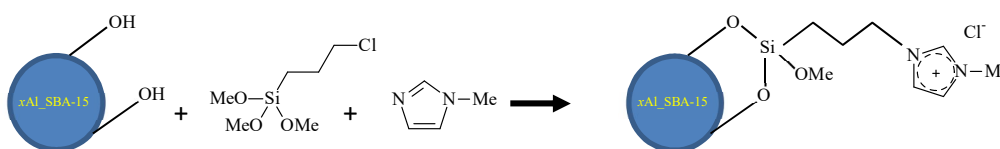


**Scheme 2.1.** Synthesis of Al_SBA-15 supported imidazolium-based catalyst.

In a typical synthesis, 1.5 g of supports (previously dried at 100 °C overnight) were dispersed in 20 cm$^3$ of toluene. Then, 2.21 cm$^3$ of 3-(chloropropyl)-trimethoxysilane (12 mmol) and 2 cm$^3$ of 1-methylimidazole (24 mmol) were added, and the suspension was kept under reflux for 24 h. Next, the solid was filtered and washed with hot methanol (50 °C). The material recovered was then dried at 60 °C for overnight and kept under reflux with methanol for 48 h to remove the imidazolium-species not anchored on the surface of the support. Finally, the catalyst was filtered and dried at 100 °C overnight.

## 2.1.2. Catalysts for CO$_2$ conversion to methane

NiO/CeO$_2$ mixed oxides with increasing Ni contents were synthesized by using two different preparation procedures: the "*Hard-Template*" (HT) and "*Soft-Template*" (ST) methods. A NiO/γ-Al$_2$O$_3$ sample was also prepared by depositing Ni on a commercial alumina through impregnation. The catalytic behaviour of the prepared samples was investigated in the CO$_2$ methanation reaction.

### 2.1.2.1. Materials

Tetraethylorthosilicate (TEOS, 98%), Pluronic copolymer P123 (EO$_{20}$PO$_{70}$EO$_{20}$), Cetyl trimethylammonium bromide (CTAB, ≥ 98%), Ni(NO$_3$)$_2$·6H$_2$O (99.999%), Ce(NO$_3$)$_3$·6H$_2$O

(99%), and NaOH (pellets, 97%) were supplied by Aldrich. Ethanol (96%) was supplied by Fluka. HCl (37%) was provided by Merck. Commercial $\gamma$-Al$_2$O$_3$ was provided by CONDEA.

### 2.1.2.2. *Hard-Templated xNiO/CeO$_2$*

The $x$NiO/CeO$_2$_HT samples ($x$ = Ni/Ce) were prepared by the *Hard-Template* method, using the SBA-15 mesostructured silica as the template.

SBA-15 was prepared under hydrothermal condition as previously reported by Zhao et al. [5]. In a typical synthesis, 4 g of Pluronic 123 were added to 120 g of HCl (2 M) and 30 g of distilled water. After 15 h under stirring at 35 °C, 8.5 g of TEOS were added and the solution was maintained at 35 °C for 24 h under stirring. The resulting gel was then transferred into a stainless-steel autoclave and kept at 100 °C for 24 h under static conditions. The obtained suspension was filtered and the recovered solid was washed with distilled water, dried at 40 °C overnight and finally calcined in air at 550 °C for 5 h.

The $x$NiO/CeO$_2$_HT catalysts were then prepared as fallow: in a typical synthesis, Ni and Ce nitrates were dissolved in 25 cm$^3$ of ethanol to obtain a total concentration of the metals equal to 0.7 M. The relative amounts of the oxides precursors were adjusted to have Ni/Ce molar ratios in the range 0.15 – 1.0 mol mol$^{-1}$. 15 cm$^3$ of the obtained solution were then added to 1 g of SBA-15 and the suspension was stirred at room temperature for 1 h. Next, the solvent was evaporated at 60 °C overnight and the resulting solid was transferred into a furnace and calcined at 500 °C for 3 h to decompose the nitrates into the corresponding oxides. The impregnation (with the remaining 10 cm$^3$ of the ethanolic solution), drying, and calcination steps were then repeated with the aim of filling the SBA-15 pores completely. The SBA-15 template was then removed by leaching with a NaOH solution (2 M) at 50 °C. Lastly, the resulting material was washed to pH 7 with distilled water, dried at 60 °C for 12 h and then calcined at 500 °C under static conditions for 3 h, and the leaching-calcination cycle was then repeated. The obtained samples were named $x$NiCe_HT, where $x$ is the nominal Ni/Ce molar ratio. The HT procedure was also used to prepare a pure CeO$_2$ (named CeO$_2$_HT), on which Ni was deposited through the incipient wetness impregnation (IWI) technique. Appropriate volumes of aqueous solutions, containing suitable Ni(NO$_3$)$_2$ amounts, were added to 0.5 g of CeO$_2$_HT. The resulting paste was then dried at 60 °C overnight and the solid was subsequently calcined at 500 °C for 3 h. The obtained catalysts were named $x$NiCe_HT$_{IWI}$, where $x$ is the nominal Ni/Ce molar ratio ranging between 0.15 and 1.0 mol mol$^{-1}$.

### 2.1.2.3. *Soft-Templated x*NiO/CeO₂

The $x$NiO/CeO₂_ST mixed oxides were synthesized with different Ni/Ce molar ratios ($x$), using the *Soft-Template* (ST) method [6,7]. Pure cerium and nickel oxides (named CeO₂_ST and NiO_ST, respectively) were first prepared using Ce(NO)₃·6H₂O or Ni(NO₃)·6H₂O as precursors, cetyl-trimethyl-ammonium bromine (CTAB) as the template, and NaOH as the precipitating agent. For the synthesis, appropriate amounts of the nitrate precursor and the template (CTAB/precursor = 0.62 mol mol⁻¹) were dissolved at room temperature in 100 cm³ of distilled water under stirring. After 30 min, a 0.17 M solution of NaOH was added dropwise until a pH value of 13 was reached; the mixture was then stirred for 15 h. After digestion at 90 °C for 3 h, the formed solid was filtered and washed with hot water (70 °C) until formation of AgBr precipitate in the filtrate by reaction of bromides with AgNO₃ was no longer observed. Then, it was dried at 110 °C for 6 h and finally calcined at 450 °C for 4 h. A similar surfactant-templated procedure, in which the ceria and nickel oxide precursors were coprecipitated, was used for preparing NiO-CeO₂ systems with Ni/Ce molar ratios in the range 0.3–4.0 mol mol⁻¹. The obtained materials were named $x$NiCe_ST, were $x$ represents the nominal value of the Ni/ Ce molar ratio. Pure CeO₂_ST was used as the support to prepare a second series of mixed oxides catalysts, with a Ni/Ce ratio between 0.3 and 1.5 mol mol⁻¹. In this case, nickel was deposited on the carrier through incipient wetness impregnation from a solution containing suitable amounts of Ni(NO₃)·6H₂O. After drying at 40 °C overnight, the obtained solids, named $x$NiCe_ST$_{IWI}$, were calcined at 450 °C for 3 h.

### 2.1.2.4. NiO/γ-Al₂O₃

NiO/γ-Al₂O₃ catalyst was prepared by incipient wetness impregnation method, having a Ni content equal to 25 wt% ($g_{Ni}/g_{cat}$). For the synthesis, an appropriate volume of aqueous solution, containing suitable Ni(NO₃)₂ amount, was added to 0.5 g of commercial γ-alumina. The resulting paste was then dried at 60 °C overnight and the solid was subsequently calcined at 500 °C for 3 h. The obtained catalyst was named NiAl_IWI.

### 2.1.3. Catalysts for CO₂ conversion to methanol

Two series of Cu-based catalysts were prepared and used in the CO₂ hydrogenation reaction to methanol. The first series of mixed oxides was prepared using hydrotalcites as precursors, while the second one was instead prepared through the *"Soft-Template"* method.

### 2.1.3.1. Materials

Cetyl trmethylammonium bormide (CTAB, $\geq$ 98%), $Cu(NO_3)_2 \cdot 2.5H_2O$ (98%), $Al(NO_3)_3 \cdot 9H_2O$ ($\geq$ 98%), $Zn(NO_3)_2 \cdot 6H_2O$ (98%), $ZrO(NO_3)_2 \cdot 6H_2O$ (99%), $Ce(NO_3)_3 \cdot 6H_2O$ (99%), $Na_2CO_3$ (99%), and NaOH (pellets, 97%) were supplied by Aldrich.

### 2.1.3.2. $z$CuO/$y$ZnO/$w$Al₂O₃/$v$ZrO₂/$u$CeO₂ from hydrotalcites

A series of $z$CuO/$y$ZnO/$w$Al₂O₃/$v$ZrO₂/$u$CeO₂ mixed oxides were synthesised with different composition *via* the hydrotalcite method [8]. For preparing hydrotalcites, an aqueous solution (100 cm³) containing appropriate amounts of $Cu(NO_3)_2$, $Al(NO_3)_3$, $Zn(NO_3)_2$, $ZrO(NO_3)_2$, and $Ce(NO_3)_3$ (with a total concentration equal to 1.5 M) was first prepared. A second solution containing 7.15 g of $Na_2CO_3$ and 13.95 g of NaOH in 100 cm³ of distilled water, was then slowly added to the former one, at room temperature and under stirring, by using a peristaltic pump, which allowed the flow rate to be adjusted in order to maintain the pH constant and equal to 11. After digestion at 60 °C for 20 h, the resulting hydrotalcite was dried at 80 °C overnight, and finally calcined at 500 °C for 4 h in order to obtain the corresponding mixed oxide. The prepared catalysts were named $z$Cu/$y$Zn/$w$Al/$v$Zr/$u$Ce_Htl, where $z,y,w,v,$ and $u$ represent the Cu/Zn/Al/Zr/Ce molar composition.

### 2.1.3.3. *Soft-Templated $z$*CuO/yZnO/uCeO₂

Two $z$CuO/$y$ZnO/$u$CeO₂ mixed oxides were synthesized with different Cu/Zn/Ce molar ratios, using the *Soft-Template* (ST) method, which has already been described in detail (cf. par. 2.1.2.3). Bi-component (CuO/CeO₂) and tri-component (CuO/ZnO/CeO₂) systems were prepared, which were named $z$Cu/$u$Ce_ST and $z$Cu/$y$Zn/$u$Ce_ST (where $z,y,$ and $u$ represent the molar composition of Cu, Zn, and Ce, respectively).

## 2.2. Characterisation techniques

### 2.2.1. Inductively coupled plasma atomic emission spectroscopy (ICP-AES)

ICP-AES technique was used to determine the Si, Al, Ni, Ce, Cu, Zn, and Zr contents in the prepared samples (supports and catalysts). Analyses were performed with a Liberty 200 spectrophotometer (Varian). For the determination of Al, Ni, Ce, Cu, Zn, and Zr, the samples

(ca. 0.015 g) were first dissolved in concentrated hydrofluoric acid (40%); after evaporation, the residues were dissolved in a mixture of HCl (37%) and $HNO_3$ (70%) (3:1 by volume) and then diluted to 250 $cm^3$ with Milli-Q water. For determining the Si content, about 0.1 g of sample were placed in a platinum crucible. After addition of 1.5 g of $Na_2B_4O_7$, alkaline fusion was performed in the furnace at 1000 °C for 30 min. Then the "pearl" was transferred into a beaker, 100 $cm^3$ of $HNO_3$ (5 vol%) were added and the mixture was heated at 80 °C until complete dissolution of the sample (typically for 30 min). The solution was finally transferred into a volumetric flask and diluted to the final volume with Milli-Q water for ICP-AES analysis.

## 2.2.2. X-ray diffraction (XRD)

XRD analyses were performed using a X3000 diffractometer (Seifert), with a θ-θ Bragg-Brentano geometry with a Cu-Kα wavelength and a graphite monochromator before the scintillation detector.

Structural characteristics of the catalysts prepared for the $CO_2$ reduction to methane and methanol were investigated in the range 20-65 ° (2θ) and 20-70 ° (2θ), respectively; the average crystallite sizes ($D_p$) were estimated by the Scherrer equation [9]. The mesostructure of the *x*Al_SBA-15 supports was studied by low-angle X-ray diffraction analysis in the range 0.8-2.5 ° (2θ).

## 2.2.3. Transmission Electron Microscopy (TEM)

Electron micrographs were obtained with a 200CX transmission electron microscope (JEOL) operating at an accelerating voltage of 200 kV. Finely ground samples were dispersed in n-octane in an ultrasonic bath. The suspension was then dropped on a copper grid covered with a carbon thin film for the observation.

## 2.2.4. $N_2$ adsorption/desorption

Textural analyses were carried out with an ASAP 2020 system (Micromeritics), by determining the nitrogen adsorption-desorption isotherms at −196 °C. Before analysis, the sample was heated overnight under vacuum up to 250 °C (heating rate, 1 °C $min^{-1}$). Surface area values were calculated by the BET equation. The mean pore diameter was determined by applying the BJH method to the isotherm desorption branch [10].

## 2.2.5. Magic Angle Spinning Nuclear Magnetic Resonance (MAS NMR)

$^{27}$Al and $^{29}$Si NMR analyses were performed on $x$Al_SBA-15 supports and Imi/$x$Al_SBA-15 catalysts.

### 2.2.5.1. $^{27}$Al MAS NMR

$^{27}$Al direct excitation magic-angle spinning (MAS) NMR spectra were recorded at room temperature by using a Varian VNMRS 400 spectrometer operating at 9.4T (104.2MHz for $^{27}$Al) equipped with a 4 mm CP-MAS Varian/Chemagnetics probe. The sample was packed in a 4 mm zirconia rotor and spun at a spinning frequency of 12000 Hz. Measurements were performed by using a 1 s relaxation delay. The processing comprised zero-filling, Fourier transform, phase and baseline corrections. The chemical shift scale was calibrated at RT with respect to a solid sample of $AlCl_3$ hexahydrate ($\delta$=0.0 ppm). Quantitative information on the $^{27}$Al atom environments was obtained by fitting the signals with Gaussian functions using the software package Origin 9 from OriginLab Corporation.

### 2.2.5.2. $^{29}$Si CP MAS NMR

$^{29}$Si cross-polarisation magic-angle spinning (CP-MAS) NMR spectra were recorded at room temperature by using a Bruker Avance-500 spectrometer operating at 11.7T (99.3 MHz for $^{29}$Si) equipped with a 4 mm CP-MAS Bruker probe. The sample was packed in a 4 mm zirconia rotor and spun at a spinning frequency of 8000 Hz. Measurements were performed by using a 5 s relaxation delay and 5 ms contact time. The processing comprised exponential multiplication of the free induced decay (FID) with a line broadening factor of 30 Hz, zero-filling, Fourier transform, phase and baseline corrections. The chemical shift scale was calibrated at RT with respect to a sample of solid 3-(trimethylsilyl)-1-propanesulfonic acid sodium salt (DSS; $\delta$=0.0 ppm).

## 2.2.6. Raman spectroscopy

Raman spectra were measured at room temperature in back-scattering geometry with an inVia Renishaw micro-Raman spectrometer equipped with an air-cooled CCD detector and edge filters. A 488.0 nm emission line from an Ar ion laser was focused on the sample under a Leica DLML microscope, using 20x or 5x objectives. The power of the incident beam was about 5 mW. Repeated (10 or 20 s) accumulations were generally acquired for each sample.

The resolution was 2 cm$^{-1}$ and spectra were calibrated using the 520.5 cm$^{-1}$ line of a silicon wafer. Spectra processing included baseline removal and curve fitting using a Gauss-Lorentz cross-product function by Peakfit 4.12 software (Jandel, AISN Software).

### 2.2.7. Elemental Analysis (CHN)

The imidazolium content of the Imi/*x*Al_SBA-15 samples both fresh and recovered after reaction, was assessed by CHN elemental analysis carried out with an PE 2400 Series II CHN-O analyzer (Perkin Elmer) by total burning at 950 °C in an oxygen/helium mixture.

### 2.2.8. Temperature Programmed Reduction (TPR)

The reducibility of the Ni- and Cu-based catalysts was studied through TPR analysis performed on a TPD/R/O 1100 apparatus (Thermoquest).

TPR profiles on Ni-based catalysts were recorded under the following conditions: sample weight, 0.020 g; heating rate, from 40 to 500 or 950 °C, 20 °C min$^{-1}$; flow rate, 30 cm$^3$ min$^{-1}$; H$_2$, 5 vol% in N$_2$. Prior to the experiment, samples were pretreated in air (15 cm$^3$ min$^{-1}$) at 450 °C for 1 h.

TPR analyses on Cu-based catalysts were performed under the following conditions: sample weight, 0.030 g; heating rate, from 50 to 400 °C, 10 °C min$^{-1}$; flow rate, 30 cm$^3$ min$^{-1}$; H$_2$, 5 vol% in N$_2$. Prior to the experiment, samples were pretreated in N$_2$ (20 cm$^3$ min$^{-1}$) at 350 °C for 2 h.

### 2.2.9. CO$_2$ Temperature Programmed Desorption (CO$_2$-TPD)

CO$_2$-TPD profiles of selected NiO/CeO$_2$_HT samples were collected using a TPD/R/O 1100 apparatus (*ThermoQuest*) connected to a mass spectrometer as the detector (*ProLAB; ThermoONIX*). After saturation of the catalyst (0.1 g) with pulses of CO$_2$ at 50 °C, the physisorbed fraction was eliminated by purging with He (20 cm$^3$ min$^{-1}$) at 100 °C for 1 h. CO$_2$-TPD runs were then performed under He flow (20 cm$^3$ min$^{-1}$) with a heating rate of 10 °C min$^{-1}$ from 100 to 500 °C (then hold for 30 min). Prior to CO$_2$ saturation, samples were treated at 400 °C for 1 h under air flow (30 cm$^3$ min$^{-1}$), purged in He (20 cm$^3$ min$^{-1}$), and then reduced under H$_2$ (15 cm$^3$ min$^{-1}$) at 400 °C for 1 h. In order to quantitatively determine the desorbed CO$_2$, the response factor for the MS signal (M/Z = 44) was calculated from the peaks area corresponding to known doses of the detected gas.

## 2.2.10. H₂-chemisorption

Pulse chemisorption runs on selected $x$NiO/CeO$_2$_ST catalysts were performed in TPD/R/O1100 apparatus (ThermoQuest). Before analysis, the sample (0.050 g) was reduced under H$_2$ flow (15 cm$^3$ min$^{-1}$) at 400 °C for 1 h. Then, N$_2$ (20 cm$^3$ min$^{-1}$) was used for purging (1 h) and cooling at 50 °C. Pulses of H$_2$ (5 vol% in N$_2$) were then admitted into the reactor until the area of the peaks remained constant. Metal surface area was automatically computed by the instrument software by considering a H/Ni stoichiometric factor equal to 1.

## 2.2.11. NH₃ and CO₂ adsorption microcalorimetry

The acidic and basic surface properties were investigated by microcalorimetry, using NH$_3$ and CO$_2$ as probe molecules, respectively.

A Tian-Calvet heat flow microcalorimeter (Setaram) equipped with a volumetric vacuum line was used for microcalorimetric measurements. Each sample (0.1 g, 40-80 mesh) was thermally pre-treated at 250 °C for 12 h under vacuum (5 x 10$^{-5}$ mbar). Adsorption was carried out at 80 °C by admitting successive doses of the probe gas (ammonia or carbon dioxide) and recording the thermal effect. The equilibrium pressure relative to each adsorbed amount was measured by means of a differential pressure gauge (Datametrics) and the thermal effect was recorded. The run was stopped at a final equilibrium pressure of about 1.3 mbar. The adsorption temperature was maintained at 80 °C, in order to limit physisorption. After overnight outgassing at this same temperature, a second run was carried out up to 1.3 mbar. The adsorption isotherm (relating the amount of probe gas with the corresponding equilibrium pressure) and the calorimetric isotherm (relating the integral heat of adsorption with the corresponding equilibrium pressure) were obtained from each adsorption run. Combining the two sets of data, a plot of the differential heat of adsorption as a function of the adsorbed amount was drawn, which gives information on the influence of the surface adsorbed amount on the energetics of the adsorption.

## 2.2.12. CO₂ adsorption Fourier Transform Infrared (FTIR) spectroscopy

FTIR analysis were performed by using a Bruker EQUINOX 55 spectrometer. For the FTIR measurements, the samples (in powder form) were pressed in self-supporting wafer and accurately positioned between two KBr windows, located inside of a quartz cell. After outgassing at 400 °C for 1 h by using a vacuum line (residual pressure equal to 10$^{-3}$ mbar), the

samples were reduced with hydrogen (equilibrium pressure equal to 150 mbar) at the same temperature for 1 h. Next, outgassing was again performed and the sample was cooled under argon atmosphere. After reaching room temperature, argon was pumped out of the samples (until $10^{-3}$ mbar); then, the FTIR spectra were collected after achievement of different equilibrium pressures (ranging from $1 \cdot 10^{-3}$ to 50 mbar) due to send of successive doses of $CO_2$.

## 2.3. Catalytic testing

### 2.3.1. $CO_2$ conversion to cyclic carbonates

Catalytic tests were performed in a Teflon-lined stainless-steel batch reactor (*Cambridge Design Bulfrog*), designed to work at high temperature and pressure. The reactor was equipped with individual temperature and pressure control systems, and with a mechanical overhead stirring (Fig.2.1).
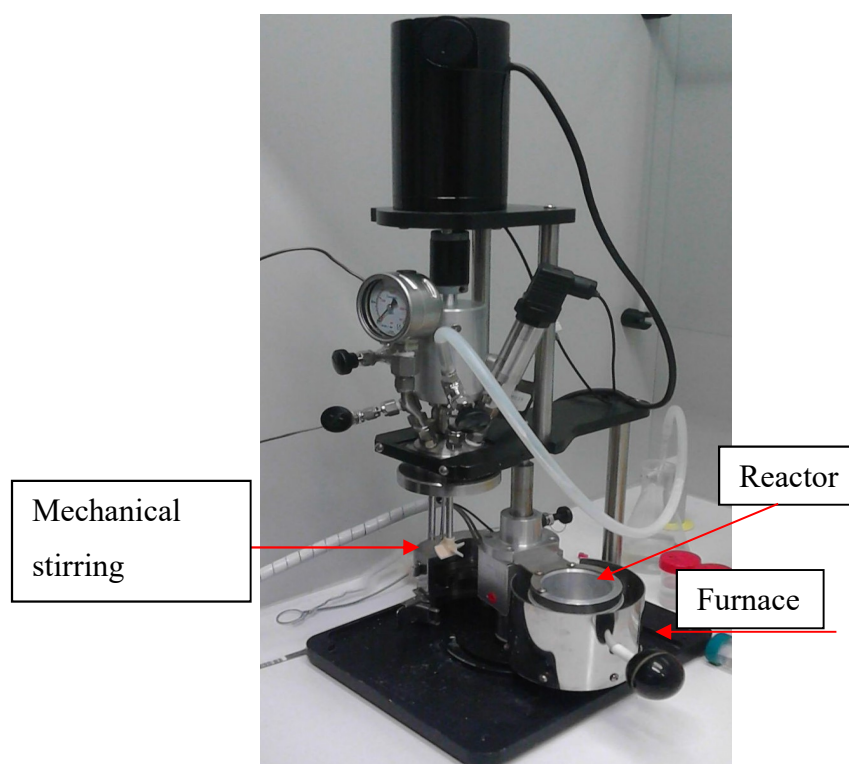


**Fig. 2.1**. $CO_2$ to cyclic carbonates plant.

In a typical catalytic run, 300 mg of catalyst (previously treated at 100 °C overnight) were placed in a Teflon-lined reactor and dispersed with 24 cm$^3$ of epoxide (epichlorohydrin or styrene oxide). The reactor was closed and the mechanical stirring was kept constant at 500 rpm. After purging with N$_2$ (P = 4 bar) for 10 min, the reactor was pressurised with CO$_2$ to the final pressure of 25 bar. Next, the temperature was gradually increased (heating rate, 1 °C min$^{-1}$) from room temperature to the reaction temperature (100 or 125 °C). When temperature reached the operative value, the reaction was allowed to run. After 3 h the system was cooled to room temperature and then depressurised. The reaction mixture was recovered and centrifuged at 5000 rpm for 15 min, then the supernatant was removed and analysed by quantitative $^1$H-NMR (using chloroform-d or toluene-d the solvent) in order to determine the amount of product and residual epoxide.

To perform recycling tests, the catalysts were recovered and washed for 5 times with methanol (25 cm$^3$), treating each time the suspension in an ultrasound bath for 10 min. After each washing step, the catalyst was recovered by centrifugation at 5000 rpm for 15 min. Finally, the catalyst recovered was dried at 100 °C overnight before being reused.

## 2.3.2. CO$_2$ conversion to methane

CO$_2$ methanation was carried out for 6 h under atmospheric pressure in a tubular ($\phi_{int}$ =0.8 cm) quartz-glass fixed-bed continuous-flow microreactor at 300 °C. The reactor was provided with an external jacket filled with silicon carbide which, by blowing with compressed air, simulates a fluidized bed and allows the system to be kept in isothermal conditions once the reaction temperature is reached upon heating in an electric furnace. The temperature was monitored by a K-type thermocouple located into the thermostatic jacket and connected to a temperature-programmer/controller. A second K-type thermocouple was positioned inside the reactor to check the temperature of the catalytic bed (Fig. 2.2).

0.050 g of catalyst (> 120 mesh) were placed into the reactor without diluting with an inert material. Prior to the reaction, the catalyst was pretreated in air (30 cm$^3$ min$^{-1}$) at 400 °C overnight; after purging in N$_2$ (20 cm$^3$ min$^{-1}$), it was subsequently reduced under H$_2$ flow (15 cm$^3$ min$^{-1}$) at the same temperature for 1 h and then cooled in N$_2$ (20 cm$^3$ min$^{-1}$) to the desired reaction temperature. The reactant gas mixture (CO$_2$, 10 mol%; H$_2$, 43 mol%; balance He) was fed to the reactor with a total flow rate of 60 cm$^3$ min$^{-1}$ (space velocity, SV = 72000 cm$^3$ h$^{-1}$ g$_{cat}^{-1}$). On selected samples, the effect of time-on-stream (t.o.s.), reaction

temperature (from 200 to 400 °C), $H_2/CO_2$ molar ratio (from 2.0 to 4.3), and space velocity (from 48000 to 908000 $cm^3$ $h^{-1}$ $g_{cat}^{-1}$) were investigated. In the last case, reduced amounts of catalysts were also used (0.010-0.025 g); hence, appropriate quantities of quartz powder were added to keep the height of the catalytic bed (ca. 0.4 cm) unchanged. After 1 h on stream, on-line analysis of the reactor effluent was performed every hour (after removing water through an ice trap and a molecular sieves trap placed between the reactor outlet and the injection valve) on a GC 6890 (*Agilent*), equipped with a *HP Poraplot Q* capillary column and a TCD. The results of the quantitative analysis of the carbon-containing components were used for checking the carbon mass balance and for calculating $CO_2$ conversion and products selectivity.



**Fig. 2.2.** $CO_2$ to methane plant and gas analysis system (A); Reactor and furnace (B).

### 2.3.3. $CO_2$ conversion to methanol

$CO_2$ conversion to methanol was performed by using a *Microactivity-Effi* (produced by *PID Eng&Tech*) completely automated plant, made up of a stainless-steel (SS316) fixed-bed continuous-flow tubular microreactor ($\phi_{int}$ =0.9 cm; total length of 30.5 cm), designed to operate at high temperature and pressure. The reactor was also equipped with 3 mass flow

controllers for $CO_2$, $H_2$, and $N_2$ (used as internal standard), and a high-pressure Liquid/Gas (L/G) separator with a capacitive level sensor (Fig. 2.3).
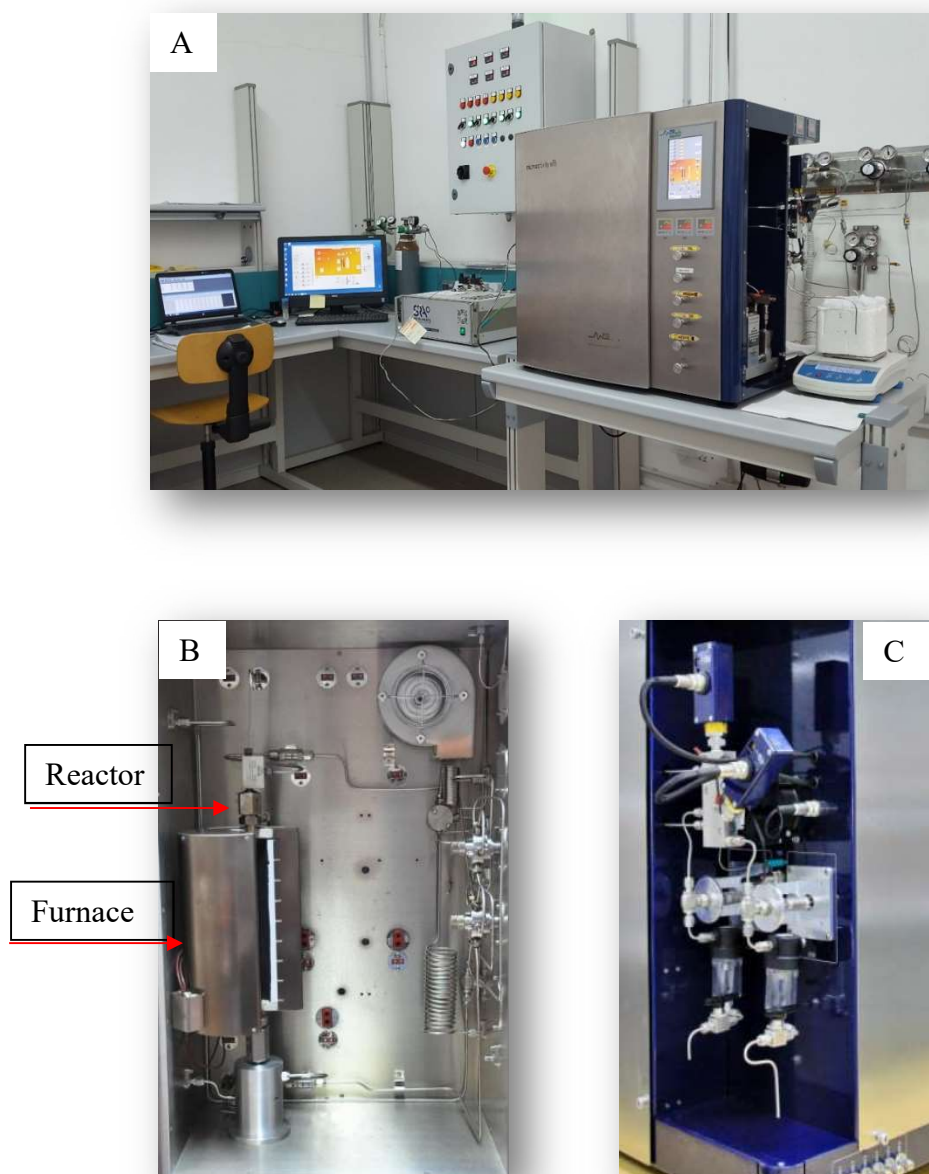


**Fig. 2.3.** $CO_2$ to methanol plant and gas analysis system (A); hot box (B); L/G separator (C).

Catalytic runs were performed at 250 °C for 48 h. In a typical test, 450 mg of catalyst (> 120 mesh) were placed into the reactor and pretreated with $N_2$ (150 $cm^3$ $min^{-1}$) at 250 °C (heating rate, 3 °C $min^{-1}$) and atmospheric pressure; then, the catalyst was reduced under $H_2$ flow (15 vol% in $N_2$; 275 $cm^3$ $min^{-1}$) at the same temperature for 2 h. After pressurisation of the reaction system at 30 bar (pressurisation rate, 1 bar $min^{-1}$), the gas flow was changed from $H_2/N_2$ to the reactant gas mixture ($CO_2$, 22.5 mol%; $H_2$, 67.5 mol%; $N_2$, 10 mol%), with a total flow rate of 330 $cm^3$ $min^{-1}$ and SV = 44000 $cm^3$ $h^{-1}$ $g_{cat}^{-1}$. The reactor effluent was sent to the high-pressure L/G separator, that allowed the condensable species (water and methanol) to be separated, recovered, and subsequently analysed by using a GC 7890A (*Agilent*), equipped with a *HP-5ms* column and coupled with a mass spectrometer (5977A, *Agilent*). The residual gas mixture was instead analysed by an on-line MicroGC R-3000 (*SRA Instruments*). The gas and liquid analyses revealed that the reactor effluent consisted of $CO_2$, $H_2$, $N_2$, CO, and $CH_3OH$, highlighting the formation of carbon monoxide and methanol as the only products. The results of the quantitative analysis of the carbon-containing components were used for checking the carbon mass balance and for calculating $CO_2$ conversion and products selectivity.

## *References*

[1]     A. Ungureanu, B. Dragoi,V. Hulea, T. Cacciaguerra, D. Meloni, V. Solinas, E. Dumitriu, *Micropor. Mesopor. Mat.* 163 (2012) 51.

[2]     L.-F. Xiao, F.-W. Li, J.-J. Peng, C.-G. Xia, *J. Mol. Catal. A: Chem.* 253 (2006) 265.

[3]     X. Zhang, D. Wang, N. Zhao, A.S.N. Al-Arifi, T. Aouak, Z.A. Al-Othman, W. Wei, Y. Sun, *Catal. Comm.* 11 (2009) 43.

[4]     W.-L. Dai, L. Chen, S.-F. Yin, S.-L. Luo, C.-T. Au, *Catal. Lett.* 135 (2010) 295.

[5]     D. Zhao, Q. Huo, J. Feng, B.F. Chmelka, G.D. Stucky GD, *J. Am. Chem. Soc.*, 120 (1998) 6024.

[6]     Y.-J. Wang, J.-M. Ma, M.-F. Luo, P. Fang, M. He, *J. Rare Earths* 25 (2007) 58.

[7]     M.-F. Luo, J.-M. Ma, J.-Q. Lu, Y.-P. Song, Y.-J. Wang, J. Catal. 246 (2007) 52.

[8]     F. Cavani, F. Trifirò, A. Vaccari, *Catal. Today* 11 (1991) 173.

[9]     H.P. Klug, L.E. Alexander, *X-Ray Diffraction Procedures*, Wiley (1962) New York.

[10]    F. Rouquerol, J. Rouquerol, K. Sing, P. Llewellyn, G. Maurin, *Adsorption by Powders and Porous Solids, Principles, Methodology and Applications*, Second Edition, Academic Press (2014) Amsterdam.

# Chapter III

# *CO$_2$ conversion to cyclic carbonates*

## 3.1. Introduction

The synthesis of cyclic carbonates through the reaction of $CO_2$ with epoxides represents a significant opportunity to decrease the carbon dioxide emissions, at the same time transforming such waste into valuable chemicals (Scheme 3.1). This reaction is at the basis of the industrial production, through which about 100 kt of cyclic carbonates are obtained per year; such value is also expected to increase, as the market of chemicals produced from cyclic carbonates (solvents, paint-strippers, lithium batteries, biodegradable packaging, etc.) is constantly expanding [1,2].
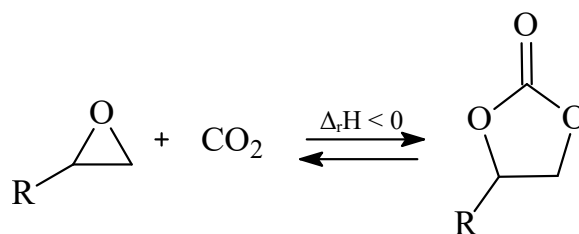


**Scheme 3.1.** $CO_2$ conversion into cyclic carbonates

The industrial process is carried out using mainly basic catalysts, which favour the opening of the epoxy ring and, consequently, the insertion of carbon dioxide. The classic industrial catalysts are mainly represented by ammonium or phosphonium salts, which require high temperature and pressure; in addition, they are generally difficult to recover and are used in quasi-equimolar amount with the substrate. For these reasons, the future challenge should be focused on finding active solid materials able to promote the $CO_2$ conversion in conditions very close to ambient temperature and pressure [1,3].

### 3.1.1. Catalysts for CO₂ conversion to cyclic carbonates

Numerous homogeneous and heterogeneous catalysts have been studied for the cycloaddition of $CO_2$ to epoxides. Homogeneous alternatives, such as phosphines [4,5], organic bases [6,7], organometallic complexes [8-10], and ionic liquids (ILs) [11-16], though showing a high catalytic activity, suffer of several disadvantages, related to their degradation, separation

processes and, consequently, reusability. In this regard, solid catalysts have to be considered as preferable, even though large efforts have to be done in order to increase their activity [1,17].

Metal oxides with basic properties represent an interesting option for catalysing $CO_2$ cycloaddition to epoxides, since they are relatively cheap and simple to prepare. Different metal oxides such as MgO, CaO, $ZrO_2$, ZnO, $Al_2O_3$, $CeO_2$ and $La_2O_3$ have been tested as catalysts for the cyclic carbonates production from $CO_2$. Promising results have been obtained by using MgO in the presence of DMF, which plays the twofold role of solvent and active species in the reaction mechanism [18]. Yamaguchi *et al.* [19] have shown that, in the presence of DMF, Mg-Al mixed oxides prepared by using hydrotalcites as precursors also provide interesting performances, due to the cooperation of acid and base sites in the epoxy ring opening. Such synergistic effect has also been confirmed by other studies carried out on Mg-Zn-Al mixed oxides [20] as well as on zeolites modified with alkali metals oxides, in the presence of suitable amounts of water [21,22]. Despite the large number of studies carried out in order to find solid materials able to promote the production of cyclic carbonates, heterogeneous catalysts are significantly less active than the homogeneous alternatives. In this regard, the immobilisation of organic bases and organometallic complexes on suitable supports can be considered as a good strategy to get high activity while solving problems related to separation and reusability of the homogeneous catalysts.

Nitrogen-based organic molecules, such as alkyl amines, adenine, and guanine, supported on different siliceous materials, like MCM-41 and SBA-15, have been found to be highly active for converting $CO_2$ into cyclic carbonates. Very good results were obtained by using Al_SBA-15 and Ti_SBA-15, since the introduction of $Al^{3+}$ or $Ti^{4+}$ enhances the acidic properties of the catalyst, promoting the epoxides adsorption and activation [6,23-25]. Good results have also been displayed by catalysts prepared by anchoring Cr- and Al-salen complexes on amino-functionalised $SiO_2$, ITQ-2, and MCM-41 [26-28], the need of solvents or co-catalysts and their poor reusability being the main drawbacks.

### 3.1.1.1. Supported Ionic Liquids-based catalysts

Different classes of ionic liquids (ILs) have showed a remarkable catalytic performance for the $CO_2$ conversion to organic carbonates, which include ILs based on quaternary ammonium [29], phosphonium or pyridinium [30], and imidazolium [31] salts. The reaction mechanism at the basis of the catalytic activity of such ionic liquids is depicted in Scheme 3.2

[32]. In the first step (1), the opening of the epoxy ring (a) occurs as a consequence of the nucleophilic attack by the anion species A⁻, the resulting intermediate (b) being stabilized by the interaction with the cationic moiety. Next, the insertion of $CO_2$ (2) leads to the formation of the (c) species, from which the formation of the 5-membered cyclic carbonate occurs as a result of the elimination mechanism, thus restoring the catalytic ionic couple ($[C]^+ A^-$) (3). From this mechanism clearly emerges the prominent role of the anionic species, which have to be good both as nucleophiles and leaving groups, the reason why halides are generally selected to get high performances. In addition, the role of the cationic moieties appears also important, being responsible for the stabilisation of the (c) and (b) intermediates. In this regard, the presence of suitable Lewis acid species has been indicated as beneficial, due to the coordination of the oxygen at the three-membered ring, which can favour the nucleophilic attack and then the ring opening of the epoxide [33,34].
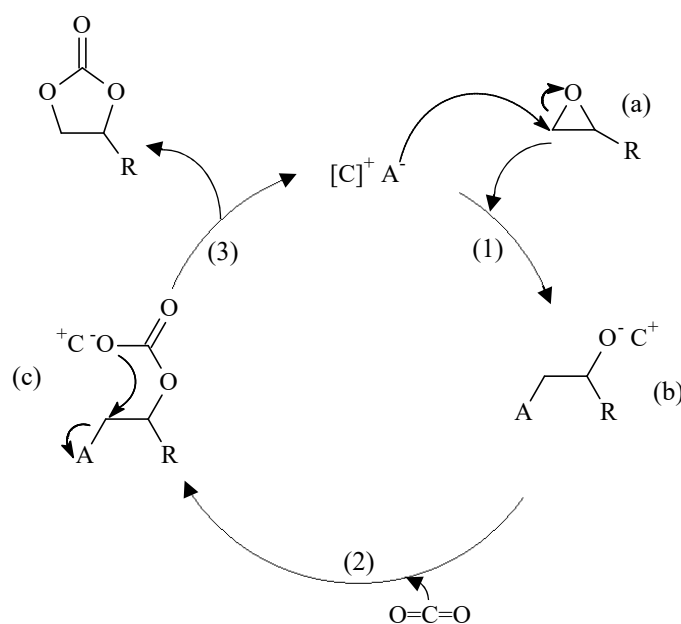


**Scheme 3.2.** Reaction mechanism for $CO_2$ cycloaddition to epoxide with ionic liquids ($[C^+] A^-$).

Since the reusability of the ionic liquids represents the main drawback, their immobilisation on suitable solid materials has attracted increasing interest [1,17,32,35]. Different catalysts have been prepared by anchoring imidazolium-based salts on polymer

matrices [36-39], with very interesting results obtained by using bio-polymers, such as chitosan, which appears as a very promising support thanks to the presence of several hydroxyl groups able to stabilize the (b) and (c) intermediates showed in Scheme 3.2 [40,41]. The use of 3-n-butyl-1-propyl-imidazolium grafted on $SiO_2$ has been reported by Xiao *et al*. in [42], where the influence of different metal salts acting as co-catalysts was also studied. The results indicated that high propylene carbonates yields are obtained by using $ZnCl_2$. However, a decrease in activity was observed for recycling tests as a consequence of the occurrence of leaching phenomena. The influence of different nucleophiles on the catalytic activity of functionalised imidazolium salts supported on silica catalysts has also been highlighted by Whang *et al*. [43]. High catalytic performances have been obtained by Dai *et al*. [44] on SBA-15 and Al_SBA-15 functionalised with 3-(2-hydroxyl-ethyl)-1-propylimidazolium bromide, though the occurrence of leaching was also observed to some extent up to three recycling tests.

### 3.1.2. Future perspectives and work purpose

Although cyclic carbonates synthesis through $CO_2$ conversion with epoxides is a well known and commercialised process, improvements in the catalytic systems are needed in order to make the reaction possible at mild temperature and pressure conditions. In addition, since the most active and used catalysts are homogeneous, large efforts should be focused on the development of suitable heterogeneous alternatives, which will have to combine high catalytic performance and reusability.

For this purpose, three Imi/*x*Al_SBA-15 catalysts were prepared (cf. par. 2.1.1) and tested in the $CO_2$ cycloaddition using different epoxides and reaction conditions. Since acidic sites can act as co-catalysts by favouring the epoxy ring opening, *x*Al_SBA-15 supports, where *x* represents the Si/Al molar ratio, were used to immobilise the imidazolium salt catalysts, aiming studying the influence of the Al content on the catalytic activity. In addition, recycling testing were also performed on selected samples for evaluating the materials reusability on multiple catalytic cycles.

## 3.2. Results and discussion

### 3.2.1. Chemical composition and $^{27}$Al MAS NMR analyses of *x*Al_SBA-15 supports

Tab. 3.1 reports the chemical composition of the *x*Al_SBA-15 supports. The ICP-AES results show that the experimental Si/Al values are in good agreement with the gel composition for all the prepared samples.

**Tab. 3.1.** Chemical composition of the *x*Al_SBA-15 supports.

| Sample | Si/Al (mol mol$^{-1}$) |
|---|---|
| 5Al_SBA-15 | 7 |
| 20Al_SBA-15 | 25 |
| 80Al_SBA-15 | 86 |

The $^{27}$Al MAS NMR spectra of the *x*Al_SBA-15 supports (Fig. 3.1) are characterised by broad peaks resulting from the superimposition of different contributions. In each spectrum, at least two signals are clearly visible, centred at about 53 and 0 ppm. According to the literature [45,46], the signal at 53 ppm can be ascribed to the framework Al atoms tetrahedrally coordinated, while the contribution at 0 ppm can be associated with octahedrally coordinated extra-framework Al species. In the case of 5Al_SBA-15, a signal centred at about 30 ppm is also observed, which, in agreement with some studies carried out on dealuminated zeolites [47,48], can be reasonable associated with the presence of additional extra-framework four- and/or five-coordinated Al species. However, at the current state, a clear attribution of the 30 ppm signal cannot be given. It is worth noting that, although not clearly visible, a contribution of these additional extra-framework Al species can be supposed also in the case of the 20Al_SBA-15 and 80Al_SBA-15 supports, since the profile of the corresponding peaks suggests the presence of more than two Al species. In light of the above, all the NMR profiles have been fitted by considering three contributions. A comparison of the framework aluminium content with the total one revealed that only 28, 25, and 17 % of the Al atoms can be considered incorporated in the silica structure of 5Al_SBA-15, 20_Al-SBA-15, and 80Al_SBA-15, respectively.
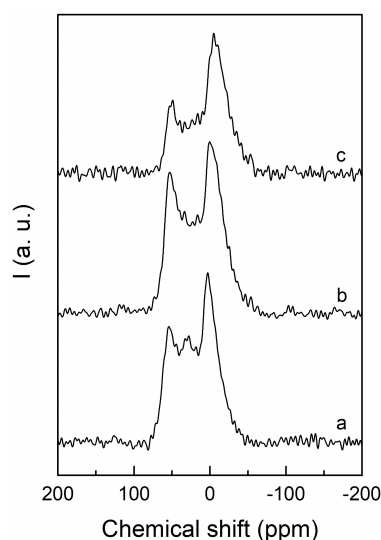
**Fig. 3.1.** ^{27}Al MAS NMR spectra of 5Al_SBA-15 (a), 20Al_SBA-15 (b), and 80Al_SBA-15 (c).

### 3.2.2. Chemical composition, structural and textural characterisation of Imi-catalysts

For the three Imi/*x*Al_SBA-15 catalysts, the imidazolium content, calculated from the amount of nitrogen determined by CHN analysis, is reported in Tab. 3.2, where the textural features of the catalysts and the corresponding supports are also reported. CHN results clearly indicate the increase in the imidazolium amount along with the Al content, suggesting that the functionalisation degree is more depending on the presence of aluminium rather than on the surface area and pore volume of the supports, which show an opposite trend with the same parameter.

**Tab. 3.2.** Imidazolium content and textural properties of the catalysts and corresponding supports.

| Sample | Amount of Imi (mmol $g_{cat}^{-1}$) | $S_{BET}$ (m² g⁻¹) | $V_P$ (cm³ g⁻¹) |
|---|---|---|---|
| 5Al_SBA-15 | - | 392 | 0.86 |
| Imi/5Al_SBA-15 | 1.06 | 243 | 0.51 |
| 20Al_SBA-15 | - | 409 | 0.94 |
| Imi/20Al_SBA-15 | 0.75 | 282 | 0.70 |
| 80Al_SBA-15 | - | 554 | 0.96 |
| Imi/80Al_SBA-15 | 0.55 | 349 | 0.81 |

## XRD

In Fig. 3.2 the low angle (LA) X-ray diffraction patterns of the $x$Al_SBA-15 supports and Imi/$x$Al_SBA-15 catalysts are reported. All the samples show three well-resolved peaks which can be indexed as the (100), (110), and (200) reflections associated with a hexagonal pore structure (space group *P6mm*). It is worth noting that no significant differences with respect to the corresponding supports can be observed for the Imi_catalysts, suggesting that the mesostructure is retained after the functionalisation procedure.
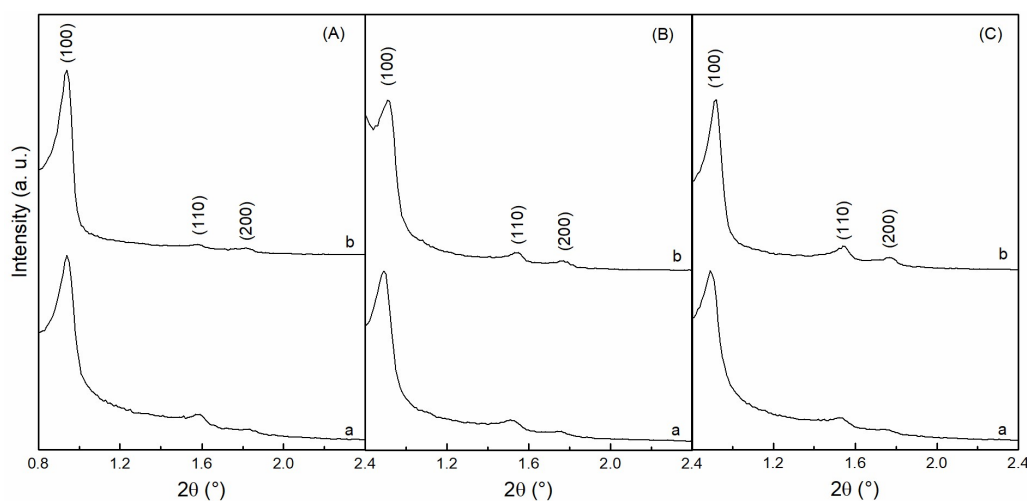


**Fig. 3.2.** Low angle X-ray diffraction patterns of the $x$Al_SBA-15 (a) supports and Imi/$x$Al_SBA-15 catalysts (b): (A) $x = 5$; (B) $x = 20$; (C) $x = 80$.

## N₂ adsorption/desorption

The N₂ physisorption results for the Imi/$x$Al_SBA-15 catalysts and the related supports are reported in Fig. 3.3. According to [49], all the isotherms can be classified as type IVa with a hysteresis loop at high relative pressures, typical for mesoporous materials. As expected, the functionalisation procedure induces a reduction in the surface area and porous volume values (Tab. 3.2). The pore size distribution (PSD) curves, obtained applying the BJH method to the desorption branch of the isotherms (inset), appear quite narrow for all the samples, though a shift toward lower pore size values is observed as a consequence of functionalisation. Such shift shows that anchoring of the imidazolium moieties occurs not only at the external surface of the carrier particles but also within the pores.
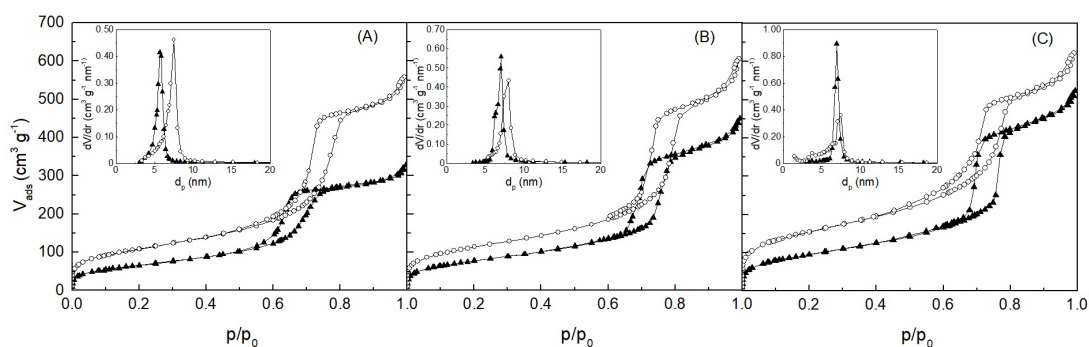
**Fig. 3.3.** $N_2$ adsorption/desorption isotherms and pore size distribution (inset) of the $x$Al_SBA-15 supports (○) and Imi/$x$Al_SBA-15 catalysts (▲): (A) $x$ = 5; (B) $x$ = 20; (C) $x$ = 80.

## $^{29}$Si CP-MAS NMR spectroscopy

In Fig. 3.4, the $^{29}$Si cross-polarisation magic-angle spinning (CP-MAS) spectra of the Imi/$x$Al_SBA-15 catalysts are reported. For all the spectra, two groups of signals ascribable to Q and T species (Scheme 3.3) can be observed at chemical shift values of about -110 and -65 ppm, respectively [50-52].
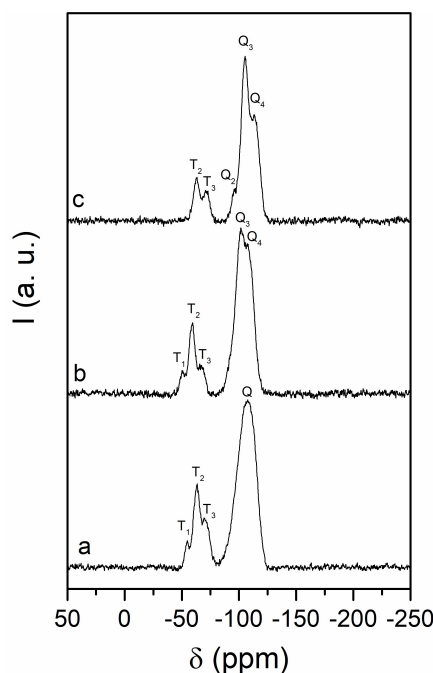


**Fig. 3.4.** $^{29}$Si CP-MAS NMR spectra of Imi/5Al_SBA-15 (a), Imi/20Al_SBA-15 (b), and Imi/80Al_SBA-15 (c).
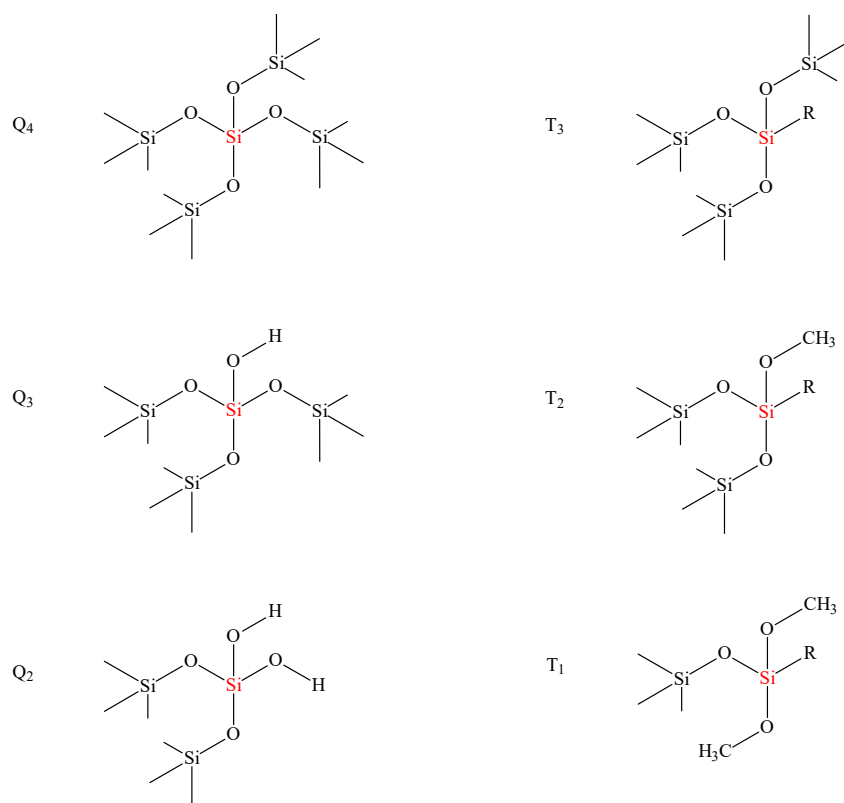
**Scheme 3.3.** Description of the Q and T species observable in the $^{29}$Si CP-MAS NMR spectra.

In the spectrum of Imi/5Al_SBA-15, a broad and asymmetric peak centred at about 108 ppm is present, for which it is not possible to distinguish the contributions of the different Q species. By converse, distinct $T_3$, $T_2$ and $T_1$ signals are observable, confirming that the organic groups are covalently bonded to the support surface. In the case of Imi/20Al_SBA-15, the $Q_4$ and $Q_3$ signals are clearly visible, though the presence of the $Q_2$ contribution can also be supposed by the tail of the peak toward the high chemical shift region. Also in this case, the $T_3$, $T_2$ and $T_1$ signals are well defined, confirming that the functionalisation procedure had been performed successfully. As for Imi/50Al_SBA-15, the $Q_4$, $Q_3$, and $Q_2$ contributes are all identifiable, whereas, unlike the other Imi-catalysts, the $T_1$ signal is not observed, suggesting that the low aluminium content of the support guarantees a large concentration of vicinal silanols available to anchor the imidazolium moieties.

### 3.2.3. NH₃ adsorption microcalorimetry

As already mentioned, materials characterised by suitable acidic properties can improve the activity of the imidazolium-based catalysts. Indeed, acid sites can act as co-catalysts, promoting the epoxide ring opening and, as a consequence, favouring the insertion of $CO_2$ (cf. Scheme 3.2). For this reason, the acidic properties of the bare $x$Al/SBA-15 have been studied by means of NH₃-adsorption microcalorimetric measurements. In Fig. 3.5, the differential heat of adsorption ($Q_{diff}$) is reported as a function of the ammonia uptake for all the prepared supports. The results for the pure SBA-15 have also been reported for comparison.
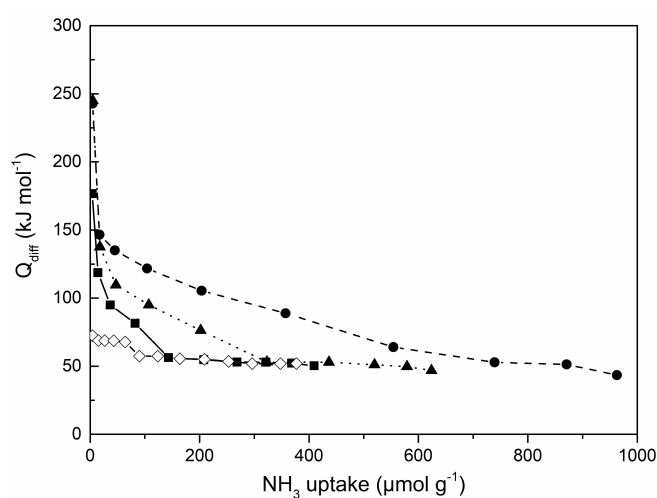


**Fig. 3.5.** Differential heat versus NH₃ uptake at 80 °C for SBA-15 (◇), 5Al_SBA-15 (●), 20Al_SBA-15 (▲), and 80Al_SBA-15 (■).

All the $x$Al/SBA-15 samples show acidic properties significantly more pronounced with respect to SBA-15, both in terms of number and strength of sites. $Q_{diff}$ initial values very close to 250 kJ mol $^{-1}$ can be observed for 5Al_SBA-15 and 20Al_SBA-15, revealing the presence of strong acidic sites. As for 80Al_SBA-15, the initial $Q_{diff}$ is lower than those of the other supports (*ca.* 175 kJ mol$^{-1}$), even though it remains remarkably higher compared to that of the pure SBA-15. For all the $x$Al_SBA-15 supports, $Q_{diff}$ decreases as the NH₃ uptake increases, thus indicating a high heterogeneity of the adsorbing sites. In agreement with previous studies on pure silica samples [53,54], $Q_{diff}$ value indicative of non-specific and/or physical adsorption has been chosen as the initial value (72 kJ mol$^{-1}$) obtained for SBA-15, on which only very weak adsorbent-adsorbate interactions are supposed to occur. Accordingly, for all the Al-containing

supports, the fraction of ammonia uptake corresponding to differential heats below 72 kJ mol$^{-1}$ has been neglected in estimating the total acid sites number, which resulted equal to 97, 205, and 464 µmol g$^{-1}$ for 80Al_SBA-15, 20Al_SBA-15, and 5Al_SBA-15, respectively. As expected, the results clearly show the presence of acidity on the *x*Al_SBA-15 materials, which increases with the increase in the Al content, confirming that the prepared materials are suitable to be used as supports for imidazolium salts-based catalysts.

### 3.2.4. Catalytic results

Catalytic tests for the $CO_2$ cycloaddition to epichlorohydrin were performed in a batch reactor at 125 °C and an initial $CO_2$ pressure of 25 bar, by using 0.3 g of catalyst and 24 cm$^3$ of epoxide. For each Imi/*x*Al_SBA-15 catalyst, two recycling tests were also performed in the same conditions. Catalytic results after three hours of reaction are reported in Tab. 3.3.

**Tab. 3.3.** Catalytic results for the Imi/*x*Al_SBA-15 samples. Reaction condition: T = 125 °C; P$_{CO_2,in}$ = 25 bar; m$_{cat}$ = 0.3 g; 24 cm$^3$ of epichlorohydrin; time of reaction: 3 h.

| Sample | Catalytic test | Epoxide conversion (mol%) | Carbonate selectivity (mol%) |
|---|---|---|---|
| Imi/5Al_SBA-15 | [a]1 | 75 | > 99 |
| | [b]2 | 59 | > 99 |
| | [c]3 | 60 | > 99 |
| Imi/20Al_SBA-15 | [a]1 | 76 | > 99 |
| | [b]2 | 57 | > 99 |
| | [c]3 | 57 | > 99 |
| Imi/80Al_SBA-15 | [a]1 | 62 | > 99 |
| | [b]2 | 43 | > 99 |
| | [c]3 | 44 | > 99 |

[a]1: first catalytic testing on fresh Imi/*x*Al_SBA-15; [b]2 and [c]3: 1st and 2nd reuse.

The results clearly show that all the catalysts are active in the cycloaddition of $CO_2$ to epichlorohydrin, though a decrease in epoxide conversion is observed between the first and the second recycling test. This could be due to a contribution, during the first run, of homogeneous

catalysis by "free" imidazolium species, which could be originated by leaching phenomena and/or by the release of imidazolium salts not anchored on the support but not effectively removed during the washing steps of the synthesis procedure. However, data in Tab. 3.3 show that activity remains constant after the first reuse, indicating the complete removal of homogeneous catalysts and that interactions between the remaining imidazolium moieties and the surface of the support are strong enough to prevent a further leaching of the active species. CHN analyses were carried out on the catalysts recovered after the second recycling run for determining the amount of the residual imidazolium content and to calculate the turnover number ($TON_{imi}$) for the fresh and the reused samples. The pertinent results are reported in Tab. 3.4 and support the view of the decrease in $CO_2$ conversion as a consequence of the loss of imidazolium species. Nevertheless, the comparable $TON_{imi}$ values of the fresh and the reused catalysts, calculated as moles of epoxide converted per mole of imidazolium, indicate that the very high specific activity of the imidazolium sites is preserved during the multiple catalytic cycles. Interestingly, despite the higher imidazolium content with respect to the other samples, the Imi/5Al_SBA-15 catalyst is characterised by the lower turnover number, suggesting that the imidazolium specific activity might be affected by the Al content and/or that a fraction of imidazolium salts might be unnecessary for converting the epoxide at the current reaction condition.

**Tab. 3.4.** Catalytic activities comparison between fresh and used Imi/*x*Al_SBA-15 catalysts.

| Sample | Catalytic test | Amount of Imi (mmol $g_{cat}^{-1}$) | *$TON_{imi}$ |
|---|---|---|---|
| Imi/5Al_SBA-15 | [a]1 | 1.06 | 717 |
| | [b]3 | 0.86 | 709 |
| Imi/20Al_SBA-15 | [a]1 | 0.75 | 1043 |
| | [c]3 | 0.55 | 1048 |
| Imi/80Al_SBA-15 | [a]1 | 0.55 | 1152 |
| | [c]3 | 0.41 | 1104 |

[a]1: catalytic testing on catalyst fresh; [c]3: 2nd reuse.

*turnover number ($TON_{imi}$) calculated as moles of epoxide converted/moles of imidazolium active sites.

In order to confirm the previously observed catalytic performance, $CO_2$ cycloaddition to epichlorohydrin was also performed at 100 °C on the Imi/20Al_SBA-15 catalyst. The pertinent results are reported in Tab. 3.5. As expected, a diminution in epoxide conversion is observed as a consequence of the decrease in the reaction temperature. In addition, although to a lesser extent compared to the results obtained at 125 °C, conversion decreases after the first use. Notwithstanding, the ability of the catalyst in promoting the cycloaddition reaction is confirmed also at lower temperatures.

**Tab. 3.5.** Catalytic results for Imi/20Al_SBA-15. Reaction condition: T = 100 °C; $P_{CO_{2,in}}$ = 25 bar; $m_{cat}$ = 0.3 g; 24 cm³ of epichlorohydrin; time of reaction : 3 h.

| Sample | Catalytic test | Amount of Imi (mmol $g_{cat}^{-1}$) | Epoxide conversion (mol%) | *TON$_{imi}$ |
|---|---|---|---|---|
| Imi/20Al_SBA-15 | [a]1 | 0.75 | 24 | 327 |
| | [b]2 | n.d. | 20 | n.d. |
| | [c]3 | 0.62 | 19 | 316 |

[a]1: catalytic testing on catalyst fresh; [b]2 and [c]3: 1st and 2nd reuse. n.d.: not determined.

*turnover number (TON$_{imi}$) calculated as moles of epoxide converted/moles of imidazolium active sites.

Additional tests were also performed with styrene oxide, which is notoriously less reactive than epichlorohydrin. Moreover, the corresponding cyclic carbonate (styrene carbonate) is a very required product, since it is widely used as an nonaqueous electrolyte in lithium secondary batteries and in the synthesis of aromatic carbamates, dialkyl carbonates, vicinal diols, beta-amino alcohols, thermoplastic aromatic polycarbonates, non-isocyanate polyurethanes, and aliphatic polycarbonate polyols [55]. Catalytic results obtained at 125 °C by using Imi/20Al_SBA-15 are reported in Tab. 3.6.

**Tab. 3.6.** Catalytic results for Imi/20Al_SBA-15. Reaction condition: T = 125 °C; $P_{CO_{2,in}}$ = 25 bar; $m_{cat}$ = 0.3 g; 24 cm³ of styrene oxide; time of reaction : 3 h.

| Sample | Catalytic test | Amount of Imi (mmol $g_{cat}^{-1}$) | Epoxide conversion (mol%) | *TON$_{imi}$ |
|---|---|---|---|---|
| Imi/20Al_SBA-15 | [a]1 | 0.75 | 18 | 172 |
| | [b]2 | 0.74 | 18 | 174 |

[a]1: catalytic testing on catalyst fresh; [b]2: 1st reuse.

*turnover number (TON$_{imi}$) calculated as moles of epoxide converted/moles of imidazolium active sites.

Unlike what was noted by using epichlorohydrin (Tab 3.4), no decrease in activity is observed in the recycling test when using styrene oxide. This seems to indicate that no leaching phenomena occur in the presence of such oxide, and that all the organic active phase is anchored to the surface of the support, confirming that the catalysts were successfully prepared. According to the above, it can be proposed that the decrease in activity observed when epichlorohydrin is used as the reactant can be ascribed to the occurrence of leaching phenomena rather than to the removal of imidazolium species which are not anchored on the silica surface during the synthesis procedure. The different behaviour observed in the presence of epichlorohydrin or styrene oxide in the reaction medium suggests that the epoxide nature can influence the detachment of the imidazolium moieties more weakly bonded to the support.

## 3.3. Conclusions

In this study, three $x$Al_SBA-15 materials were prepared and used as supports for imidazolium salts-based catalysts. CHN analyses showed that the Si/Al molar ratio affects the functionalisation degree, which increases along with the Al content.

As highlighted by the calculated $TON_{imi}$ values, all the prepared Imi/$x$Al_SBA-15 samples are highly active in the $CO_2$ conversion with epichlorohydrin. A decrease in activity was observed for the used catalysts as a consequence of leaching phenomena. However, epoxide conversion values remain unchanged after the first reuse, pointing out the maintenance of the catalytic performances in the additional catalytic cycles. A different catalytic behaviour was observed depending on the Si/Al molar ratio. Indeed, an unexpected low $TON_{imi}$ value was calculated for the Imi/5Al_SBA-15 sample despite the high imidazolium content. Such decrease in specific activity might be due to an effect of the Al content or to the presence of excess imidazolium moieties, not necessary for the epoxide conversion in the used reaction conditions. In order to better understand the role of the Si/Al ratio on the catalytic performance as well as that of a surplus concentration of imidazolium, further studies should be performed on ad-hoc prepared Imi/$x$Al_SBA-15 materials.

The results obtained by using styrene oxide allow excluding the presence of "free" imidazolium species in the fresh catalysts, confirming that the samples were successfully prepared and usable in multiple catalytic cycles.

## *References*

[1]     M. North, R. Pasquale, C. Young, *Green Chem.* 12 (2010) 1514.

[2]     M. Aresta, *Carbon Dioxide as Chemical Feedstock*, WILEY-VCH (2010) Weinheim.

[3]     P. Styring, E. A. Quadrelli, K. Armstrong, *Carbon Dioxide Utilisation-Closing the carbon cycle*, ELSEVIER (2015).

[4]     H.S. Kim, J.Y. Bae, J.S. Lee, O.S. Kwon, P. Jelliarko, S.D. Lee, S.H. Lee, *J. Catal.* 232 (2005) 80.

[5]     J. Sun, L. Wang, S.J. Zhang, Z.X. Li, X.P. Zhang, W.B. Dai, R. Mori, *J. Mol. Catal. A: Chem.* 256 (2006) 295.

[6]     A. Barbarini, R. Maggi, A. Mazzacani, G. Mori, G. Sartori, R. Sartorio, *Tetrahedron Lett.* 44 (2003) 2931.

[7]     J.L. Jiang, R.M. Hua, *Synth. Commun.* 36 (2006) 3141.

[8]     R.L. Paddock, Y. Hiyama, J.M. Mckay, S.T. Nguyen, *Tetrahedron Lett.* 45 (2004) 2023.

[9]     R. Srivastava, T.H. Bennur, D. Srinivas, *J. Mol. Catal. A: Chem.* 226 (2005) 199.

[10]    Z.W. Bu, G. Qin, S.K. Cao, *J. Mol. Catal. A: Chem.* 277 (2007) 35.

[11]    V. Cáló, A. Nacci, A. Monopoli, A. Fanizzi, *Org. Lett.* 4 (2002) 2561.

[12]    J. Sun, S. Fujita, M. Arai, *J. Organomet. Chem.* 690 (2005) 3490.

[13]    Y.X. Zhou, S.Q. Hu, X.M. Ma, S.G. Liang, T. Jiang, B.X. Han, *J. Mol. Catal. A: Chem.* 284 (2008) 52.

[14]    J. Sun, J.Y. Ren, S.J. Zhang, W.G. Cheng, *Tetrahedron Lett.* 50 (2009) 423.

[15]    F. Jutz, J.-M. Andanson and A. Baiker, *Chem. Rev.* 111 (2011) 322.

[16]    J.Q. Wang, W.G. Cheng, J. Sun, T.Y. Shi, X.P. Zhang, S.J. Zhang, *RSC Adv.* 4 (2014) 2360.

[17]    W.-L. Dai, S.-L. Luo, S.-F. Yin, C.-T. Au, *Appl. Catal A: Gen.* 366 (2009) 2.

[18]    B.M. Bhanage, S.I. Fujita, Y. Ikushima, M. Arai, *Appl. Catal. A: Gen.* 219 (2001) 259.

[19]    K. Yamaguchi, K. Ebitani, T. Yoshida, H. Yoshida, K. Kaneda, *J. Am. Chem. Soc.* 121 (1999) 4526.

[20]    S.F. Yin, W.L. Dai, S.L. Luo, S.S. Wu, X.W. Zhang, W.S. Li, CN 101265253 (patent).

[21]    E.J. Doskocil, *Micropor. Mesopor. Mat.* 76 (2004) 177.

[22]    E.J. Doskocil, *J. Phys. Chem. B* 109 (2005) 2315.

[23]    R. Srivastava, D. Srinivas, P. Ratnasamy, *J. Catal.* 233 (2005) 1.

[24]    R. Srivastava, D. Srinivas, P. Ratnasamy*, Micropor. Mesopor. Mater.* 90 (2006) 314.

[25]    D. Srinivas, P. Ratnasamy, *Micropor. Mesopor. Mat.* 105 (2007) 170.

[26]    C. Baleizâo, B. Gigante, M.J. Sabater, H. García, A. Corma, *Appl. Catal. A: Gen.* 228 (2002) 279.

[27]    M. Alvaro, C. Baleizâo, D. Das, E. Carbonell, H. García, *J. Catal.* 228 (2004) 254.

[28]    M. Ramin, F. Jutz, J.D. Grunwaldt, A. Baiker, *J. Mol. Catal. A: Chem.* 242 (2005) 32.

[29]    A. Nacci, A. Monopoli, A. Fanizzi, *Org. Lett.* (2002) 1552.

[30]    W.L. Wong, P.H. Chan, Z.Y. Zhou, K.H. Lee, K.C. Cheung, K.Y. Wong, *ChemSusChem* 1 (2008) 67.

[31]    H. Kawanami, A. Sasaki, K. Matsui, Y. Ikushima, *Chem. Commun.* (2003) 896.

[32]    F.D. Bobbink, P.J. Dyson, *J. Catal.* 343 (2016) 52.

[33]    M. North, R. Pasquale, *Angew. Chem. Int. Ed.* 48 (2009) 2946.

[34]    P.P. Pescarmona, M. Taherimehr, *Catal. Sci. Technol.* 2 (2012) 2169.

[35]    M. Buaki-Sogo, H. Garcia, C. Aprile, *Catal. Sci. Technol.* 5 (2012) 1222.

[36]  Y. Xie, Z. Zhang, T. Jiang, J. He, B. Han, T. Wu, K. Ding, *Angew. Chem., Int. Ed.* 46 (2007) 7255.

[37]  W.-L. Dai, L. Chen, S.-F. Yin, W.-H. Li, Y.-Y. Zhang, S.-L. Luo, C.-T. Au, *Catal. Lett.* 137 (2010) 74.

[38]  R.A. Watile, K.M. Deshmukh, K.P. Dhake, B.M. Bhanage, *Catal. Sci. Technol.* 2 (2012) 1051.

[39]  T.-Y. Shi, J.-Q. Wang, J. Sun, M.-H. Wang, W.-G. Cheng, S.-J. Zhang, *RSC Adv.* 3 (2013) 3726.

[40]  J. Sun, J. Wang, W. Cheng, J. Zhang, X. Li, S. Zhang, Y. She, *Green Chem.* 14 (2012) 654.

[41]  K.R. Roshan, G. Mathai, J. Kim, J. Tharun, G.-A. Park, D.-W. Park, *Green Chem.* 14 (2012) 2933.

[42]  L.F. Xiao, F.W. Li, J.J. Peng, C.G. Xia, *J. Mol. Catal. A: Chem.* 253 (2006) 265.

[43]  J.Q. Wang, X.D. Yue, F. Cai, L.N. He, *Catal. Commun.* 8 (2007) 167.

[44]  W.-L. Dai, L. Chen, S.-F. Yin, S.-L. Luo, C.-T. Au, *Catal. Lett.* 135 (2010) 295.

[45]  R.B. Borade, A. Clearfield, *Catal. Lett.* 31 (1995) 267.

[46]  K.R. Kloetstra, H.W. Zandbergen, H. van Bekkum, *Catal. Lett*. 33 (1995) 157.

[47]  J. Chen, T. Chen, N Guan, J. Wang, *Catal. Today* 93-95 (2004) 627.

[48]  S. Li, A. Zheng, Y. Su, H. Fang, W. Shen, Z. Yu, L.Chen, F. Deng, *Phys. Chem. Chem. Phys.* 12 (2010) 3895.

[49]  F. Rouquerol, J. Rouquerol, K. Sing, P. Llewellyn, G. Maurin, *Adsorption by Powders and Porous Solids, Principles, Methodology and Applications*, Second Edition, Academic Press (2014) Amsterdam.

[50]  N. Godard, A. Vivian, L. Fusaro, L. Cannavicci, C. Aprile, D. P. Debecker, *ChemCatChem* 9 (2011) 2211.

[51]  V. Hiremath, A. H. Jadhav, H. Lee, S. Kwon, J. G. Seo, *Chem. Eng. J.* 287 (2016) 602.

[52]  V. Elumalai, S. Dharmalingam, *Micropor. Mesopor. Mat.* 236 (2016) 260.

[53]    G. Colón, I. Ferino, E. Rombi, E. Selli, L. Forni, P. Magnoux, M. Guisnet, *Appl. Catal. A: Gen.* 168 (1998) 81.

[54]    D. Meloni, D. Perra, R. Monaci, M.G. Cutrufello, E. Rombi, I. Ferino, *Appl. Catal. B: Environ.* 184 (2016) 163.

[55]    K. Jasiak, T. Krawczyk, M. Pawlyta, A.Jakóbik-Kolon, S. Baj, *Catal. Lett.* 146 (2016) 893.

## Chapter IV


# CO<sub>2</sub> conversion to methane

## 4.1. Introduction

The use of $CO_2$ as a C1 building block for producing fuels is attracting growing attention as a complementary alternative for the reduction of greenhouse emissions and, at the same time, the preservation of natural resources for the future generations. At this purpose, the production of $CH_4$ through $CO_2$ hydrogenation (known as *"Sabatier"* or *"methanation"* reaction) is considered a promising process, especially if the required hydrogen is produced from renewable resources. $CO_2$ methanation allows $H_2$ to be transformed into a substance compatible with the existent technologies; in fact, methane could be directly injected into already existent pipelines networks or storage infrastructures, making $CO_2$ methanation a highly attractive strategy.

$CO_2$ hydrogenation to methane is an exothermic reaction that occurs with a significant volume contraction (Eq 4.1).

$$CO_2 \; + \; 4H_2 \; \rightleftharpoons \; CH_4 \; + \; 2H_2O_{(g)} \qquad \Delta_r H_{298K} = -164 \text{ kJ mol}^{-1} \qquad \text{(Eq. 4.1)}$$

Considering both the strong exothermic character and the increase in entropy associated with the reaction, the achievement of high $CH_4$ yields at atmospheric pressure requires reaction temperatures not exceeding 300 °C. However, due to significant kinetic limitations which make difficult the eight-electron reduction of $CO_2$ to $CH_4$ by hydrogen, catalysts with high activity are needed to get satisfactory reaction rate and methane selectivity [1]. Although the conversion of carbon dioxide to methane is a well-established process for which the commercialisation on industrial-scale has already been realised, numerous efforts have to be still made in order to find catalysts able to give high performance at mid-temperature conditions.

### 4.1.1. Reaction mechanisms

Although several studies have been published in recent past, the debate concerning the possible reaction mechanisms of $CO_2$ methanation still remains open, mainly because of the uncertainly in determining the intermediate species involved in the rate determining step [2,3]. Nevertheless, two main reaction paths were identified for $CO_2$ methanation [4]. The first route involves the conversion of $CO_2$ to CO through the *Reverse Water Gas Shift* (RWGS) reaction, followed by its reduction to $CH_4$ through the same mechanism implicated in CO methanation;

conversely, the second one concerns the direct $CO_2$ hydrogenation to $CH_4$ through the formation of carbonates and formates as reaction intermediates. Both paths appear to be possible from a mechanistic point of view, with the preference of one rather than the other that strictly depends on the catalyst properties (such as composition and structural or morphologic features) and reaction conditions (such as temperature and pressure).

## 4.1.2. Catalysts for $CO_2$ conversion to methane

Numerous metal-based catalysts have been used for the conversion of CO and $CO_2$ into methane. Among these, different noble-metals such as Ru, Rh, and Pd have shown a high performance in the reaction, though their use on industrial-scale is not so attracting due to their high cost. From this point of view, Ni-based catalysts are preferable, as they combine a high catalytic activity with affordable costs.

Besides the nature of active metals, also synthesis methods and promoters are crucial for obtaining high performance catalysts. In addition, the used supports should be characterised by a large surface area to guarantee high metal dispersion. In this respect, different mixed oxides have been used as supports for methanation catalysts, among which $\gamma$-$Al_2O_3$, $SiO_2$, $TiO_2$, $CeO_2$, and $ZrO_2$ are the most investigated [4-6].

### 4.1.2.1. Noble metals-based catalysts

Ru-based mixed oxides have been reported as the more active methanation catalysts, leading to high $CO_2$ conversion and $CH_4$ selectivity at relatively low temperatures [7]. In addition, compared to the alternatives, they are probably the most stable catalysts, being highly resistant to sintering phenomena in a wide range of temperatures [8]. Several studies have shown that the performance of Ru-based catalysts principally depends on the dispersion of the metallic phase, on the type of the support, and on the use of suitable modifiers/promoters that can chemically interact with the metal [4]. The catalytic activity of the Ru-based catalysts has been investigated by using different supports [9,10] including $Al_2O_3$, $TiO_2$, $SiO_2$, MgO, $MgAl_2O_3$, C, and $CeO_2$/$ZrO_2$. $CeO_2$ can play a significant role in $CO_2$ conversion processes, due to the presence of oxygen vacancies that can promote its activation. In this regard, the addition of $CeO_2$ to Ru/$\gamma$-$Al_2O_3$ resulted in an increased catalytic activity, due to the fast reaction between hydrogen, activated on the metallic sites, and reaction intermediates

originating by $CO_2$-adsorption on the ceria sites (carbonates and formates) [11]. A promising catalytic performance was also obtained at 450 °C by using ceria doped with Ru, with $CO_2$ conversion and $CH_4$ selectivity significantly higher than those of analogous systems doped with Ni, Co, or Pd [12].

Various Rh-supported catalysts have also been investigated for the conversion of $CO_2$ to methane [5]. Rh/γ-$Al_2O_3$ was indicated as a very efficient catalyst, in which the oxidation state of rhodium plays a crucial role on the species distribution on the catalyst surface; in addition, it was reported that the Rh particles sizes does not influence catalytic activity at high temperature, while an increase in the intrinsic activity was observed between 130 and 150 °C for the larger particles in comparison with the smaller ones [13,14]. Swalus *et al.* showed a promising increase in methanation activity by mechanical mixing of Rh/γ-$Al_2O_3$ and Ni/active carbon, thanks to their synergistic action in $CO_2$ and $H_2$ activation [15]. Rh/$TiO_2$ is considered one of the most active Rh-based catalyst, probably due to the formation of strong Rh-support interactions which can allow the energetic barrier for the $CO_2$ activation to be lowered [16]. Nevertheless, a widespread of this catalyst on industrial scale is hindered by the high Rh cost.

Among the noble metals, also Pd has also shown a good catalytic performance in $CO_2$ methanation, due to its ability to effectively activate the $H_2$ required for the reduction reactions [4]. The catalytic behaviour of Pd/$Al_2O_3$- and Pd/MWCNT-based (MultiWall Carbon NanoTube) bifunctional catalysts was studied by Kwak *et al*. [17], who reported that methanation can only occur in the presence of metal oxides able to activate $CO_2$. In addition, their results clearly highlighted the dependence of activity and selectivity on the Pd dispersion, showing that CO was the main product on catalysts containing Pd in atomic dispersion, probably due to the absence of sites able to activate carbon monoxide for a further reduction; on the contrary, selectivity significantly shifted towards $CH_4$ in the presence of Pd clusters.

### 4.1.2.2. Nickel-based catalysts

As already pointed out, Ni-based materials represent the best option as catalysts for $CO_2$ methanation. In fact, the Ni-based mixed oxides are characterised by high availability and low cost, while guaranteeing a high catalytic performance. For this reason, Ni-based catalysts have been the subject of a huge number of studies, manly concerning with the use of different preparation methods, supports, and promoters [4,5].

Alumina is probably the most investigated support, with $Ni/Al_2O_3$ catalysts showing high catalytic performance despite the presence of deactivation, due both to the formation of carbonaceous deposit and the sintering of the Ni-particles. A mesoporous nanocrystalline $\gamma$-$Al_2O_3$ with high surface area was used as the support to prepare different Ni-based catalysts by impregnation method [18]; the influence of the nickel content and of the calcination temperature on the catalytic activity was investigated, the best results being obtained, at relatively low temperatures (from 200 to 350 °C), with a Ni content of 20 wt%. The use of $Ni/Al_2O_3$ catalysts prepared via the Ni-Al hydrotalcite precursor was discussed by He *et al.* [19]; the authors showed that the presence of strong basic sites, originating from the formation of the Ni-O-Al structure, positively affects $CO_2$ conversion and $CH_4$ selectivity.

In order to improve the performance of the $Ni/Al_2O_3$ catalysts, the use of different promoters, such as $CeO_2$, $MnO_2$, $IrO_2$, and $La_2O_3$, was also investigated [20]. Among these, $CeO_2$ appeared the most promising, as it improved the $Al_2O_3$ thermal stability and the Ni dispersion, and promoted the metal-support interactions [4].

Mesostructured silicas, such as MSN (Mesostructured Silica Nanoparticles), MCM-41, and SBA-15, have recently been tested as supports for Ni-based catalyst [4,5]; among these, MSN seems the most promising. Ni/MSN catalysts prepared by impregnation method were used for the $CO_2$ methanation process at temperatures ranging from 150 °C to 450 °C; the better catalytic performance, deriving from the use of MSN as the support with respect to MCM-41, HY, $SiO_2$, and $\gamma$-$Al_2O_3$, was explained by the observed higher concentration of basic sites, which are considered responsible for the activation of $CO_2$ [21]. The effect of the Ni content was also investigated by Aziz *et al.* [22]. The experimental results showed that, although the dispersion of the active phase worsens with the increase in Ni content, catalytic activity follows the opposite trend. This behaviour was explained by considering the increase in the catalyst basicity along with the Ni content, thus underling the prominent role of basic sites in the range of the investigated Ni concentrations (1-10 wt% of Ni).

$ZrO_2$ is considered a suitable support for Ni-based catalyst thanks to its acidic/basic properties and $CO/CO_2$ adsorption capability. The catalytic performance of $Ni/ZrO_2$ systems strictly depends on the zirconia phase, with the presence of tetragonal $ZrO_2$ which is reported to positively affect their catalytic activity. Moreover, the $Ni/ZrO_2$ catalytic performance was also found to increase with the addition of rare-earth elements such as Yb and Sm, though the best results were obtained by adding $CeO_2$ [4].

The function of ceria as the support/promoter in the formulation of Ni-based catalysts can be explained by its high oxygen storage capacity and by the ability to strongly interact with Ni, which can favour an efficient dispersion of the primary active phase [23]. Interesting observations on the role of ceria in $CO_2$ methanation were presented by Ussa Aldana *et al.* through the study of the reaction mechanism on Ni/CeO₂-ZrO₂ catalysts [24]. By using FTIR measurements, the authors showed that $CO_2$ is adsorbed on defective sites of ceria through the formation of hydrogen-carbonates and carbonates (mono- and bi-dentate), whose presence was considered a clear evidence that the reaction mechanism does not involve CO as the intermediate, given that such oxygenated species can be directly hydrogenated to form formates and finally $CH_4$.

## 4.1.3. Future perspectives and work purpose

The chemical recycling of $CO_2$ to methane have to be considered as a crucial strategy to reduce carbon dioxide emissions and to meet the criteria of sustainability. In this light, the scientific community has presented various strategies in the attempt to solve the issues related to the economical and energetic aspects of the process, as well as to find better catalytic systems.

Presently, Ni-based catalysts are the best option for the $CO_2$ methanation, though further improvements are needed to achieve higher activity, especially at relative low temperatures. For this reason, the future research direction should be focused on exploring new synthesis procedures, through which materials with high surface area, as well as high dispersion and stability of the active phase can be obtained. Furthermore, the addition of components that can synergistically work with the primary active phase in the reactants activation, or through which the basic properties of the catalyst can be tailored, should be also investigated.

In this thesis work, the conversion of $CO_2$ to methane was studied on NiO/CeO₂ mixed oxides, prepared with two different unconventional synthesis approaches (par. 2.1.2). The first series of catalysts was prepared by using the "*Hard-Template*" method, while the second one was obtained by means of the "*Soft-Template*" strategy. The synthesis approaches were both chosen with the aim to develop efficient catalysts with high surface area and Ni dispersion. CeO₂ was selected as it is considered one of the most important oxides used as the support for metal-based catalysts. Cerium oxide catalytic activity is strictly correlated to its reducibility, its oxygen storage capacity, and the presence of oxygen vacancies, which can affect the dispersion,

morphology, and electronic properties of the supported metals, hence improving their catalytic activity. In this regard, to better understand the support influence on the catalytic performance, $CO_2$ methanation was also performed on a $NiO/\gamma Al_2O_3$ mixed oxide, being $\gamma$-alumina the most used support on a commercial-scale.

## 4.2. *Hard-Templated x*NiO/CeO₂

### 4.2.1. Characterisation of SBA-15

SBA-15 was used as the template for the synthesis of the $NiO/CeO_2\_HT$ mixed oxides and the $CeO_2\_HT$ support.

The low angle (LA) X-ray diffraction pattern of SBA-15 is reported in Fig. 4.1. The pattern clearly shows three well-resolved peaks ascribable to (100), (110), and (200) reflections, typical of the hexagonal P6mm (2D symmetry) pore structure.

The internal architecture of SBA-15 is clearly visible in the TEM image shown in Fig. 4.2, which confirms the highly ordered 2-D hexagonal regularity. The ordered arrays of silica channels have a diameter of ca. 6-7 nm with a wall thickness of about 3 nm.
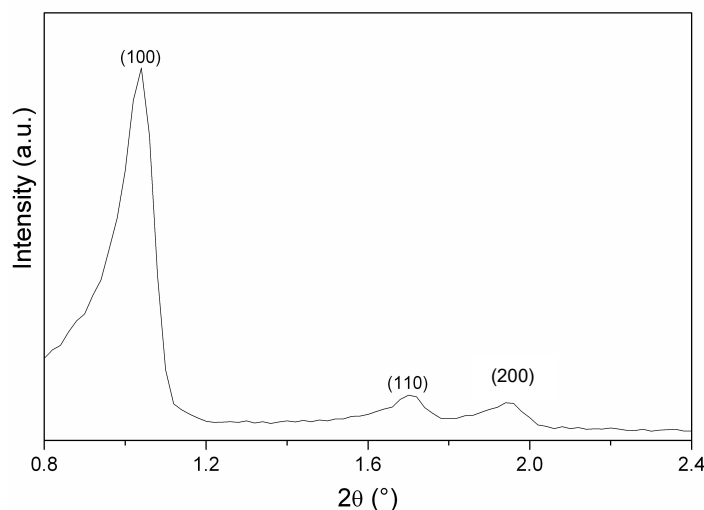


**Fig. 4.1.** Low angle X-ray diffraction pattern of SBA-15.
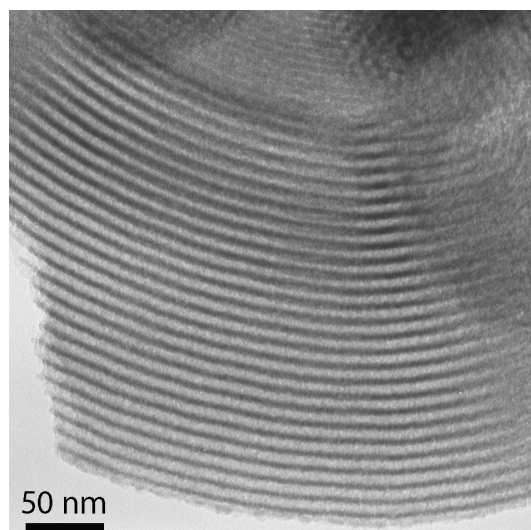
**Fig. 4.2.** TEM image of SBA-15.

Nitrogen physisorption curves are reported in Fig. 4.3, which shows a type IVa isotherm with a hysteresis loop at high relative pressures, typical of SBA-15 (Fig. 4.3A). BET surface area and pore volume were 803 m$^2$ g$^{-1}$ and 1.25 cm$^3$ g$^{-1}$, respectively. The BJH method was applied to the desorption branch of the isotherm to obtain the pore size distribution (Fig. 4.3B) which appears quite narrow and centred at 6.7 nm, in agreement with TEM results.
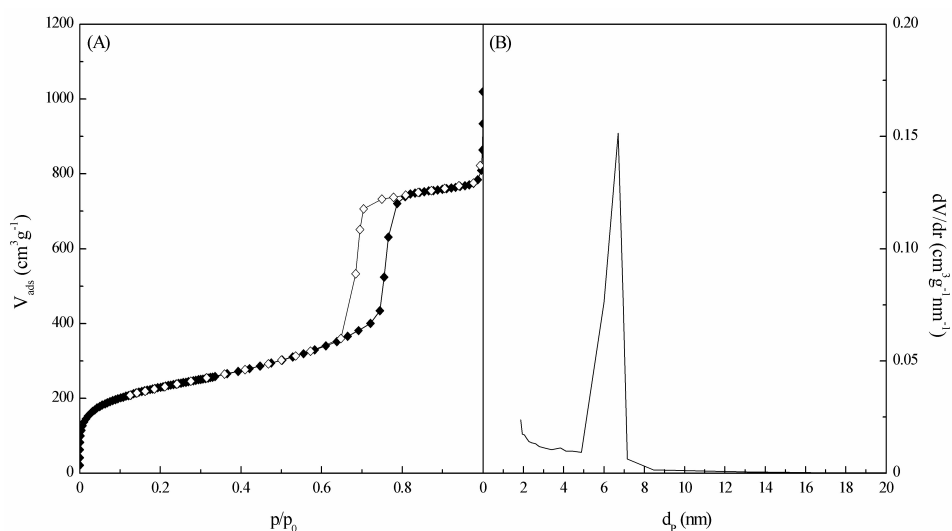


**Fig. 4.3.** Nitrogen adsorption-desorption isotherm (A) and pore size distribution (B) of SBA-15.

### 4.2.2. Characterisation of fresh catalysts

#### 4.2.2.1. Chemical composition, structural and textural characterisation

Tab. 4.1 reports the chemical composition as well as the structural and textural properties of the $x$NiCe_HT and $x$NiCe_HT$_{IWI}$ fresh catalysts, together with those of CeO$_2$_HT.

**Tab. 4.1.** Chemical composition, structural and textural properties of the fresh HT and HT$_{IWI}$ catalysts.

| Sample | Ni/Ce (mol mol⁻¹) | g$_{Ni}$/g$_{cat}$ (wt%) | Crystal phases | Cryst. size D$_c$ (nm) | S$_{BET}$ (m² g⁻¹) | V$_p$ (cm³ g⁻¹) |
|---|---|---|---|---|---|---|
| 0.15NiCe_HT | 0.13 | 4.3 | CeO₂ | n.p.ᵃ, 6 | 145 | 0.29 |
| 0.5NiCe_HT | 0.41 | 11.8 | NiO; CeO₂ | 9; 6 | 176 | 0.41 |
| 1.0NiCe_HT | 1.02 | 24.1 | NiO; CeO₂ | 16; 6 | 130 | 0.30 |
| CeO₂_HT | - | - | CeO₂ | 9 | 116 | 0.39 |
| 0.15NiCe_HT$_{IWI}$ | 0.14 | 4.6 | NiO; CeO₂ | n.d.ᵇ; 9 | 108 | 0.30 |
| 0.5NiCe_HT$_{IWI}$ | 0.49 | 13.9 | NiO; CeO₂ | 17; 9 | 88 | 0.23 |
| 1.0NiCe_HT$_{IWI}$ | 0.99 | 23.7 | NiO; CeO₂ | 23; 9 | 78 | 0.20 |

ᵃ n.p. (not present): no peaks typical of NiO phase were present; ᵇ n.d.: not determined.

The ICP-AES results show that the experimental Ni/Ce molar ratios are in good agreement with the theoretical ones, pointing out the efficiency of the preparation procedures.

The residual silica content on the NiCe_HT samples and CeO$_2$_HT (used as the support for the NiCe_HT$_{IWI}$ samples) is found to be about 2.5 wt% (Tab. 4.2), in agreement with the values reported by other authors for materials prepared through the HT method [26,27].

**Tab. 4.2.** Residual silica content on the $x$NiCe_HT and CeO$_2$_HT samples.

| Sample | Ni/Ce (mol mol⁻¹) |
|---|---|
| 0.15NiCe_HT | 2.12 |
| 0.5NiCe_HT | 2.25 |
| 1.0NiCe_HT | 2.51 |
| CeO₂_HT | 2.53 |

### *XRD and TEM*

In Fig. 4.4A, the low angle X-ray diffraction patterns of the $x$NiCe_HT catalysts are shown. Three signals, which can be indexed as the (100), (110), and (200) reflections characteristic of the 2-D hexagonal (*P6mm*) structure, are visible in the LA XRD pattern of 0.15NiCe_HT, indicating the presence of a long-range periodic order with hexagonal symmetry. However, the low intensity of the signals suggests that the material does not exactly replicate the original mesostructure of the SBA-15 template. Such intensity is even lower for the samples with higher nickel contents, which seems to indicate the formation of more disordered materials.

The wide angle (WA) XRD results for the $x$NiCe_HT catalysts are reported in Fig. 4.4B. All the diffraction patterns show peaks at 2θ values of 28.5°, 33.1°, 47.5°, 56.3°, and 59.1°, typical of the fluorite-type cubic crystal structure of $CeO_2$ (PDF card 81-0792). In the diffraction pattern of 1.0NiCe_HT, peaks ascribable to (111), (200), and (220) crystallographic planes of the NiO phase are visible at 37.3°, 43.3°, and 62.9° (PDF card 78-0643). In the case of 0.5NiCe_HT, only broad peaks of very low intensity are observed, reasonably due to the presence of small nickel oxide nanocrystals. The crystalline diffraction peaks of NiO are not observed in the diffractogram of 0.15NiCe_HT, probably due to the high dispersion of the nickel oxide phase and/or to detection limits of the technique.
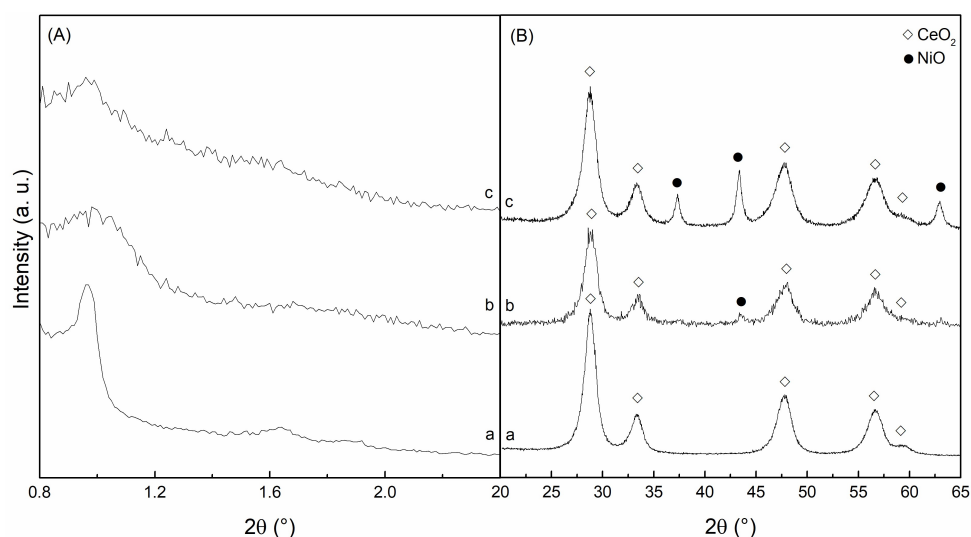


**Fig. 4.4.** Low angle (A) and wide angle (B) XRD patterns of the $x$NiCe_HT catalysts: 0.15NiCe_HT (a), 0.5NiCe_HT (b), and 1.0NiCe_HT (c).

The average crystallites size, $D_c$, for the $CeO_2$ phase is 6 nm, irrespective of the nickel content (Tab. 4.1). Instead, the mean size of NiO crystallites increases from 9 to 16 nm as the Ni/Ce molar ratio increases from 0.5 to 1.0 mol $mol^{-1}$.

Transmission electron microscopy (TEM) images reported in Fig. 4.5 confirm the LA and WA XRD data: all the samples preserve the ordered 2-D hexagonal symmetry of the parent SBA-15; however, with the increase in Ni content, the structure becomes more and more disordered. As expected for hard-templated materials deriving from SBA-15, beams of nanowires built-up of nanoparticles with mean diameter of 6-7 nm, and separated by 3-4 nm (Fig. 4.5A, inset), are observed for all the samples. In addition, small spheroidal NiO nanoparticles of 2-4 nm in size start to be visible for the 0.5NiCe_HT sample (Fig. 4.5B, inset). In the case of 1.0NiCe_HT, besides the small particles, thin rounded NiO nanocrystals of 20-50 nm in diameter are spread all over the mesostructured support (Fig. 4.5C). Such nanocrystals originate the spots in the electron diffraction image (Fig. 4.5C, inset).
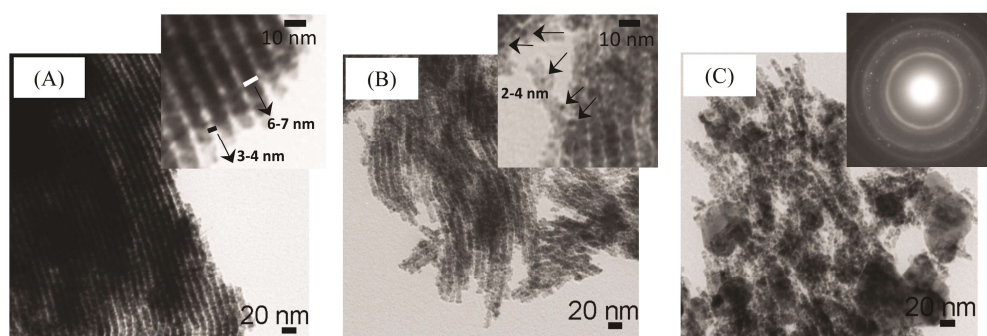


**Fig. 4.5.** TEM images of: (A) 0.15NiCe_HT; (B) 0.5NiCe_HT; (C) 1.0NiCe_HT.

LA XRD results for CeO₂_HT and 1.0NiCe_HT$_{IWI}$ are shown in Fig. 4.6A. The diffractogram of CeO₂_HT clearly shows the presence of the three reflections typical of the 2-D hexagonal structure, indicating that the reverse replica of the SBA-15 template has been, at least partially, formed. No significant differences are seen in the pattern of 1.0NiCe_HT$_{IWI}$, indicating that impregnation with Ni, even at the highest metal loading, does not modify the original structure of the ceria support. As expected, the WA XRD patterns of all the *x*NiCe_HT$_{IWI}$ samples (Fig. 4.6B) show diffraction peaks ascribable to the fluorite type cubic crystal structure of the pure cerium oxide. It is worthy of note that, at variance with the case of

the HT series, very small signals at 2θ values typical of the NiO phase can already be observed in the case of the 0.15NiCe_HT$_{IWI}$ catalyst, which seems to indicate a lower dispersion of the nickel oxide species deposited by impregnation. This assumption is supported by the results on 0.5NiCe_HT$_{IWI}$ and 1.0NiCe_HT$_{IWI}$, whose diffraction patterns show well-defined NiO peaks, from which a mean crystallite size of 17 and 23 nm has been calculated, respectively (Tab. 4.1). A D$_c$ value of 9 nm has been estimated for the pure CeO₂_HT support.
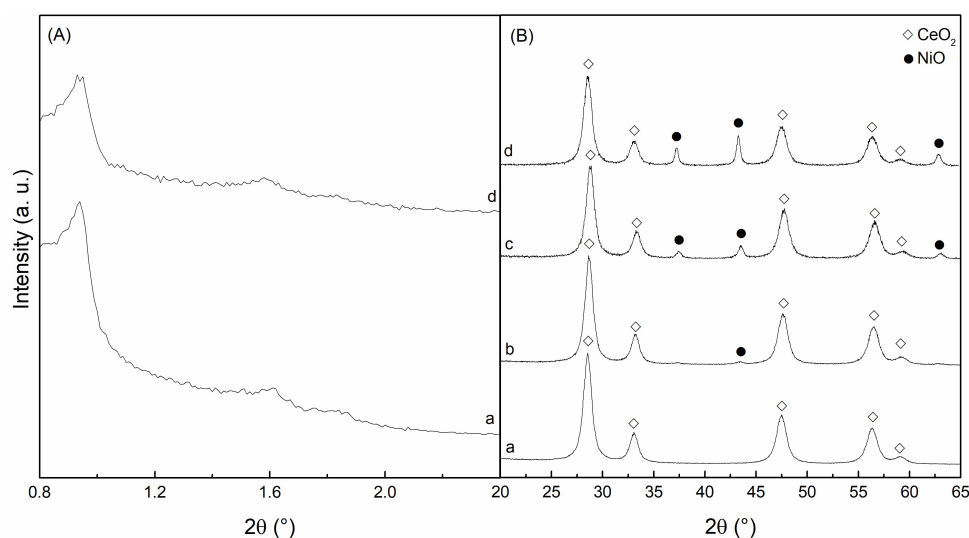


**Fig. 4.6.** Low angle (A) and wide angle (B) XRD patterns of the *x*NiCe_HT$_{IWI}$ catalyst: CeO₂_HT (a), 0.15NiCe_HT$_{IWI}$ (b), 0.5NiCe_HT$_{IWI}$ (c), 1.0NiCe_HT$_{IWI}$ (d).

TEM images of the CeO₂_HT (Fig. 4.7A) and 0.15NiCe_HT$_{IWI}$ (Fig. 4.7B) samples show features typical of a mesostructured material obtained by the hard template strategy using SBA-15 as a mould. No significant differences can be evidenced between these two samples. When the molar ratio Ni/Ce is increased up to 0.5 mol mol$^{-1}$, at the far end of the CeO₂ nanorods some porous nanoparticles start to form, preserving somehow the porosity of the mesostructured CeO₂ matrix (Fig. 4.7C). When the Ni/Ce molar ratio equals 1.0 mol mol$^{-1}$, the number of these porous nanoparticles increases, although the size seems to remain nearly the same, and the mesostructured CeO₂ is almost completed coated (Fig. 4.7D). By closely inspecting Figs. 4.7A-C, it can be seen that several channels are about 1-2 nm in diameter, i.e. not exactly void replicas of the former walls of the SBA-15 template. In addition, CeO₂ particles slightly larger (ca. 8 nm) than the pore size of the SBA-15 host (6-7 nm) are actually observed,

in agreement with XRD results. Such features, reasonably due to the growth of the $CeO_2$ particles induced by the calcination treatment after the removal of the SBA-15 template, were not observed in the case of the *x*NiCe_HT catalysts, thus suggesting an effect of the Ni-Ce interactions in preventing the $CeO_2$ nanocrystals growth.
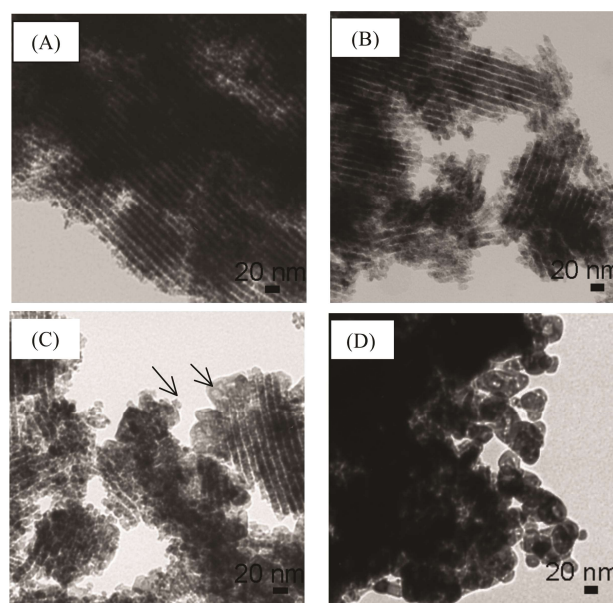


**Fig. 4.7.** TEM images of: (A) $CeO_2$_HT; (B) 0.15NiCe_HT$_{IWI}$; (C) 0.5NiCe_HT$_{IWI}$; (D) 1.0NiCe_HT$_{IWI}$.

*N₂ adsorption/desorption*

$N_2$ physisorption curves of all the prepared samples (Figs. 4.8, and 4.9,) have been classified according to [25]. The $N_2$ physisorption curves of the *x*NiCe_HT catalysts (Fig. 4.8) can be identified as type IIb isotherms, for which no plateau is observed at high p/p₀ values. In addition to a hysteresis loop typical of mesoporous solids prepared through the hard template method [28,29], a feature in the region of high relative pressures is observed for 0.5NiCe_HT and 1.0NiCe_HT, which can be ascribed to inter particles voids. Surface areas of the *x*NiCe_HT catalysts are in the range 130-176 m² g⁻¹ (Tab. 4.1), much higher than those reported in the literature (45-65 m² g⁻¹) for $Ni_xCe_yO$ mixed oxides prepared by conventional methods [30-32]. The pore size distribution (PSD) of the hard-templated catalysts (Fig. 4.8, insets) shows a peak at a pore size value (ca. 3.5 nm) comparable to the pore wall thickness of the parent SBA-15. However, unlike the case of the mesostructured silica (Fig. 4.3B), such peak appeared not

well-defined. This confirms the partial formation of the negative replica of the template, in agreement with LA XRD and TEM results.
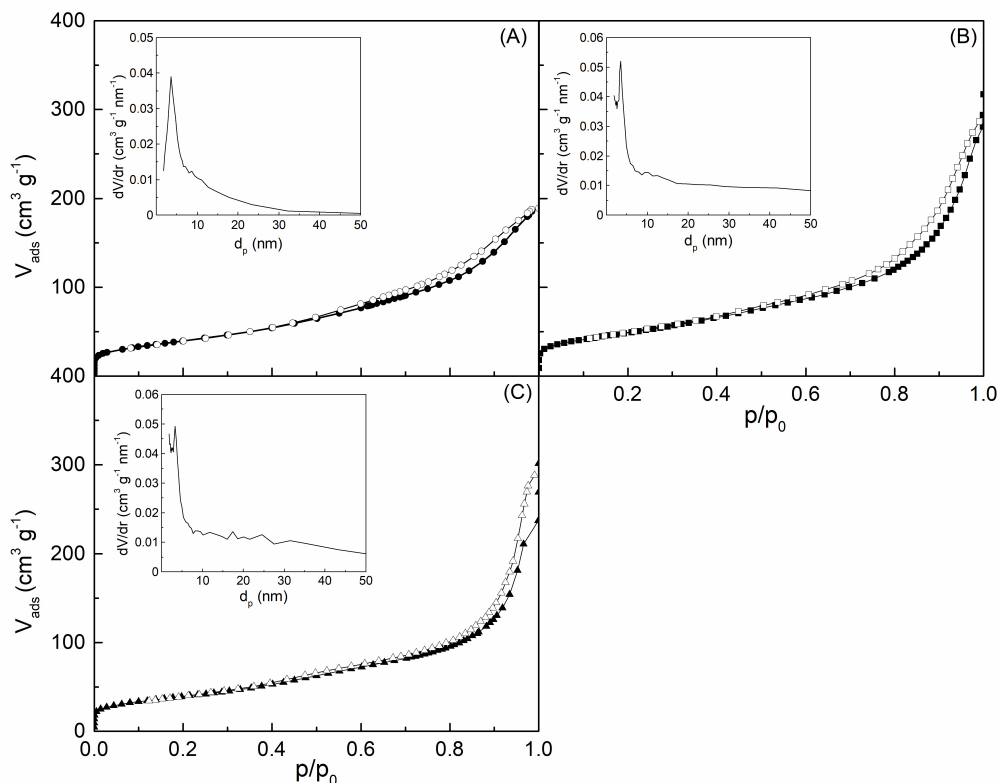


**Fig. 4.8.** $N_2$ adsorption/desorption isotherms and pore size distribution (inset) of the $x$NiCe_HT catalysts: (A) 0.15NiCe_HT; (B) 0.5NiCe_HT; (C) 1.0NiCe_HT.

CeO₂_HT and $x$NiCe_HT$_{IWI}$ samples also show type IIb $N_2$ adsorption/desorption isotherms (Fig. 4.9). Surface areas values of $x$NiCe_HT$_{IWI}$ catalysts decrease with the increase in the Ni loading (Tab. 4.1), varying from 108 $m^2$ $g^{-1}$ to 78 $m^2$ $g^{-1}$. Besides a first peak centered at around 3.2 nm (consistent with the formation of the negative replica of the SBA-15 template), a second broad peak centered at around 9 nm was observed in the PSD curve of the ceria support (Fig. 4.9A, inset), whose presence is indicative of larger pores with a wide size distribution. The presence of this broad peak is an indication that the structure of the obtained material is partially disordered, as already suggested by LA XRD and TEM analyses. As expected, such bimodal distribution of the pore size was also showed by the $x$NiCe_HT$_{IWI}$ catalysts (Fig. 4.9, insets).
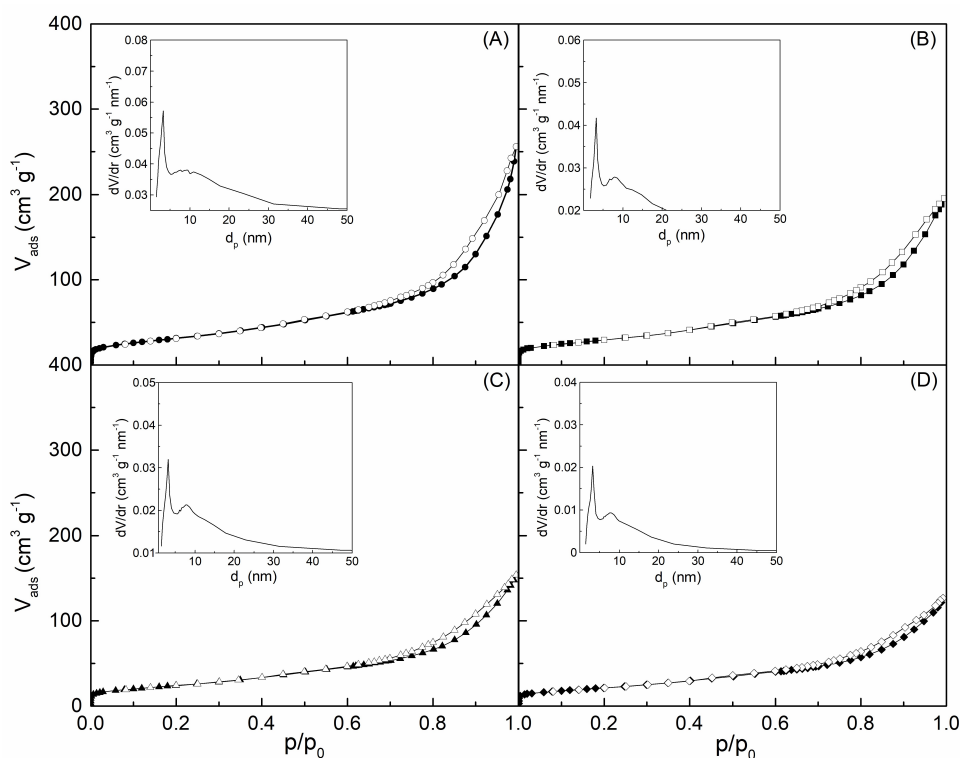
**Fig. 4.9.** $N_2$ adsorption/desorption isotherms and pore size distribution (inset) of the pure $CeO_2$_HT $x$NiCe_HT$_{IWI}$ catalysts: (A) $CeO_2$_HT; (B) 0.15NiCe_HT$_{IWI}$; (C) 0.5NiCe_HT$_{IWI}$; (D) 1.0NiCe_HT$_{IWI}$.

*Raman spectroscopy*

The interaction between NiO and $CeO_2$ in the mixed oxide materials prepared either by HT or HT$_{IWI}$ procedure was investigated by Raman spectroscopy (Fig 4.10).
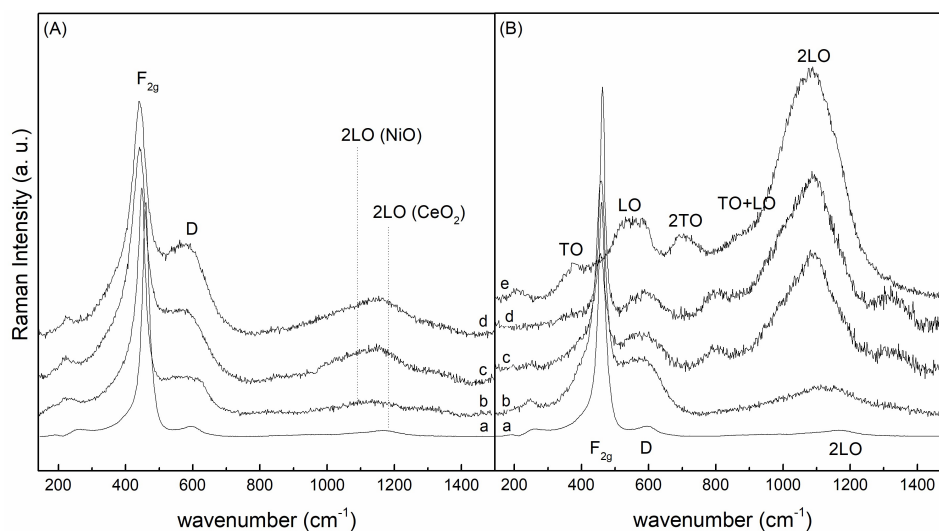


**Fig. 4.10.** Raman spectra of (A) $x$NiCe_HT and (B) $x$NiCe_HT$_{IWI}$: $CeO_2$_HT (a), 0.15NiCe (b), 0.5NiCe (c), 1.0NiCe (d), and NiO_HT refrence (e).

Raman spectra of the $x$NiCe_HT catalysts, and of the pure CeO₂_HT oxide, are compared in Fig. 4.10A in the spectral range 100-1500 cm$^{-1}$. The spectrum of CeO₂_HT (Fig. 4.10A, curve a) exhibits an intense peak at about 460 cm$^{-1}$, attributed to the $F_{2g}$ mode of the fluorite-like phase, and weak bands at about 265, 595, and 1175 cm$^{-1}$, due to second-order transverse acoustic (2 TA), defect-induced (D) mode, and second-order longitudinal optical (2LO) mode, respectively [33-35]. For the $x$NiCe_HT samples, the $F_{2g}$ band broadens and shifts to lower frequency with the increase in nickel content (Fig. 4.10A, curves b-d); in addition, it becomes asymmetric with a low-frequency tail, and new features appear at about 225 and 580 cm$^{-1}$, which can be related to lattice defects introduced into the CeO₂ structure in order to maintain charge neutrality after divalent cations incorporation [35,36]. The increase in intensity of the D band (580 cm$^{-1}$), which includes contributions due to oxygen vacancies (D₁, at about 530 cm$^{-1}$) and to cation substitution in the lattice (D₂, at about 590 cm$^{-1}$), with respect to that of the $F_{2g}$ mode, as well as the appearance of the band at about 225 cm$^{-1}$ at increasing Ni content, support the hypothesis of Ni$^{2+}$ incorporation within the CeO₂ structure and ensuing solid solution formation. The relative intensity of the D band to the $F_{2g}$ band (as well as the D₁/D₂ intensity ratio), although indicative of oxygen vacancies and solid solution formation [37], does not directly correlate with sample composition. The presence of NiO nanoparticles should be evidenced by bands at about 570 cm$^{-1}$ (one-phonon, LO mode), which would overlap with the D band of ceria, as well as by a band at ~1080 cm$^{-1}$ (two-phonon, 2LO mode) [38]. Such band, though not clearly distinguishable in the Raman spectra of Fig. 4.10A, is responsible of the change in shape and intensity of the band between 1000 and 1250 cm$^{-1}$, indicating the presence of NiO nanoparticles, in line with the WA XRD results.

The Raman spectra of the $x$NiCe_HT$_{IWI}$ samples are plotted in Fig. 4.10B together with that of the hard-templated CeO₂ support; the spectrum of an ad hoc prepared hard-templated NiO sample is also reported for comparison. The spectrum of NiO_HT (Fig. 4.10B, curve e) exhibits peaks at about 380, 560, 710, 890, and 1088 cm$^{-1}$ assigned to NiO one-phonon (1P) (TO and LO), two-phonon (2P) (2TO and TO + LO), and 2LO modes, respectively, in agreement with the predicted features for nanostructured NiO [38]. $x$NiCe_HT$_{IWI}$ samples are characterized by a peak at about 460 cm$^{-1}$ and a band at about 580 cm$^{-1}$, related to the $F_{2g}$ and D modes of CeO₂, respectively, as well as by features in the range 700-1100 cm$^{-1}$, typical of nanostructured NiO. Compared to the Raman spectra of the $x$NiCe_HT samples, a lower shift and broadening of the $F_{2g}$ and D modes of CeO₂ are observed at increasing Ni content, together

with a significant increase in intensity of the band at about 1090 cm$^{-1}$. These findings suggest that a lower amount of Ni ions is incorporated into the $CeO_2$ lattice, resulting in a less defective structure, and that an increasing amount of NiO is formed as a separate phase with the increase in Ni content, in agreement with WA XRD findings.

### 4.2.2.2. H₂-TPR

The reduction behaviour of all the prepared samples has been investigated. To better understand the effect of the NiO-support interactions on the reducibility of the nickel oxide species, the NiO_HT sample has also been analysed by TPR. The results for the hard-templated NiO and $CeO_2$ pure oxides are reported in Fig. 4.11.
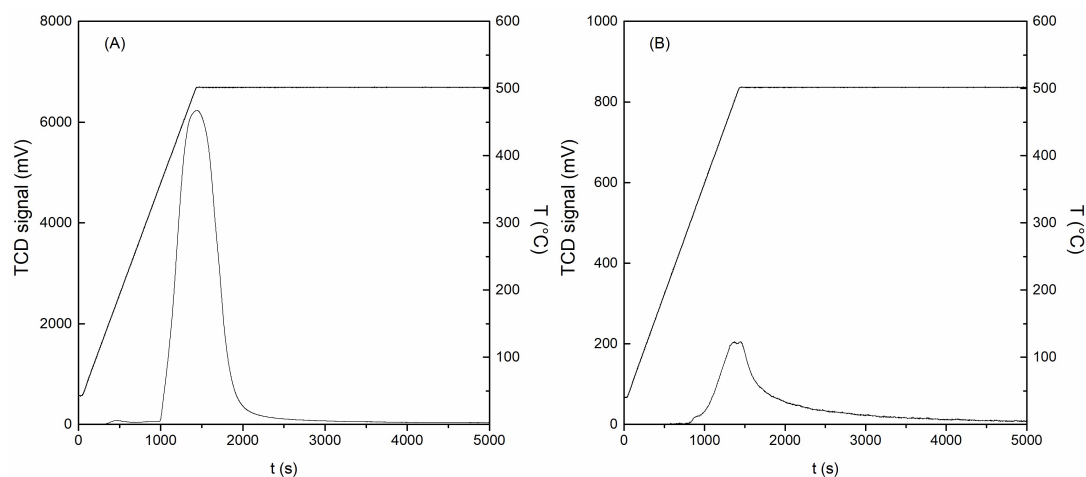


**Fig. 4.11.** H₂-TPR curves of pure (A) NiO_HT and (B) CeO₂_HT.

An intense peak centred at 500 °C was observed for NiO_HT (Fig. 4.11A), while a much less intense one was shown at the same temperature by $CeO_2$_HT (Fig. 4.11B), which is ascribable to the reduction of the surface capping oxygen of ceria and whose area is reported to increase with the rise in the surface area of the ceria sample [39,40].

TPR profiles of the *x*NiCe_HT catalysts are presented in Fig. 4.12A. Unlike the case of NiO_HT, all curves of the *x*NiCe_HT catalysts exhibit two main features, the former at temperatures between 160 and 380 °C and the latter at temperatures above 400 °C. In the TPR profile of 0.15NiCe_HT (Fig. 4.12A, profile a) such features appear as two distinct peaks, the first showing a shoulder facing on the low temperature and the second on the high temperature region. For 0.5NiCe_HT and 1.0NiCe_HT (Fig. 4.12A, profiles b and c) these two contributions merge and the low-temperature feature appears as a shoulder of an intense peak centered at 412

and 441 °C, respectively. By a closer inspection, the TPR signals of the $x$NiCe_HT catalysts appear to consist of several peaks, indicating the presence of different reducible species. In previous papers, the $H_2$-TPR profiles of $Ni_xCe_{1-x}O_2$ systems have been reported to show four reduction peaks ($\alpha$, $\beta$, $\gamma$, and $\delta$) [40-42]. The $\alpha$ peak, located at temperatures lower than 350 °C, has been ascribed to the reduction of oxygen species in oxygen vacancies generated by the $Ce_xNi_yO$ solid solution formation; such adsorbed species have also been reported to give rise to two different reduction peaks, $\alpha_1$ and $\alpha_2$, both located below 300 °C [31,43]. The $\beta$ and $\gamma$ peaks have instead been attributed to the reduction of nickel oxide particles dispersed on the ceria surface and to NiO species strongly interacting with $CeO_2$, respectively [40-42]. Finally, the high temperature $\delta$ peak, generally observed beyond 800 °C, has been ascribed to the reduction of bulk $CeO_2$ [31,40,41,43]. According to the literature, the low-temperature feature in the TPR profile of the $x$NiCe_HT samples can be reasonably ascribed to the abstraction by hydrogen of oxygen species adsorbed on defective sites in the solid solution and at the NiO/$CeO_2$ interface, whose presence is confirmed by Raman analysis. The high-temperature feature would instead originate from the superimposition of the $\beta$ and $\gamma$ peaks, resulting from the reduction of different NiO species, whose relative concentration depends on the nickel loading; however, a contribution stemming from ceria reduction could also be present since the surface reducibility of $CeO_2$ can be greatly increased by the establishing of strong Ni-Ce interactions [44].
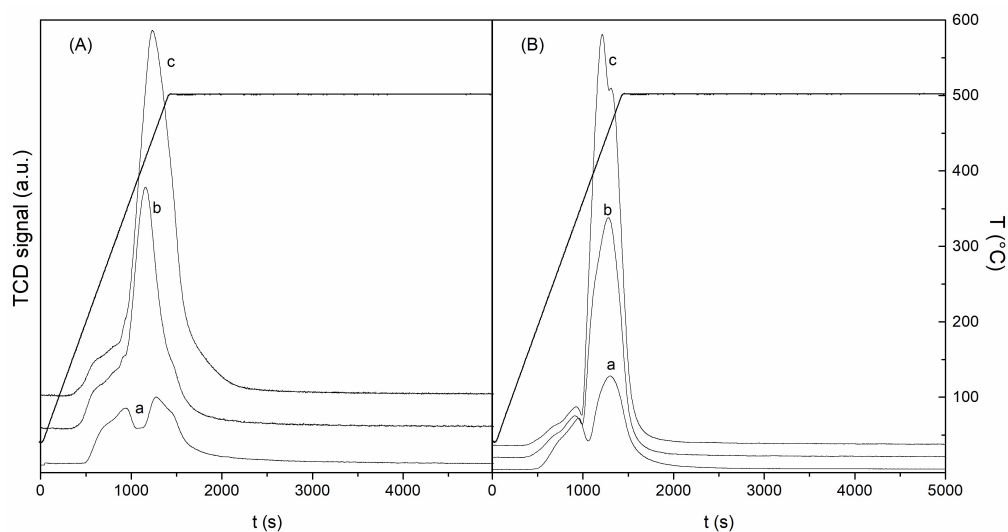


**Fig. 4.12.** $H_2$-TPR profiles of (A) $x$NiCe_HT and (B) $x$NiCe_HT$_{IWI}$: 0.15NiCe (a), 0.5NiCe (b), 1.0NiCe (c).

The reduction profiles of the $x$NiCe_HT$_{IWI}$ catalysts are reported in Fig. 4.12B. A low-temperature feature, indicative of the existence of defective sites, is observed below 350 °C, together with a peak of higher intensity centered at temperatures above 420 °C, mainly ascribable to the contribution of the β-type NiO species, in agreement with Raman results.

## 4.2.3. Structural characterisation after H₂ pretreatment at 400 °C for 1 h

WA XRD results of the $x$NiCe_HT catalysts submitted to the H₂ pretreatment at 400 °C are shown in Fig. 4.13A. Only reflections ascribable to the $CeO_2$ phase are observable in the XRD patterns of reduced 0.15NiCe_HT and 0.5NiCe_HT, which seems to indicate that highly dispersed $Ni^0$ species are formed after the reduction pretreatment at mild conditions. However, the presence of unreduced nickel species cannot be excluded, since the $Ni^{2+}$ species involved in the formation of the Ni-Ce solid solution can be expected to be hardly reducible through the H₂-treatment at 400 °C, as suggested in [45]. For the 1.0NiCe_HT catalyst, besides those of the $CeO_2$ phase, peaks at 2θ values of 44.5 ° and 51.9 ° are observable, which can be ascribed to the presence of $Ni^0$ crystallites (PDF card 04-0850). Small signals ascribable to NiO are also visible at 2θ values of 37.3 ° and 43.3 °. The existence of nickel in the oxidized state has been observed by in-situ XPS on Ni/CeO₂ [46] and Ni/CeO₂-ZrO₂ [47] catalysts, previously reduced at 380 and 450 °C, respectively, and then transferred to the analysis chamber without being exposed to the environment. Accordingly, the reflections appearing at 37.3 ° and 43.3 ° in the XRD pattern of the reduced 1.0NiCe_HT sample can be ascribed to the presence of un-reduced nickel oxide species, though a minor contribution of nickel oxide deriving from reoxidation of the catalyst surface due to exposure to air prior to the XRD measurements cannot be excluded. A mean size value of 16 nm is calculated for $Ni^0$ crystallites on 1.0NiCe_HT, comparable with that obtained for NiO nanocrystals on the fresh sample. This is in line with Raman results, which evidenced the formation, regardless of the Ni loading, of dispersed nickel oxide species in strong interaction with the ceria support. It may be supposed that such strong interactions hinder the sintering of $Ni^0$ particles deriving from NiO reduction.
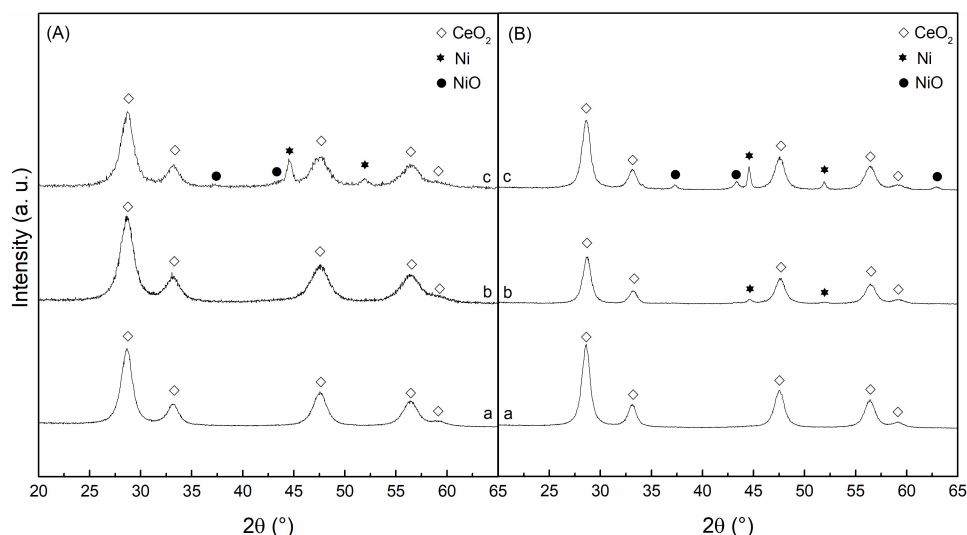
**Fig. 4.13.** Wide angle X-ray diffraction patterns of (A) $x$NiCe_HT and (B) $x$NiCe_HT$_{IWI}$ after pretreatment at 400 °C for 1 h: 0.15NiCe (a), 0.5NiCe (b), and 1.0NiCe (c).

Fig. 4.13B shows the WA XRD patterns of the reduced $x$NiCe_HT$_{IWI}$ catalysts. Reflections of the CeO₂ phase appear in the diffractogram of all the samples. In the case of 0.15NiCe_HT$_{IWI}$, no peaks ascribable to any nickel species are detected. Though the presence of metallic nickel is expected, the lack of Ni$^0$ reflections is most probably due to the low concentration and/or high dispersion of the metal. Signals typical of the Ni$^0$ phase are visible for the other $x$NiCe_HT$_{IWI}$ catalysts. Ni$^0$ crystallite size values of 19 and 34 nm have been calculated for 0.5NiCe_HT$_{IWI}$ and 1.0NiCe_HT$_{IWI}$, respectively. For the latter sample, peaks at 37.3 °, 43.3 °, and 62.9 ° in its XRD pattern reveal the presence of residual NiO, for which a mean crystallite size of 18 nm has been estimated. Unlike 0.5NiCe_HT$_{IWI}$, a marked increase in the size of the Ni$^0$ nanocrystals in comparison with the NiO crystallite size of the fresh catalyst is observed for 1.0NiCe_HT$_{IWI}$ (cf. Tab. 4.1), suggesting that deposition of NiO by the IWI procedure results in a weaker interaction between the nickel oxide phase and ceria. This is confirmed by Raman analysis, which showed that, on fresh 0.5NiCe_HT$_{IWI}$ and 1.0NiCe_HT$_{IWI}$, a significant amount of NiO is present as a separate phase (whose amount seems to increase along with the Ni content). TEM analysis of 1.0NiCe_HT$_{IWI}$ (Fig. 4.14) is in agreement with XRD results: together with small nanocrystals dispersed within/over the mesostructured CeO₂ (indicated by arrows), probably associable to the residual NiO phase, thin Ni$^0$ particles with diameter even higher than 50 nm are present.
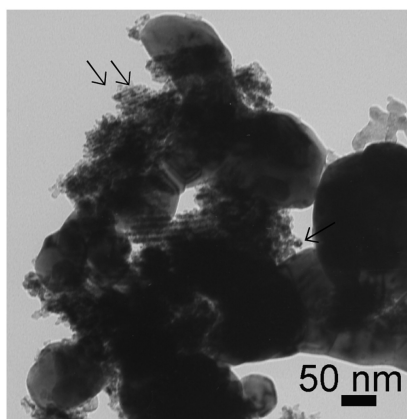
**Fig. 4.14.** TEM image of 1.0NiCe_HT$_{IWI}$ after H$_2$ pretreatment at 400 °C for 1 h.

## 4.2.4. Catalytic results

### 4.2.4.1. *x*NiCe_HT and *x*NiCe_HT$_{IWI}$

In Tab. 4.3, are summarised the catalytic results for the *x*NiCe_HT and *x*NiCe_HT$_{IWI}$ samples. The reaction tests were performed at 300 °C and atmospheric pressure by using 0.050 g of catalyst and a H$_2$/CO$_2$ molar ratio equal to 4.3 mol mol$^{-1}$ (space velocity, SV = 72000 cm$^3$ h$^{-1}$ g$_{cat}$$^{-1}$).

**Tab. 4.3.** Catalytic results for *x*NiCe_HT, *x*NiCe_HT$_{IWI}$, and *x*NiAl_IWI. Reaction condition; T = 300 °C; P = 1 atm; m$_{cat}$ = 0.050 g; SV = 72000 cm$^3$ h$^{-1}$ g$_{cat}$$^{-1}$; H$_2$/CO$_2$ = 4.3 mol mol$^{-1}$.

| Sample | CO$_2$ conversion (mol%) | CH$_4$ selectivity (mol%) |
|---|---|---|
| 0.15NiCe_HT | 37 | 93 |
| 0.5NiCe_HT | 70 | > 99 |
| 1.0NiCe_HT | 76 | > 99 |
| 0.15NiCe_HT$_{IWI}$ | 48 | 97 |
| 0.5NiCe_HT$_{IWI}$ | 66 | 98 |
| 1.0NiCe_HT$_{IWI}$ | 57 | 98 |

Unlike CeO$_2$_HT, which, as expected, was inactive towards CO$_2$ methanation, $x$NiCe_HT and $x$NiCe_HT$_{IWI}$ catalysts are very active, with CO$_2$ conversions ranging from 37 to 76 mol%. All catalysts were found to be stable within 6 h on stream and showed high CH$_4$ selectivity ($\geq$ 93 mol%). To confirm the catalysts stability, long-run tests (up to 30 h on stream) were carried out on the 0.5NiCe_HT and 0.5NiCe_HT$_{IWI}$ samples, which did not show any decrease in CO$_2$ conversion. For the $x$NiCe_HT samples, catalytic activity increases along with the Ni content (Tab. 4.3). The highest conversion value (76 mol %) is shown by 1.0NiCe_HT, on which Ni$^0$ particles of 16 nm in size are present, despite the high Ni content. A comparison of the present catalytic results, in terms of specific activity, with those reported in [44] for ceria/zirconia-supported Ni (Ni-CZ) catalysts with similar nickel contents points out a superior catalytic activity of the HT samples. Indeed, specific activity values of 2.43 x 10$^{20}$ and 1.53 x 10$^{20}$ molecules$_{CO2,transformed}$ g$_{Ni}^{-1}$ s$^{-1}$ are calculated at 300 °C for 0.15NiCe_HT and 0.5NiCe_HT, respectively, i.e. higher than those (2.07 x 10$^{20}$ and 0.80 x 10$^{20}$ molecules$_{CO2,transformed}$ g$_{Ni}^{-1}$ s$^{-1}$, respectively) obtained at 350 °C for 0.15Ni-CZ and 0.5Ni-CZ. In the case of the $x$NiCe_HT$_{IWI}$ catalysts, the highest CO$_2$ conversion value (66 mol%) was observed for 0.5NiCe_HT$_{IWI}$ (Tab. 4.3), the lower CO$_2$ conversion for 1.0NiCe_HT$_{IWI}$ being not surprising in view of the much larger size of its Ni$^0$ nanocrystals (34 nm) compared to that of 0.5NiCe_HT$_{IWI}$ (19 nm).

### 4.2.4.2. The role of Ni$^0$ and CeO$_2$

On Ni-based catalysts supported on ceria-zirconia, CO$_2$ methanation has been reported to occur without involving CO as the reaction intermediate [24,47,48]. In the proposed mechanism, CO$_2$ would be activated on the ceria-zirconia support by forming carbonates and hydrogen carbonates, which would be subsequently hydrogenated to formates and finally to methane by hydrogen dissociatively adsorbed on Ni$^0$ particles.

To investigate the role of CeO$_2$ and Ni$^0$ nanocrystals in adsorbing and activating CO$_2$, temperature programmed desorption (TPD) runs were performed (cf. par. 2.2.9) on CeO$_2$_HT and NiO_HT pure oxides as well as on 0.5NiCe_HT and 0.5NiCe_HT$_{IWI}$ previously submitted to the reduction pretreatment. The pertinent results are shown in Fig. 4.15.
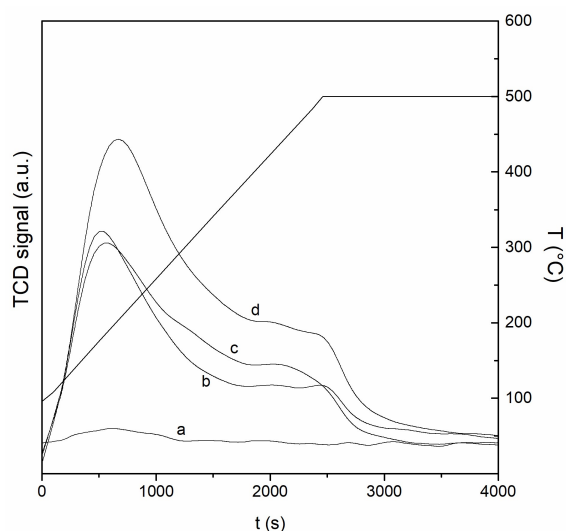
**Fig. 4.15.** $CO_2$-TPD profiles of NiO_HT (a), CeO_2_HT (b), 0.5NiCe_HT$_{IWI}$ (c), and 0.5NiCe_HT (d) after $H_2$ pretreatment at 400 °C for 1 h.

In the case of CeO_2_HT, 0.5NiCe_HT$_{IWI}$, and 0.5NiCe_HT, increasing amounts of $CO_2$ (corresponding to $6.8 \times 10^{-2}$, $7.3 \times 10^{-2}$, and $11.0 \times 10^{-2}$ mmol$_{CO2}$ g$_{cat}^{-1}$, respectively) are observed to desorb between 100 and 500 °C. Two main features, the first centered in the temperature range 175-205 °C and the second above 450 °C, can be seen in the TPD profiles of these samples. Such features do not appear neatly separate, which seems to indicate the presence of heterogeneous adsorbing sites. Several papers can be found in the literature dealing with the study of $CO_2$-$CeO_2$ interactions by means of TPD [49-52], where the nature and stability of the adsorbed species are assigned by comparison with Fourier Transform Infrared Spectroscopy (FTIR) results [49-51]. Hydrogen carbonates as well as carbonates (bridged, mono-, bi-, and polydentate) were identified by FTIR after $CO_2$ adsorption on ceria, whose stability increases in the order hydrogen carbonates < bridged and bidentate carbonates < mono- and polydentate carbonates. Such species were assumed to be responsible for peaks in $CO_2$-TPD curves at temperatures < 200 °C, in the range 200-450 °C, and > 450 °C, respectively [51]. Thus, the TPD profiles of CeO_2_HT, 0.5NiCe_HT, and 0.5NiCe_HT$_{IWI}$ may be described accordingly. It is worthy of note that, at variance with the previous samples, only a low amount of $CO_2$ ($0.25 \times 10^{-2}$ mmol$_{CO2}$ g$_{cat}^{-1}$) desorbs between 100 and 300 °C in the case of NiO_HT, indicating the establishing of very weak interactions between nickel species and $CO_2$. The present $CO_2$-TPD results support the assumption of different activation sites for $CO_2$ and $H_2$ during methanation, suggesting the occurrence of a reaction mechanism similar to that proposed

in the literature for ceria/zirconia-supported Ni catalysts [24,47,48]. Such a mechanism should be favoured by a large metal-support interface, where $Ni^0$ particles and ceria are in close interaction. Hence, the catalytic activity of the $x$NiCe_HT samples can be explained accordingly, since the presence of well dispersed NiO species strongly interacting with the ceria support (which are then preserved from severe sintering phenomena during reduction) has been evidenced by Raman results. However, a CO selectivity of 7 mol% was observed for 0.15NiCe_HT. According to [24], a parallel reaction pathway, which involves CO formation through a redox cycle on reduced ceria, could also take place. The higher value of CO selectivity showed by the 0.15NiCe_HT sample might thus be explained by considering that, on this catalyst, a significant part of nickel is involved in the Ni-Ce solid solution formation, hence favouring the surface $CeO_2$ reduction, but is prevented to form $Ni^0$ nanocrystals, i.e. the active sites for $H_2$ activation. Interestingly, by comparing the two 0.15NiCe catalysts, besides a higher CO selectivity, 0.15NiCe_HT also shows a lower $CO_2$ conversion in comparison with 0.15NiCe_HT$_{IWI}$ (Tab. 4.3). By taking into account Raman results, which pointed out that a lower amount of Ni ions is incorporated into the $CeO_2$ structure in the case of the IWI samples, it can be reasonably proposed that on 0.15NiCe_HT$_{IWI}$ a higher amount of NiO can be transformed to $Ni^0$ by the reduction pretreatment at 400 °C, providing a higher concentration of active sites on which $H_2$ is made available for both CO and $CO_2$ hydrogenation and limiting the decrease in activity due to the competition between $H_2$ and CO for the $Ni^0$ sites.

### 4.2.4.3. Influence of space velocity

Unlike the 0.15NiCe and 1.0NiCe samples, 0.5NiCe_HT and 0.5NiCe_HT$_{IWI}$ catalysts show similar $CO_2$ conversion values at SV = 72000 cm$^3$ h$^{-1}$ g$_{cat}^{-1}$, despite the large difference in $Ni^0$ nanocrystal size (cf. par. 4.2.3.1). For this reason, the catalytic performance of such samples was further investigated at a much higher space velocity (696000 cm$^3$ h$^{-1}$ g$_{cat}^{-1}$), by using 0.0125 g of catalyst. $CO_2$ conversion values of 25 and 19 mol% were obtained for 0.5NiCe_HT and 0.5NiCe_HT$_{IWI}$, respectively. Interestingly, besides conversion, CH$_4$ selectivity was also found to decrease for 0.5NiCe_HT$_{IWI}$ together with an appreciable increase in the formed amount of CO (11 mol%). According to [53], the presence of extended Ni faces on the large $Ni^0$ particles would favour the occurrence of the reverse water gas shift reaction; hence, the rise in CO selectivity for 0.5NiCe_HT$_{IWI}$ might be explained accordingly. To inspect the catalytic

behaviour of the 0.5NiCe catalysts in more detail, the metal surface area was determined by $H_2$ pulse chemisorption on the samples previously submitted to the $H_2$ reduction pretreatment at 400 °C. Specific metal surface areas ($A_{met}$) of 5.0 and 4.5 $m_{(Ni^0)}^2$ $g_{cat}^{-1}$ (corresponding to Ni dispersion values of 6.3 and 4.9%) were calculated for 0.5NiCe_HT and 0.5NiCe_HT$_{IWI}$, respectively. The values of specific activity calculated on the metal surface basis are 3.6 x $10^{18}$ and 3.7 x $10^{18}$ (molecules$_{CO_2;transformed}$ $m_{(Ni^0)}^{-2}$ $s^{-1}$) at SV = 72000 $cm^3$ $h^{-1}$ $g_{cat}^{-1}$, and 11.7 x $10^{18}$ and 9.8 x $10^{18}$ (molecules$_{CO_2;transformed}$ $m_{(Ni^0)}^{-2}$ $s^{-1}$) at SV = 696000 $cm^3$ $h^{-1}$ $g_{cat}^{-1}$, for 0.5NiCe_HT and 0.5NiCe_HT$_{IWI}$, respectively. Though the results confirm a similar catalytic performance at the lower space velocity, a higher activity is observed on the 0.5NiCe_HT sample at increasing SV values, suggesting that the presence of small $Ni^0$ crystallites is crucial to preserve high catalytic performance also under unfavourable reaction condition.

### 4.2.5. Conclusions

*x*NiCe_HT and *x*NiCe_HT$_{IWI}$ catalysts were found very active and selective for the $CO_2$ methanation reaction after a mild reduction pretreatment ($H_2$ at 400 °C for 1 h). The observed catalytic behaviour can be explained by taking into account the role of ceria in allowing the formation of small NiO nanocrystals in strong interaction with the support, which, however, can be reduced (at least partially) under mild conditions. Such metal oxide-support interactions are particularly efficient in the case of the *x*NiCe_HT systems, where they prevent the occurrence of severe sintering processes of the $Ni^0$ active phase deriving from the $H_2$ reduction pretreatment, regardless of the nickel content. By converse, in the case of the *x*NiCe_HT$_{IWI}$ catalysts, a remarkable increase in the particle size of $Ni^0$ compared with that of the parent NiO nanocrystals is observed for 1.0NiCe_HT$_{IWI}$, leading to a decrease in $CO_2$ conversion in spite of the increase in nickel loading. These findings indicate that the HT method permits to achieve a good dispersion of higher nickel amounts in comparison with the conventional impregnation procedure. Interestingly, the similar values of $CO_2$ conversion for the 0.5NiCe_HT and 0.5NiCe_HT$_{IWI}$ samples, despite the considerably different $Ni^0$ crystal size, would suggest that this parameter does not crucially affect the catalytic performance. However, the comparison of the $CO_2$ conversion values for the two previous catalysts at higher space velocity seems to indicate that the validity of this assumption is limited to a restricted range of operating

conditions, the size of the $Ni^0$ nanocrystals being very important for maintaining high catalytic activity and $CH_4$ selectivity in a wide range of reaction conditions.

## 4.3. *Soft-Templated xNiO/CeO₂*

### 4.3.1. Characterisation of fresh catalysts

#### 4.3.1.1. Chemical composition, structural and textural characterisation

In Tab 4.4, chemical composition, structural and textural properties of the $x$NiCe_ST and $x$NiCe_ST$_{IWI}$ catalysts are reported, as well as those of NiO_ST and CeO₂_ST pure oxides. ICP-AES results show that the experimental values of the Ni/Ce molar ratio are very close to the nominal ones for all the catalysts.

**Tab. 4.4.** Chemical composition, structural properties, and textural features of the prepared samples.

| Sample | Ni/Ce (mol mol$^{-1}$) | g$_{Ni}$/g$_{cat}$ (wt%) | Crystal phases | Cryst. size D$_c$ (nm) | S$_{BET}$ (m$^2$ g$^{-1}$) | V$_p$ (cm$^3$ g$^{-1}$) |
|---|---|---|---|---|---|---|
| NiO_ST | - | - | NiO | 3 | 209 | 0.31 |
| CeO₂_ST | - | - | CeO₂ | 5 | 191 | 0.36 |
| 0.3NiCe_ST | 0.29 | 8.7 | NiO; CeO₂ | 4; 3 | 174 | 0.17 |
| 0.5NiCe_ST | 0.48 | 13.5 | NiO; CeO₂ | 4; 3 | 178 | 0.24 |
| 1.0NiCe_ST | 0.96 | 23.0 | NiO; CeO₂ | 4; 3 | 206 | 0.29 |
| 1.5NiCe_ST | 1.43 | 30.1 | NiO; CeO₂ | 4; 3 | 221 | 0.38 |
| 2.5NiCe_ST | 2.50 | 40.9 | NiO; CeO₂ | 4; 3 | 208 | 0.37 |
| 4.0NiCe_ST | 3.84 | 49.1 | NiO; CeO₂ | 4; 3 | 209 | 0.38 |
| 0.3NiCe_ST$_{IWI}$ | 0.32 | 9.7 | NiO; CeO₂ | 11; 5 | 155 | 0.27 |
| 0.5NiCe_ST$_{IWI}$ | 0.53 | 14.7 | NiO; CeO₂ | 14; 4 | 162 | 0.28 |
| 1.0NiCe_ST$_{IWI}$ | 1.02 | 24.1 | NiO; CeO₂ | 20; 5 | 122 | 0.23 |
| 1.5NiCe_ST$_{IWI}$ | 1.58 | 31.9 | NiO; CeO₂ | 21; 5 | 107 | 0.22 |

## *XRD and TEM*

The XRD patterns of the *x*NiCe_ST mixed oxides, as well as those of pure CeO$_2$_ST and NiO_ST, are reported in Fig. 4.16.
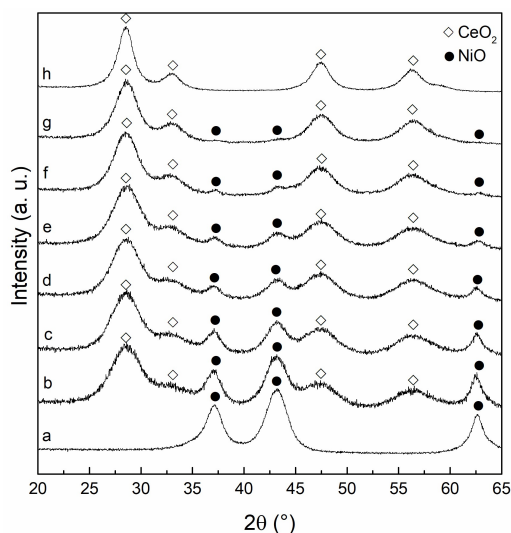


**Fig. 4.16.** Wide angle X-ray diffraction of NiO_ST (a), 4.0NiCe_ST (b), 2.5NiCe_ST (c), 1.5NiCe_ST (d), 1.0NiCe_ST (e), 0.5NiCe_ST (f), 0.3NiCe_ST (g), and CeO$_2$_ST (h).

CeO$_2$_ST (Fig. 4.16, pattern h) shows the typical reflections of the fluorite-type cubic crystalline structure, with an average nanocrystal diameter of 4.5 nm. In the diffractogram of NiO_ST (Fig. 4.16, pattern a), peaks ascribable to the crystallographic planes of the NiO phase are visible, from which a mean crystallite size of about 4 nm has been estimated.

In the case of the *x*NiCe_ST mixed oxides, the distinctive peaks of the CeO$_2$ phase appear enlarged in comparison with those of the pure oxide, in agreement with a calculated value of ca. 3 nm for the mean nanocrystal diameter. Signals ascribable to the presence of NiO are observed for all the samples, which become more and more defined with the increase in Ni content. However, an average nanocrystal size of about 4 nm has been calculated irrespective to the Ni content, which is very similar to that obtained for pure NiO_ST (Tab. 4.4). If compared to those obtained for the HT samples (Tab. 4.1), the lower crystallite size values of CeO$_2$ and NiO shown by CeO$_2$_ST and *x*NiCe_ST clearly indicate the higher efficiency of the soft-template method in hindering the growth of the oxides particles during the synthesis. Such

an efficiency is particularly interesting for ensuring a very high dispersion of NiO also for the samples with the higher Ni/Ce molar ratio.

TEM images of pure $CeO_2$_ST (Fig. 4.17A) point out the presence of thin nanofilaments (3-4 nm in diameter and up to 200 nm long, indicated by arrows) that coexist with small, roughly spheroidal, nanoparticles of 3-5 nm in size (Fig. 4.17A, inset), while only small nanorods (3-4 nm in diameter and 15–20 nm long) are visible in the case of NiO_ST (Fig. 4.17B). In the case of the 0.5NiCe_ST (Fig. 4.17C), a low number of nanofilaments, as those observed for pure $CeO_2$_ST, appears to be dispersed into/over a matrix made up of small spheroidal nanoparticles. When the Ni/Ce molar ratio rises up to 2.5 (2.5NiCe_ST sample, Fig. 4.17D) the number of elongated nanoparticles (indicated by arrows) increases compared to that in the 0.5NiCe_ST sample. Such nanoparticles show a morphology which seems to resemble to that of the NiO_ST nanorods, although their length reaches 70-80 nm. The comparison of the particle size estimated by TEM with the crystal size obtained by XRD suggests that both the nanofilaments and the nanorods could consist of chains of small spheroidal nanocrystals probably due to a self-organization mechanism induced by the presence of the ionic surfactant (CTAB).
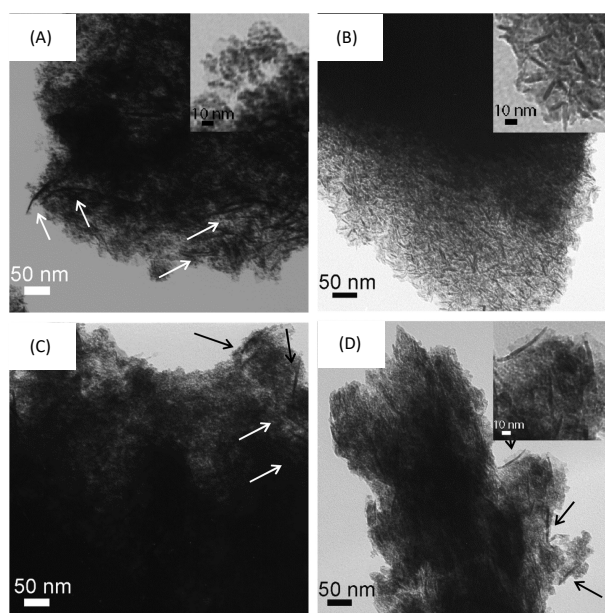


**Fig. 4.17.** TEM images of selected *x*NiCe_ST catalysts: (A), $CeO_2$_ST; (B), NiO_ST; (C), 0.5NiCe_ST; (D) 2.5NiCe_ST.

Fig. 4.18 shows the XRD patterns of the $x$NiCe_ST$_{IWI}$ catalysts as well as that of the CeO$_2$_ST support. Together with the diffraction peaks ascribable to the fluorite-type cubic crystal structure of CeO$_2$, signals at 2θ values typical of the NiO phase are observable for all the $x$NiCe_ST$_{IWI}$ samples. Besides increasing in intensity, such signals become narrower along with the nickel content, indicating the formation of larger NiO nanocrystals, whose size ranges between 11 and 21 nm (Tab. 4.4).
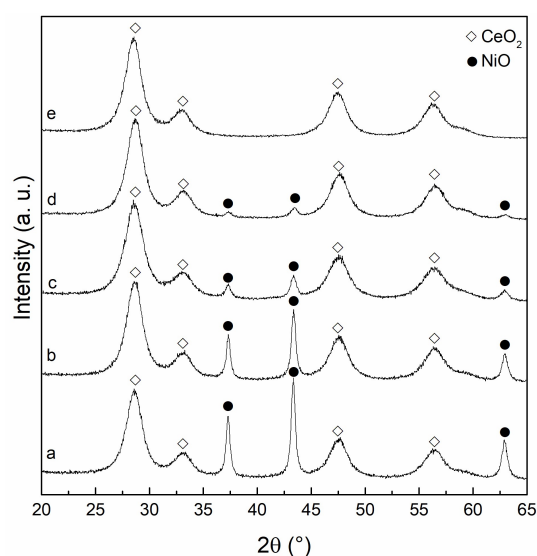


**Fig. 4.18.** Wide angle X-ray diffraction of 1.5NiCe_ST$_{IWI}$ (a), 1.0NiCe_ST$_{IWI}$ (b), 0.5NiCe_ST$_{IWI}$ (c), 0.3NiCe_ST$_{IWI}$ (d), and CeO$_2$_ST (e).

In agreement with what reported for the HT and HT$_{IWI}$ systems, this finding seems to further confirm that deposition of the nickel oxide precursor on the previously prepared CeO$_2$ support by the IWI method leads to a much less dispersion of the supported phase with respect to the ST method. TEM results also support this view (Fig. 4.19); indeed, nanoparticles with a broad particle size distribution (from 15 to 40 nm), dispersed into/over the CeO$_2$ matrix, are present in TEM images of both 1.0NiCe_ST$_{IWI}$ and 1.5NiCe_ST$_{IWI}$ samples (Fig. 4.19A and B, respectively). Interestingly, no nanofilaments associable with the CeO$_2$ support are clearly detectable; moreover, the great majority of the observed particles, probably ascribable to NiO

phase, appear to be mesoporous, hence a direct comparison with the crystal size obtained by XRD could be meaningless.
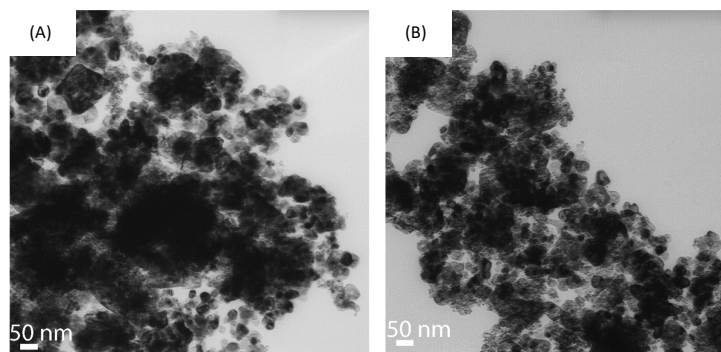


**Fig. 4.19.** TEM images of selected $x$NiCe_ST$_{IWI}$ catalysts: (A) 1.0NiCe_ST$_{IWI}$; (B) 1.5NiCe_ST$_{IWI}$.

### *N₂ adsorption/desorption*

N$_2$ physisorption results of CeO$_2$_ST and NiO_ST pure oxides, as well as for $x$NiCe_ST and $x$NiCe_ST$_{IWI}$ catalysts were reported in Fig. 4.20, 4.21, and 4.22, respectively. All physisorption curves can be classified as type IVa adsorption/desorption isotherms, which are typical of mesoporous solids.
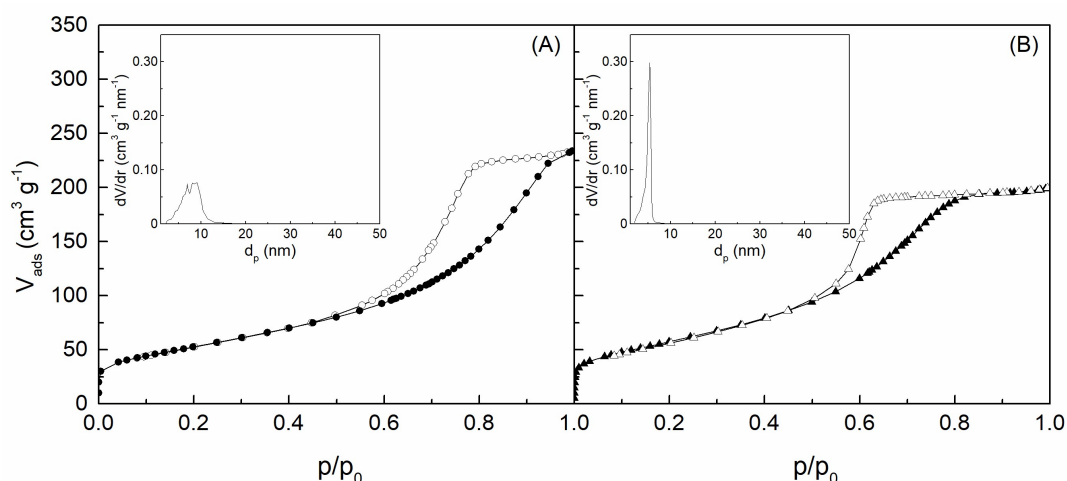


**Fig. 4.20.** N$_2$ adsorption/desorption isotherms and pore size distribution (inset) of (A) CeO$_2$_ST and (B) NiO_ST pure oxides.

Both $CeO_2$_ST and NiO_ST pure oxides exhibit a quite narrow pore size distribution curves (Fig. 4.20A e B, insets), centered at 8 and 5 nm, respectively. All *x*NiCe_ST samples are characterised by a monomodal pore size distribution (Fig. 4.21, insets), though the peaks show an evident tail towards narrower sizes, with a shift of the maximum from about 4 nm to about 8 nm with the increase in Ni content.
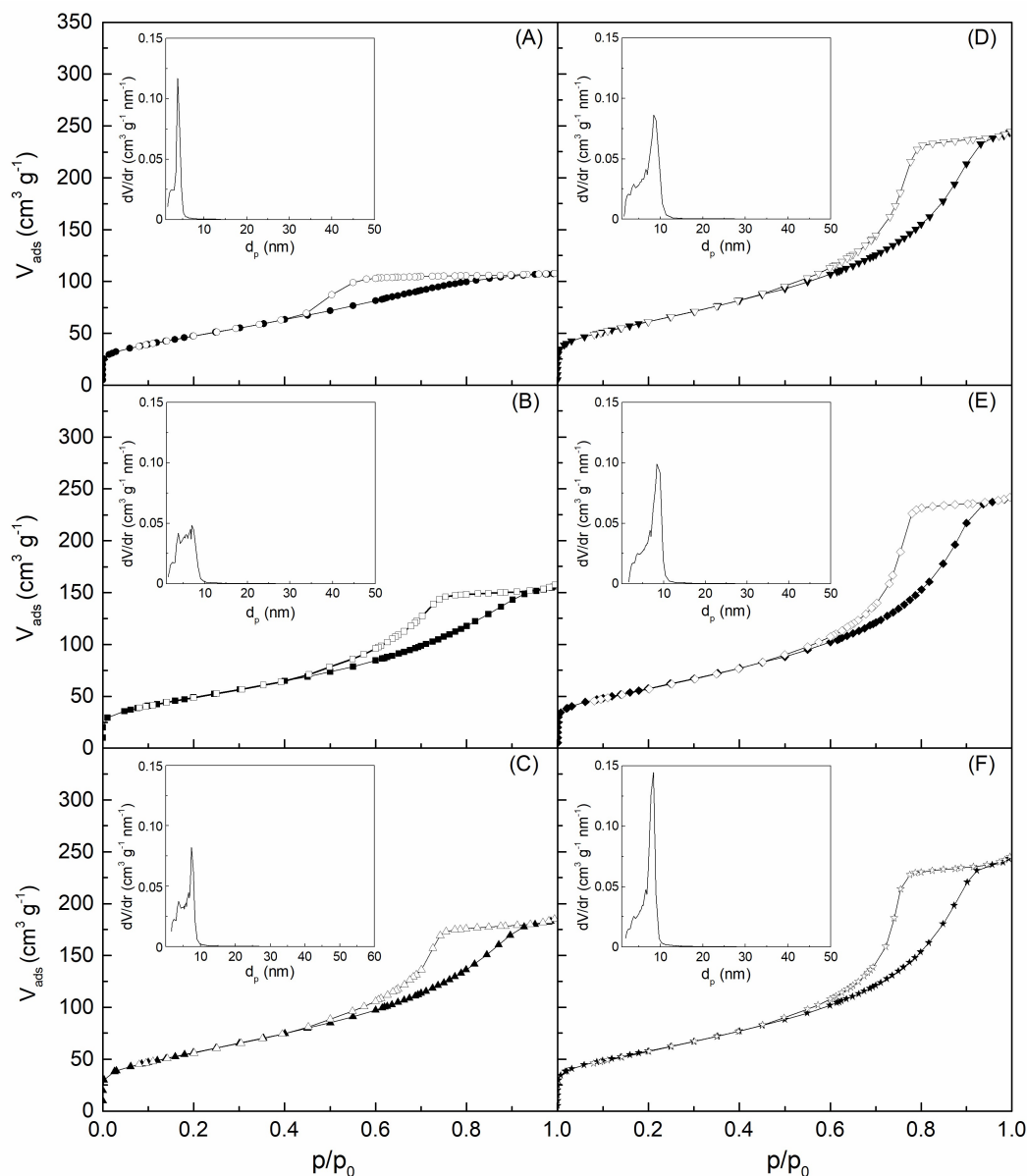


**Fig 4.21.** $N_2$ adsorption/desorption isotherms and pore size distribution (inset) of the *x*NiCe_ST catalysts: (A) 0.3NiCe_ST; (B) 0.5NiCe_ST; (C) 1.0NiCe_ST; (D) 1.5NiCe_ST; (E) 2.5NiCe_ST; (F) 4.0NiCe_ST.

As for $x$NiCe_ST$_{IWI}$ samples, the pore size distribution curves are very similar to those of the ceria support (Fig. 4.22, insets).
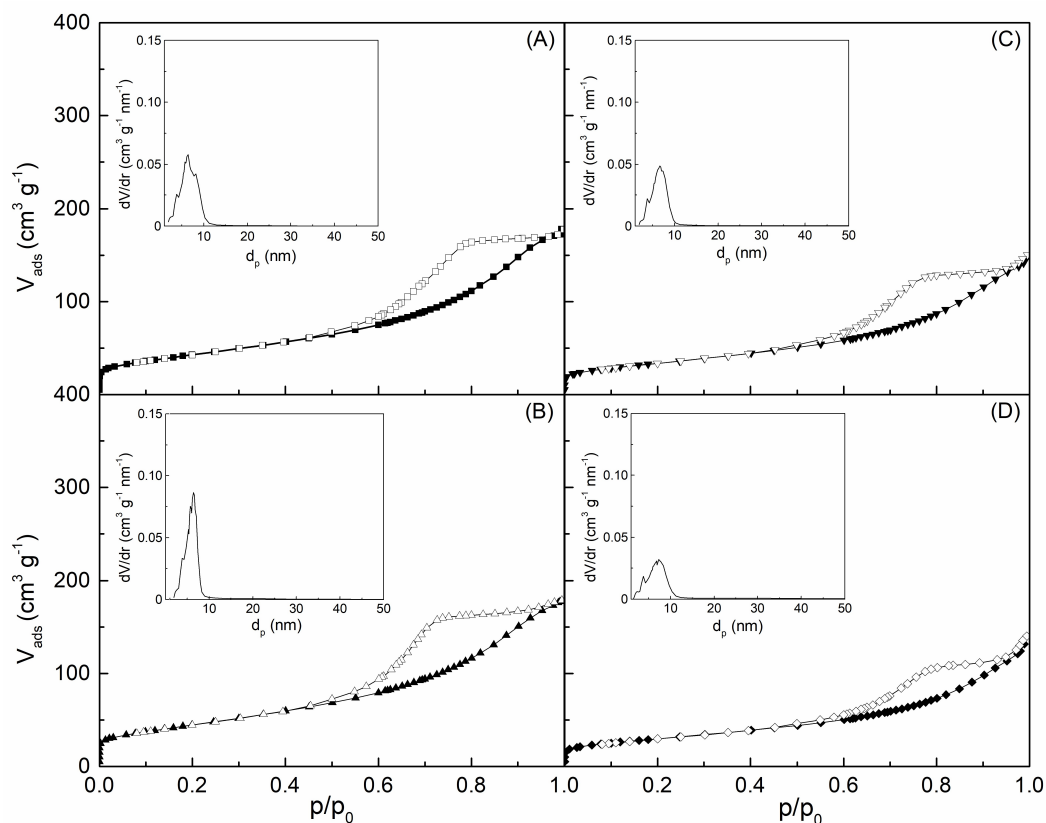


**Fig. 4.22.** N$_2$ adsorption/desorption isotherms and pore size distribution (inset) of the $x$NiCe_ST$_{IWI}$ catalysts: (A) 0.3NiCe_ST$_{IWI}$; (B) 0.5NiCe_ST$_{IWI}$; (C) 1.0NiCe_ST$_{IWI}$; (D) 1.5NiCe_ST$_{IWI}$.

For the pure NiO_ST and CeO$_2$_ST oxides, surface areas (S$_{BET}$) calculated by the BET equation are about 200 m$^2$ g$^{-1}$ (Tab. 4.4), in line with those reported in the literature for cerium oxide synthesized by the soft template method [54,55]. Unlike the case of the $x$NiCe_HT series, whose surface area value was found to decrease at the highest Ni content, for the $x$NiCe_ST catalysts, the S$_{BET}$ values generally increase along with the Ni/Ce molar ratio and are always very high, in the range 174-221 m$^2$ g$^{-1}$ (Tab. 4.4). This result highlights as the soft-template method is able to guarantee excellent textural features irrespective to the catalyst composition.

With regard to the $x$NiCe_ST$_{IWI}$ samples, a manifest decrease in both surface area and pore volume ($V_p$) is observed with the increase in Ni loading (Tab. 4.4), as it was already noted for the NiCe_HT$_{IWI}$ catalysts.

*Raman spectroscopy*

Raman spectra of the soft-templated CeO₂ and of the 1.5NiCe samples obtained by the ST and ST$_{IWI}$ preparation procedures are compared in Fig. 4.23.
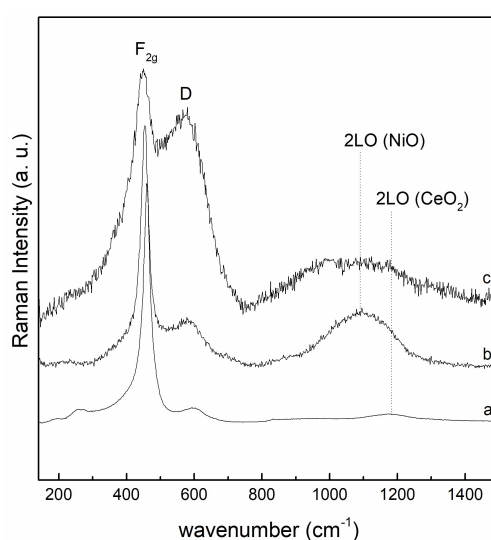


**Fig. 4.23.** Raman spectra of the CeO₂_ST (a), 1.5NiCe_ST$_{IWI}$ (b), and 1.5NiCe_ST (c) samples.

For the CeO₂_ST sample (Fig. 4.23, curve a), the spectrum shows the strong $F_{2g}$ peak at about 460 cm$^{-1}$, and the 2TA, D, and 2LO weak bands at about 260, 580, and 1175 cm$^{-1}$, respectively. Both the 1.5NiCe_ST$_{IWI}$ and 1.5NiCe_ST samples (Fig. 4.23, curves b and c) are characterized by a peak at about 450 cm$^{-1}$ and a band at about 580 cm$^{-1}$, related to the $F_{2g}$ and D modes of CeO₂, respectively, and by a broad feature in the range 1000-1100 cm$^{-1}$ typical of nanostructured NiO. As already observed for the HT series, the presence of Ni causes the broadening of the $F_{2g}$ band as well as its shift to lower frequencies, also accompanied by an increase of the D band intensity. Interestingly, the spectrum of 1.5NiCe_ST (Fig. 4.23, curve c) shows an $F_{2g}$ band significantly wider than that of the 1.5NiCe_ST$_{IWI}$ sample

(Fig. 4.23, curve b), which becomes asymmetric with a low-frequency tail. In addition, the feature at about 580 cm$^{-1}$, related to lattice defects induced into the $CeO_2$ structure in order to maintain charge neutrality after divalent cations incorporation, appears increased in intensity with respect to the $F_{2g}$ mode, suggesting that a higher amount of $Ni^{2+}$ is incorporated into the $CeO_2$ structure. The broad band at $\sim$1090 cm$^{-1}$ (two-phonon, 2LO mode), indicative of the presence of NiO nanoparticles, is instead more intense for 1.5NiCe_ST$_{IWI}$ than for NiCe1.5_ST. In agreement with those formerly reported for the HT and HT$_{IWI}$ series, these evidences confirm that the materials synthesised through the simultaneous use of Ni and Ce precursors are characterised by stronger Ni-Ce interactions, which, as previously underlined, are crucial to ensure a high NiO dispersion.

### 4.3.1.2. H₂-TPR

TPR profiles of the CeO₂_ST and NiO_ST pure oxides, as well as of the $x$NiCe_ST samples are presented in Fig. 4.24. In order to realize a more complete description of the reducibility of the NiCe systems (also related to the bulk reduction of ceria) and to better clarify the difference between the ST and ST$_{IWI}$ catalysts, the H₂-TPR analyses were performed in a wider temperature range, i.e. from 40 °C to 950 °C.



**Fig. 4.24.** H₂-TPR profiles of CeO₂_ST (a), 0.3NiCe_ST (b), 0.5NiCe_ST (c), 1.0NiCe_ST (d), 1.5NiCe_ST (e), 2.5NiCe_ST (f), 4.0NiCe_ST (g), and NiO_ST (h).

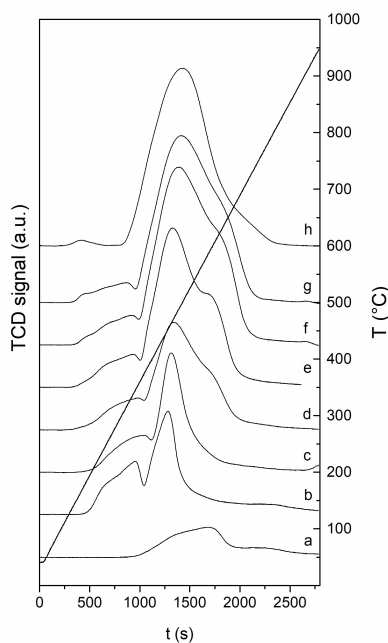The TPR curve of CeO$_2$_ST (Fig. 4.24, profile a) shows a broad peak, starting at 340 °C, with a maximum at ca. 590 °C, and a second contribution, much less intense, centered at about 780 °C. According to the literature [39], the reduction of pure CeO$_2$ basically occurs in two temperature regions: the first between 300 and 600 °C, and the second between 700 and 1000 °C. Such regions are ascribed to surface and bulk reduction processes, respectively. Hence, the first peak in the CeO$_2$_ST profile may be assigned to the abstraction of the surface capping oxygen ions, while the second high-temperature feature is reasonably related to the hard reduction process of the bulk oxide. As for NiO_ST, its profile shows only a single H$_2$-consumption peak centered at about 500 °C (Fig. 4.24, profile h).

In agreement with what already observed for the HT series (cf. par. 4.2.2.2), two main features can be identified in the TPR curves of all the $x$NiCe_ST catalysts (Fig. 4.24, profiles b-g). Once again, an inspection of the shape of the TPR profiles reveals that both the low- and the high-temperature peaks result from the overlapping of different contributions, which indicates the presence of different reducible species. According to the previous observations, the low-temperature feature (α contribution), can be ascribed to the loss of oxygen species adsorbed on defective sites in the solid solution and at the NiO/CeO$_2$ interface, where sites in which Ce and Ni are in close interaction exist. It is worthy to note that, if compared to the results reported for the 0.5NiCe_HT and 1.0NiCe_HT catalysts (Fig. 4.12A), the α peaks appear better defined for the ST samples, suggesting a higher concentration of defective sites. The high-temperature peak can instead be assigned to the reduction of β (NiO dispersed) and γ (NiO strongly interacting with CeO$_2$) species, whose relative concentration would depend on the Ni loading; however, a minor contribution arising from the reduction of the surface capping oxygen of ceria, which starts to occur at about 350 °C (Fig. 4.24, profile a), could also be present.

As for the $x$NiCe_ST$_{IWI}$ catalysts, the reduction profiles are reported in Fig. 4.25. As in the case of the ST series, the appearance of the low-temperature contribution below 380 °C, in the TPR curve of all the samples, is a clear indication of the presence of defective sites. The much more intense peak in the high-temperature region (above 400 °C) may instead be ascribed to the superimposition of the β and γ peaks, whose relative amounts seem to change in favour of the former contribution (due to the presence of NiO as a separate phase) with the increase in the Ni/Ce molar ratio. As a consequence, a decrease in the T$_{max}$ value of such peak is observed.
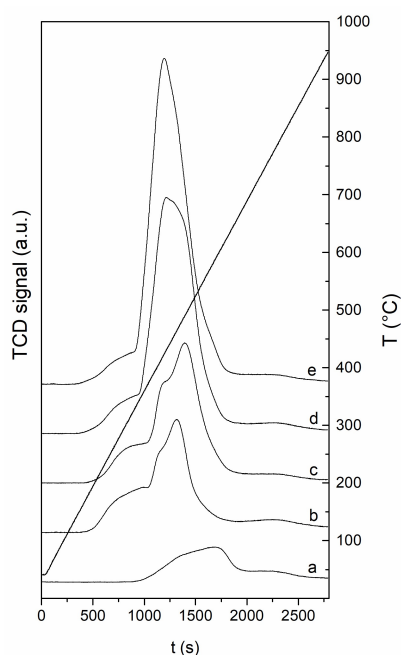
**Fig. 4.25.** H$_2$-TPR profiles of CeO$_2$_ST (a), 0.3NiCe_ST$_{IWI}$ (b), 0.5NiCe_ST$_{IWI}$ (c), 1.0NiCe_ST$_{IWI}$ (d), and 1.5NiCe_ST$_{IWI}$ (e).

By a closer inspection of the TPR profiles, clearly emerges that, compared to the corresponding ST$_{IWI}$ samples, the reduction of the γ species for the 1.0NiCe_ST and 1.5NiCe_ST catalysts occurs at remarkably higher temperatures, suggesting the presence of NiO species with a higher dispersion, which interact more strongly with ceria; it is worthy of note that this conclusion is supported by XRD results, which have shown the presence of very small NiO nanocrystals on the ST samples.

## 4.3.2. Structural characterisation after H$_2$ pretreatment at 400 °C for 1 h

XRD patterns of pure NiO_ST and the *x*NiCe_ST samples are reported in Fig. 4.26, while those of the *x*NiCe_ST$_{IWI}$ mixed oxides are instead reported in Fig. 4.27. For all the samples, the Ni$^0$ crystallite size determined by Scherrer equation are reported in Tab. 4.5.

Pure NiO_ST exhibits the typical signals of the Ni$^0$ phase (Fig. 4.26, pattern a), with an average nanocrystal size of ca. 6 nm. The close size values of Ni$^0$ and original NiO crystals

(about 7 and 4 nm, respectively) support the hypothesis that the presence of the residual NiO may hinder the agglomeration of the $Ni^0$ particles, as suggested in [56].

**Tab. 4.5.** $Ni^0$ crystallite size of the reduced samples.

| Sample | $Ni^0$ crystal size ($D_{Ni}$) (nm) |
|---|---|
| NiO | 6.5 |
| 0.3NiCe_ST | n.p.[a] |
| 0.5NiCe_ST | 7 |
| 1.0NiCe_ST | 6 |
| 1.5NiCe_ST | 6 |
| 2.5NiCe_ST | 8 |
| 4.0NiCe_ST | 8 |
| 0.3NiCe_ST$_{IWI}$ | n.p.[a] |
| 0.5NiCe_ST$_{IWI}$ | 16 |
| 1.0NiCe_ST$_{IWI}$ | 34 |
| 1.5NiCe_ST$_{IWI}$ | 35 |

n.p.[a] (not present): no peaks typical of $Ni^0$ phases were present.

Reflections of the fluorite-type $CeO_2$ cubic phase appear in the XRD patterns of all the *x*NiCe_ST samples. In the case of 0.3NiCe_ST (Fig. 4.26, pattern g), no reflections attributable to any nickel species are detected, probably due to their high dispersion and/or to the detection limits of the technique. For the NiCe_ST catalysts with Ni/Ce molar ratio between 0.5 and 1.5, only signals ascribable to the presence of $Ni^0$ nanocrystals are visible at 2θ values of 44.5° and 51.9° (Fig. 4.26, patterns d-f). An average $Ni^0$ crystallite size of about 6 nm (Tab. 4.5) has been estimated for these samples. Comparison with the NiO crystallite sizes of the fresh catalysts (cf. Tab. 4.4) indicates that only a minor growth of the $Ni^0$ nanocrystals, formed from NiO, takes place during the reduction process. These results are in agreement with those observed for the *x*NiCe_HT samples, confirming that the presence of NiO and $CeO_2$ in close interaction, highlighted by Raman and TPR evidences, prevents the occurrence of severe sintering phenomena. In the case of 2.5NiCe_ST and 4.0NiCe_ST (Fig. 4.26, patterns c and b), besides reflections assignable to the $Ni^0$ phase, the appearance of weak and wide signals at 2θ values of 37.3°, 43.3°, and 62.9° are indicative of the existence of residual NiO. However, a minor

contribution of nickel oxide deriving from re-oxidation of the catalyst surface due to exposure to air prior to the XRD measurements cannot be excluded. $Ni^0$ nanocrystals of ca. 8 nm in diameter (Tab. 4.5), i.e. only moderately larger than the parent NiO particles (cf. Tab. 4.4), are present on these samples, pointing out that no significant sintering phenomena occur during the reduction process, regardless of the Ni content.
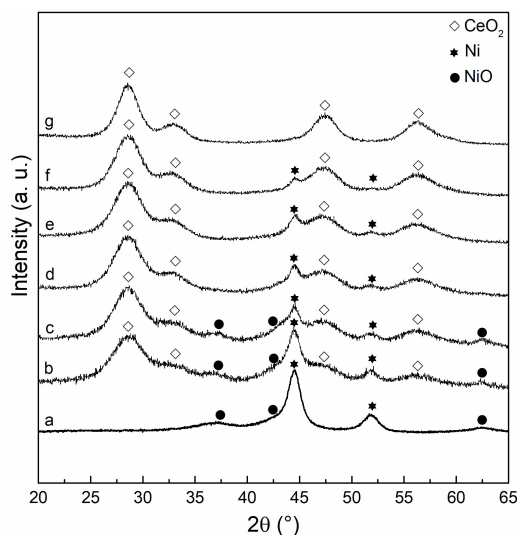


**Fig. 4.26.** Wide angle X-ray diffraction of NiO_ST (a), 4.0NiCe_ST (b), 2.5NiCe_ST (c), 1.5NiCe_ST (d), 1.0NiCe_ST (e), 0.5NiCe_ST (f), and 0.3NiCe_ST (g), after $H_2$-pretreatment at 400 °C for 1 h.

TEM analysis confirms this picture: the morphology of the particles of reduced 0.5NiCe_ST and 2.5NiCe_ST catalysts (Fig. 4.27A and B, respectively) is similar to that observed for the fresh samples.
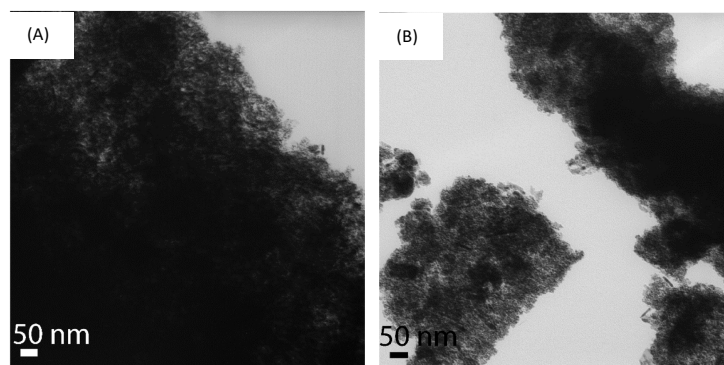


**Fig. 4.27.** TEM images of selected *x*NiCe_ST catalysts after $H_2$-pretreatment at 400 °C for 1 h: (A) 0.5NiCe_ST; (B) 2.5NiCe_ST.

Fig. 4.28 shows the XRD patterns of the $x$NiCe_ST$_{IWI}$ catalysts after the reduction pretreatment. Reflections of the $CeO_2$ phase appear in the diffractogram of all the samples. In the case of 0.3NiCe_ST$_{IWI}$ (Fig. 4.28, pattern d), only a very low signal corresponding to the most intense reflection ($2\theta = 44.5°$) of the $Ni^0$ phase is observable, indicating that the formed $Ni^0$ nanocrystals are well dispersed on the ceria support. Defined peaks typical of metallic nickel are instead visible for the other $x$NiCe_ST$_{IWI}$ catalysts, the presence of residual NiO being not observed. The calculated $Ni^0$ crystallite size values are in the range 15-35 nm (Tab. 4.5). By comparing these values with those of the original NiO nanocrystals on the fresh catalysts (Tab. 4.4), only a slight increase in size is observed for the 0.5NiCe_ST$_{IWI}$ sample, whereas in the case of 1.0NiCe_ST$_{IWI}$ and 1.5NiCe_ST$_{IWI}$, considerably larger $Ni^0$ nanocrystals are formed after reduction. It is worth to remind that a similar trend was observed for the HT$_{IWI}$ series, pointing out that, compared to the ST and HT samples, the establishing of weaker NiO-CeO₂ interactions on the IWI catalysts are responsible for the higher agglomeration of the particles during the H₂-pretreatment.
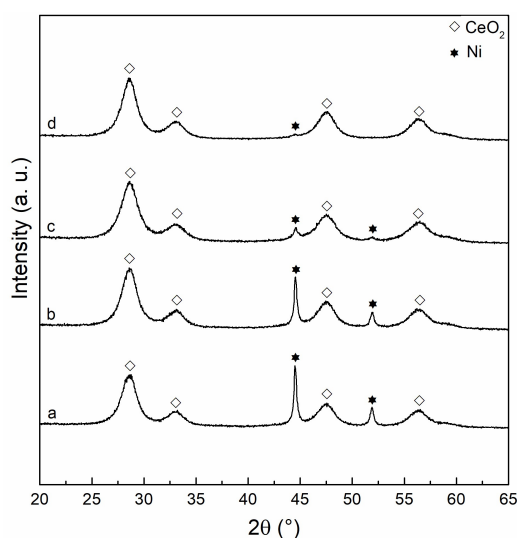


**Fig. 4.28.** Wide angle X-ray diffraction of 1.5NiCe_ST$_{IWI}$ (a), 1.0NiCe_ST$_{IWI}$ (b), 0.5NiCe_ST$_{IWI}$ (c), and 0.3NiCe_ST$_{IWI}$ (d), after H₂-pretreatment at 400 °C for 1 h.

### 4.3.3. Catalytic results

Catalytic results for the pure NiO_ST, as well as the $x$NiCe_ST and $x$NiCe_ST$_{IWI}$ samples are summarised in Tab. 4.6. Reaction tests were performed at 300 °C and 1 atm by using 0.050 g of catalyst, with a H₂/CO₂ molar ratio equal to 4.3 mol mol$^{-1}$ and space velocity 72000 cm$^3$ h$^{-1}$ g$_{cat}$$^{-1}$. While CeO₂_ST confirmed the inability of pure ceria to catalyse CO₂

methanation, pure NiO_ST as well as the $x$NiCe_ST and $x$NiCe_ST$_{IWI}$ catalysts are highly active and stable within 6 h on stream.

**Tab. 4.6.** Catalytic results for NiO_ST, $x$NiCe_ST and $x$NiCe_ST$_{IWI}$. Reaction condition; T = 300 °C; P = 1 atm; $m_{cat}$ = 0.050 g; SV = 72000 cm³ h⁻¹ g$_{cat}$⁻¹; H₂/CO₂ = 4.3 mol mol⁻¹

| Sample | CO₂ conversion (mol%) | CH₄ selectivity (mol%) |
|---|---|---|
| NiO | 64 | 98 |
| 0.3NiCe_ST | 70 | > 99 |
| 0.5NiCe_ST | 73 | > 99 |
| 1.0NiCe_ST | 84 | > 99 |
| 1.5NiCe_ST | 87 | > 99 |
| 2.5NiCe_ST | 86 | > 99 |
| 4.0NiCe_ST | 86 | > 99 |
| 0.3NiCe_ST$_{IWI}$ | 69 | > 99 |
| 0.5NiCe_ST$_{IWI}$ | 74 | > 99 |
| 1.0NiCe_ST$_{IWI}$ | 78 | > 99 |
| 1.5NiCe_ST$_{IWI}$ | 83 | > 99 |

### 4.3.3.1. NiO_ST and $x$NiCe_ST

For the series ST, the CO₂ conversion increases with the Ni/Ce molar ratio up to 1.5 and then remains almost constant at about 86 mol%. CH₄ selectivity is always very close to 100 mol%, only traces of CO being detected. A lower conversion (64 mol%) is observed on NiO_ST, which also shows a slight decrease in CH₄ selectivity (98 mol%). By taking into account the comparable Ni⁰ nanocrystal size of the NiCe_ST mixed oxides and the pure NiO, the superior activity of the $x$NiCe_ST is a confirmation of the beneficial effect of ceria. By comparing the catalytic activity of the soft- and hard-templated materials (cf. Tab. 4.3), it can be seen that, though the 0.5NiCe catalysts give very similar CO₂ conversion (73 and 70 mol% for ST and HT, respectively), a clear difference in the catalytic behaviour is observed for the 1.0NiCe samples (84 and 76 mol% for ST and HT, respectively). At the current state of the discussion, when the crucial effect of a high Ni/CeO₂ interface has already been stated, the higher performance of 1.0NiCe_ST with respect to that of 1.0NiCe_HT can be reasonably

ascribed to the presence of both smaller $Ni^0$ (6 and 16 nm, respectively) and $CeO_2$ (3 and 6 nm, respectively) nanoparticles.

The occurrence of the already discussed reaction mechanism, according to which $CO_2$ is activated on ceria (through the formation of oxygenated intermediates), while $H_2$ is activated by dissociative adsorption on $Ni^0$ particles, can be confidently proposed also for the *x*NiCe_ST catalysts, for which the small size of both $CeO_2$ and $Ni^0$ nanoparticles (cf. Tabs 4.4 and 4.5) assures a large metal-support interface, and the presence of a close interaction between well dispersed NiO species and ceria (leading to a high concentration of defective sites) is supported by both Raman and TPR results (cf. Fig. 4.23 and 4.24, respectively).

By taking into account that $CO_2$ adsorption and activation are considered to be favoured on medium basic sites [11,19], $CO_2$ adsorption microcalorimetry has been used to investigate the surface basic properties of pure $CeO_2$_ST and of selected *x*NiCe_ST catalysts (previously reduced at 400 °C for 1 h). The results are shown in Fig. 4.29, where the differential heat of adsorption ($Q_{diff}$) is plotted versus the $CO_2$ uptake. It can be observed that $Q_{diff}$ always decreases as the $CO_2$ uptake increases, thus indicating a high heterogeneity of the adsorbing sites. The presence of strong basic sites (which are generally identified as sites with differential adsorption heats > 150 kJ $mol^{-1}$) on all the investigated samples is revealed by their high initial $Q_{diff}$ value (about 200 kJ $mol^{-1}$). It is interesting to note that the calorimetric curves of the *x*NiCe_ST samples are all above the one of pure $CeO_2$_ST, thus indicating a higher concentration of $CO_2$-adsorbing sites.
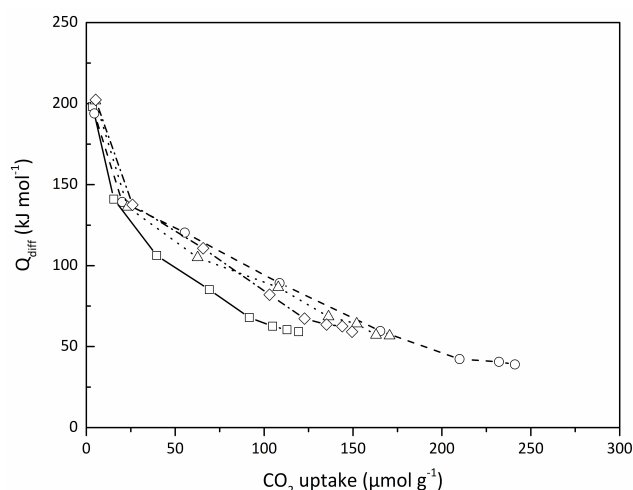


**Fig. 4.29.** Differential heats versus $CO_2$ uptake at 80 °C for $CeO_2$_ST (□), 0.3NiCe_ST (○), 1.0NiCe_ST (△), and 2.5NiCe_ST (◇).

By comparing the results of the adsorption and re-adsorption experiments, it is possible to evaluate the amount of probe molecule irreversibly adsorbed, as well as the corresponding value of the adsorption heat. In the present case, it has been found that $CO_2$ is irreversibly adsorbed on basic sites with $Q_{diff}$ values $\geq 100$ kJ mol$^{-1}$; hence, this value has been considered as the threshold value to distinguish between "weak" and "medium" sites. Accordingly, a rough distribution of the basic sites strength can be done as follows: weak sites (not able to efficiently activate carbon dioxide), $60 < Q_{diff}$ (kJ mol$^{-1}$) $< 100$; medium sites, $100 \leq Q_{diff}$ (kJ mol$^{-1}$) $\leq 150$; strong sites, $Q_{diff}$ (kJ mol$^{-1}$) $> 150$. The results are reported in Tab. 4.7, where the percentage of the sites of different strength with respect to the total basic sites number is also shown (values in brackets). It can be observed from the table that the presence of Ni leads to an increase in the medium-strength sites number (considered essential for $CO_2$ activation), probably because of the formation of defective sites originating from the Ni-Ce solid solution formation.

**Tab. 4.7.** Sites strength distribution by calorimetric results on selected ST samples.

| Sample | Weak[a] $n_{CO2}$ (µmol g$^{-1}$) | Medium[b] $n_{CO2}$ (µmol g$^{-1}$) | Strong[c] $n_{CO2}$ (µmol g$^{-1}$) |
|---|---|---|---|
| CeO₂ | 66 (58 %) | 35 (30 %) | 14 (12 %) |
| 0.3NiCe_ST | 74 (45 %) | 73 (45 %) | 17 (10 %) |
| 1.0NiCe_ST | 84 (53 %) | 55 (35 %) | 19 (12 %) |
| 2.5NiCe_ST | 68 (46 %) | 58 (39 %) | 22 (15 %) |

[a]Weak: $60 < Q_{diff}$ (kJ mol$^{-1}$) $< 100$; [b]medium: $100 < Q_{diff}$ (kJ mol$^{-1}$) $< 150$; strong: $Q_{diff}$ (kJ mol$^{-1}$) $> 150$.

To confirm the existence of hydrogen carbonates and carbonates species, formed through the interaction between $CO_2$ and basic sites on ceria, FTIR analyses were performed on pure $CeO_2$ and on selected $x$NiCe_ST catalysts, previously reduced with $H_2$ at 400 °C for 1 h (Fig. 4.30). The FTIR spectra, collected after $CO_2$ adsorption at room temperature, reveal the presence of hydrogen carbonates and monodentate/bidentate carbonates, thus further supporting the occurrence of a mechanism not involving CO as the intermediate.
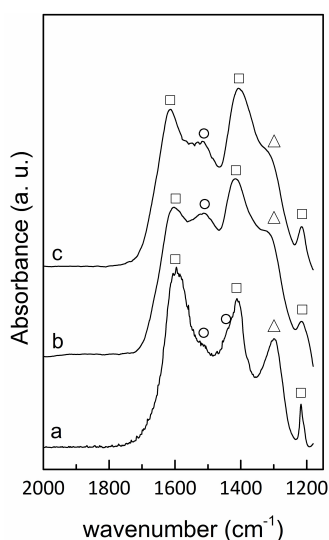
**Fig. 4.30.** FTIR spectra of the reduced CeO₂_ST, 0.3NiCe_ST, and 2.5NiCe_ST catalysts after CO₂ adsorption (equilibrium pressure = 50 mbar) at room temperature. (□) Hydrogen carbonate; (○) monodentate carbonate; (Δ) bidentate carbonate.

In the case of NiO_ST, the absence of ceria implies that both $CO_2$ and $H_2$ must be activated on $Ni^0$ particles, which leads to a decrease in catalytic activity. However, $CO_2$ conversion on NiO_ST is surprisingly higher in comparison with the values reported in [57] for $Ni^0$ nanoparticles, prepared by reduction method in aqueous solution, of about 8 nm in size (0 mol% at 300 °C and 0.4 mol% at 400 °C), and in [53] for much larger $Ni^0$ nanoparticles (200-400 nm), formed by $H_2$ reduction of NiO at 700 °C for 1 h (8 mol% at 300 °C). In this latter case, 71 mol% of CO selectivity was observed, which was ascribed to the occurrence of the reverse water gas shift reaction on active sites located on extended $Ni^0$ faces. Higher $CO_2$ conversions and $CH_4$ selectivity were obtained for $Al_2O_3$-supported nickel catalysts, where Ni species strongly interacting with the support were suggested to be needed for activating $CO_2$ and/or intermediate CO, preventing its desorption and promoting fast methanation. The lack of activity for the small $Ni^0$ nanoparticles was thus ascribed to the absence of extended $Ni^0$ faces as well as of nickel-support interactions. In the present case, it might be suggested that NiO remaining after the reduction process can have a role in activating $CO_2$ through the formation of oxygenated intermediates, providing at the same time a metal/oxide interface at which highly uncoordinated (because of the small size of the $Ni^0$ nanoparticles) Ni atoms exist, which are responsible for the rapid conversion to methane of both the oxygenated and CO intermediates.

*Influence of time-on-strem, temperature, H₂/CO₂ molar ratio, and space velocity*

Additional catalytic tests have been performed on 4.0NiCe_ST, i.e. the sample with the highest Ni content, to investigate the catalyst stability and the activity at different operating regimes. $CH_4$ selectivity was always > 99 mol%, regardless of the adopted experimental conditions. The plot of $CO_2$ conversion as a function of time-on-stream is displayed in Fig. 4.31, where the catalyst is shown to be very stable within 34 h on stream at both the investigated SV values (72000 and 237000 cm³ h⁻¹ $g_{cat}^{-1}$, respectively).
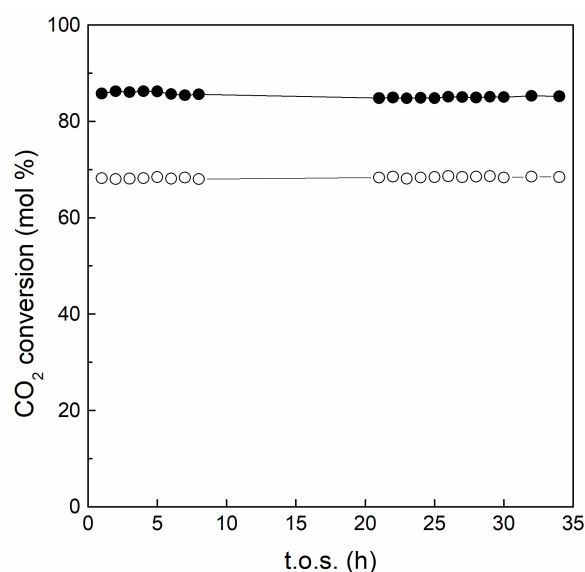


**Fig. 4.31.** $CO_2$ conversion as a function of time-on-stream for the 4.0NiCe_ST catalyst: (●) SV = 72000 cm³ h⁻¹ $g_{cat}^{-1}$; (○) SV = 237000 cm³ h⁻¹ $g_{cat}^{-1}$.

The influence of reaction temperature, H₂/CO₂ molar ratio, and space velocity is shown in Fig. 4.32, where the equilibrium conversion values are also reported for comparison. From 200 to 350 °C $CO_2$ conversion rises with temperature and then slightly diminishes (Fig. 4.32A). It is worthy of note that, despite the high SV value (72000 cm³ h⁻¹ $g_{cat}^{-1}$), thermodynamic equilibrium is approached at 300 °C, and then achieved at 350 and 400 °C. The good performance of the catalyst is confirmed by the results obtained at different H₂/CO₂ molar ratios, which show that $CO_2$ conversion at 300 °C is always very close to the equilibrium values (Fig. 4.32B). The catalytic activity as a function of space velocity (Fig. 4.32C) shows a steep decrease in the range 48000-240000 cm³ h⁻¹ $g_{cat}^{-1}$ and then decreases more smoothly.

Interestingly, a significant conversion (60 mol%) is obtained even at the highest SV value (908000 cm$^3$ h$^{-1}$ g$_{cat}^{-1}$).
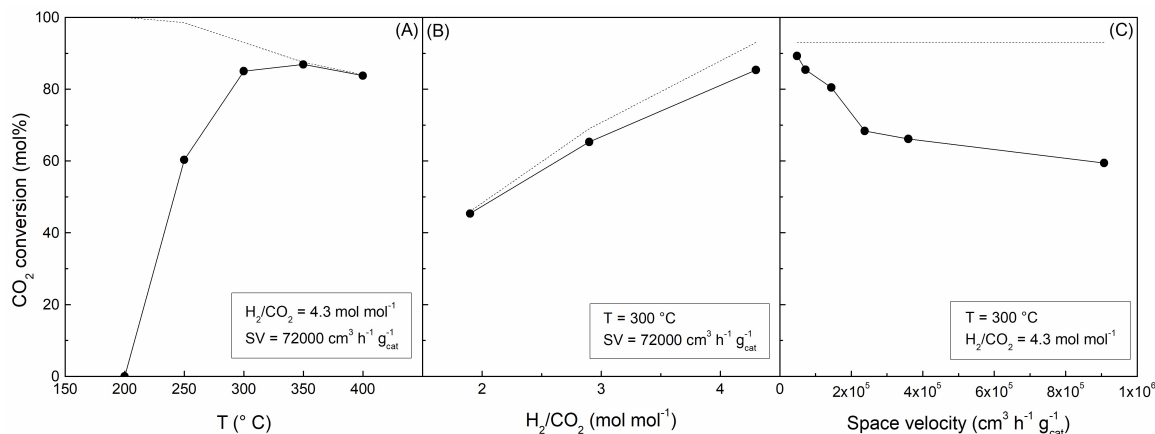


**Fig. 4.32.** $CO_2$ conversion for the 4.0NiCe_ST catalyst as a function of: (A) reaction temperature; (B) $H_2/CO_2$ molar ratio; (C) space velocity. Dashed lines represent equilibrium conversion.

The influence of the Ni/Ce molar ratio on the catalytic behaviour at 908000 cm$^3$ h$^{-1}$ g$_{cat}^{-1}$ has also been investigated on selected NiCe_ST samples and the results are compared with those obtained at 72000 cm$^3$ h$^{-1}$ g$_{cat}^{-1}$ in Fig. 4.33.
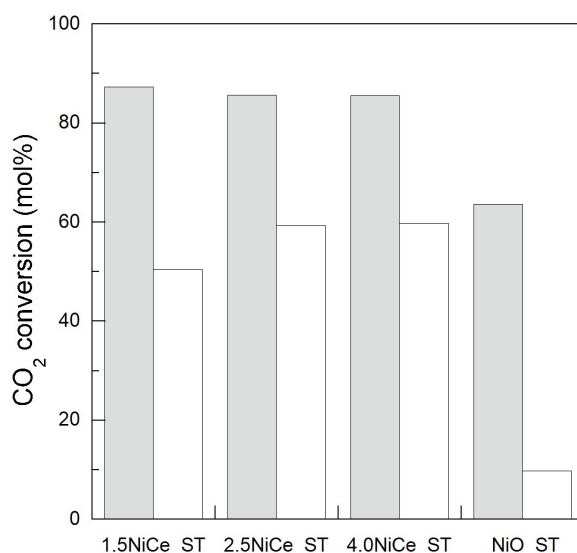


**Fig. 4.33.** $CO_2$ conversion for the *x*NiCe_ST catalysts as a function of Ni/Ce molar ratio at different space velocity values: (■) 72000 cm$^3$ h$^{-1}$ g$_{cat}^{-1}$; (□) 908000 cm$^3$ h$^{-1}$ g$_{cat}^{-1}$.

As expected, a decrease in $CO_2$ conversion with the increase in SV occurs in all cases. In the case of the pure NiO_ST, such decrease is rather high, highlighting the pivotal role of ceria in activating $CO_2$ at the nickel-support interface. In addition, an increase in CO selectivity was detected (15 mol%). For the *x*NiCe_ST mixed oxides, $CH_4$ selectivity was always > 99 mol%, the most pronounced lowering of activity being observed for the catalyst with the lowest Ni content (Fig. 4.33). This result may be explained by the decrease in concentration of $Ni^0$ active sites with the diminution in Ni amount.

### 4.3.3.2. *x*NiCe_ST$_{IWI}$

Catalytic results for the *x*NiCe_ST$_{IWI}$ samples (Tab. 4.6) show an increase in $CO_2$ conversion along with the Ni/Ce molar ratio, with $CH_4$ selectivity values higher than 99 mol% regardless of the Ni loading. It is worthy of note that, as already observed for 0.5NiCe_HT and 0.5NiCe_HT$_{IWI}$, despite the larger $Ni^0$ crystal size of the *x*NiCe_ST$_{IWI}$ catalysts compared to that of *x*NiCe_ST (cf. Tab. 4.5), similar $CO_2$ conversion values are observed for the two series (Tab. 4.6). Another interesting result comes out by comparing the catalytic activity of 0.5NiCe_ST$_{IWI}$ and 1.0NiCe_ST$_{IWI}$ ($D_{Ni0}$ = 16 and 34 nm, respectively) with that of 0.5NiCe_HT$_{IWI}$ and 1.0NiCe_HT$_{IWI}$ ($D_{Ni0}$ = 19 and 34 nm, respectively) at 72000 cm$^3$ h$^{-1}$ g$_{cat}^{-1}$. Indeed, notwithstanding the very similar $Ni^0$ crystals size, 0.5NiCe_ST$_{IWI}$ and 1.0NiCe_ST$_{IWI}$ ($CO_2$ conversion = 74 and 78 mol%, respectively) exhibit higher activity with respect to the corresponding 0.5NiCe_HT$_{IWI}$ and 1.0NiCe_HT$_{IWI}$ catalysts ($CO_2$ conversion = 66 and 57 mol%, respectively). These results could be explained by considering the different $CeO_2$ nanocrystals size obtained for the ST$_{IWI}$ and HT$_{IWI}$ series (5 and 9 nm, respectively), suggesting that the presence of small ceria nanoparticles can also significantly affect the catalytic performance.

*Influence of time-on-strem, temperature, H₂/CO₂ molar ratio, and space velocity*

The influence of time-on-stream, reaction temperature, and space velocity on the activity has been investigated on the 1.5NiCe_ST$_{IWI}$ sample (Fig. 4.34).

It can be seen in Fig. 4.34A that the catalyst does not deactivate up to 34 h on stream and shows a trend of conversion vs. temperature (Fig. 4.34B) similar to that of the 4.0NiCe_ST

sample (cf. Figs. 4.31 and 4.32A). A marked lowering of conversion is evident at a SV value of 908000 $cm^3$ $h^{-1}$ $g_{cat}^{-1}$ (Fig. 4.34C), which is accompanied by an increase in CO selectivity (13 mol%). Such an increase in CO selectivity can be explained by the occurrence of the reverse water gas shift catalysed by the extended Ni faces on the large $Ni^0$ particles, according to what has already been reported for the 0.5NiCe_HT$_{IWI}$ sample (cf. par. 4.2.4.3).
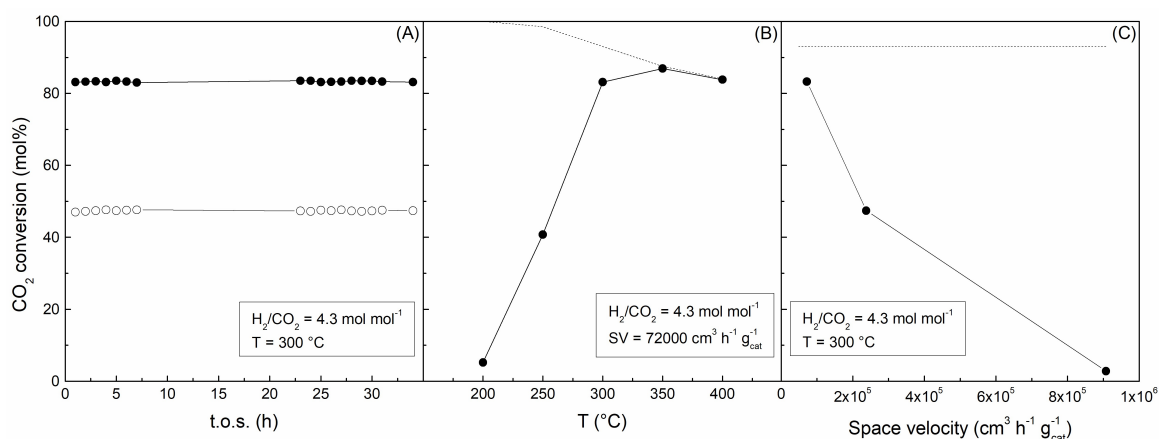


**Fig. 4.34.** CO₂ conversion for the 1.5NiCe_ST$_{IWI}$ catalyst as a function of: (A) time-on-stream; (B) reaction temperature; (C) space velocity. Dashed lines represent equilibrium conversion.

### 4.3.3.3. Comparison of the catalytic performance of 1.5NiCe_ST and 1.5NiCe_ST$_{IWI}$

The catalytic performance of the 1.5NiCe_ST and 1.5NiCe_ST$_{IWI}$ catalysts has been compared at different experimental conditions and the results are summarized in Tab. 4.8.

At 72000 $cm^3$ $h^{-1}$ $g_{cat}^{-1}$, a similar CO₂ conversion, not so far from thermodynamic equilibrium (93 mol%), is obtained at 300 °C. On both catalysts, equilibrium conversion values are instead achieved at 350 (87 mol%) and 450 °C (84 mol%). By converse, for the ST$_{IWI}$ sample, a CO₂ conversion about 15 mol% lower than that obtained on the ST catalyst is observed at 250 °C. An increasing difference in CO₂ conversion is also observed at increasing values of space velocity, which becomes dramatic at the highest value of this parameter (50 and 3 mol% for 1.5NiCe_ST and 1.5NiCe_ST$_{IWI}$, respectively).

**Tab. 4.8.** Specific metal surface area and catalytic results for the 1.5NiCe_ST and 1.5NiCeST$_{IWI}$ catalysts at different reaction conditions: P = 1 atm; $H_2/CO_2$ = 4.3 mol mol$^{-1}$.

| Sample | $A_{met}$ $(m_{(Ni^0)}^2 g_{cat}^{-1})$ | $T_R$ (°C) | SV $(cm^3\ h^{-1}\ g_{cat}^{-1})$ | Conversion (mol%) | Specific activity x 10$^{-18}$ $(molec_{CO_2,transf}\ m_{(Ni^0)}^{-2}\ s^{-1})$ |
|---|---|---|---|---|---|
| 1.5NiCe_ST | 8.9 | 300 | 72000 | 87 | 2.5 |
| | | 300 | 237000 | 70 | 6.7 |
| | | 300 | 908000 | 50 | 18.8 |
| | | 250 | 72000 | 54 | 1.6 |
| | | 350 | 72000 | 87 | 2.5 |
| | | 400 | 72000 | 84 | 2.4 |
| 1.5NiCe_ST$_{IWI}$ | 7.0 | 300 | 72000 | 83 | 3.0 |
| | | 300 | 237000 | 47 | 5.5 |
| | | 300 | 908000 | 3 | 1.3 |
| | | 250 | 72000 | 41 | 1.5 |
| | | 350 | 72000 | 87 | 3.2 |
| | | 400 | 72000 | 84 | 3.0 |

Also in this case, to more closely inspect the catalytic behaviour, the metal surface area was determined by $H_2$ pulse chemisorption on the catalysts previously submitted to the $H_2$ reduction pretreatment at 400 °C. The specific metal surface area values ($A_{met}$), reported in Tab. 4.8, correspond to 8.9 and 7.0 $m_{(Ni^0)}^2\ g_{cat}^{-1}$ for 1.5NiCe_ST and 1.5NiCe_ST$_{IWI}$, respectively. It is noteworthy that the difference in the $A_{met}$ values for the two catalysts is considerably lower than that which would be expected in view of the size of their $Ni^0$ nanocrystals (cf. Tab. 4.5). However, for the 1.5NiCe_ST catalyst, TPR results (which showed a clearly distinguishable contribution of NiO γ-species reducible at temperatures well above 500 °C) as well as Raman analysis (which confirmed the occurrence of strong interactions between the well dispersed NiO nanoparticles and the ceria support), suggested that a higher amount of the original nickel oxide (on which $H_2$ does not chemisorb) can remain unreduced in comparison with the ST$_{IWI}$ sample. Hence, the moderate value of the metal surface area shown by 1.5NiCe_ST may be explained accordingly.

From the metal surface area values, specific activity can be calculated under different reaction conditions. However, it should be considered that, under conditions where thermodynamic equilibrium is reached or is approached, catalytic activity is levelled out.

Hence, in such conditions, the slightly higher specific activity of 1.5NiCe_ST$_{IWI}$ compared to that of the ST catalyst is not surprising, by taking into account the higher A$_{met}$ value of the latter. A better catalytic performance can be observed on the 1.5NiCe_ST sample at increasing values of space velocity, while a comparable specific activity is shown by the two catalysts at 250 °C and 72000 cm$^3$ h$^{-1}$ g$_{cat}^{-1}$ (Tab 4.8). The activity trend as a function of space velocity is similar to that emerged by comparing the catalytic performance of 0.5NiCe_HT and 0.5NiCe_HT$_{IWI}$ (cf. par. 4.2.4.3). This behaviour might be explained bearing in mind that $CO_2$ and $H_2$ are activated on different active sites, provided by $CeO_2$ and Ni$^0$, respectively. H atoms for the $CO_2$-intermediates hydrogenation would derive by $H_2$ dissociatively adsorbed on the highly uncoordinated Ni atoms at the metal-support interface (which can reasonably be suggested as the most active sites for such dissociative adsorption) and on the surface of the Ni$^0$ particles, from which they can move towards the ceria support through a spill-over process, as suggested in [58]. Most likely, at low and moderate values of space velocities, active hydrogen can be supplied by Ni atoms located both on the surface and at the perimeter of the Ni$^0$ particles, in amounts high enough to convert almost all the reaction intermediates formed through $CO_2$ adsorption on the support. In such situation, the size of the Ni$^0$ nanocrystals is not a decisive factor for activity. By contrast, at very high space velocities, only the most active sites, i.e. the highly uncoordinated Ni atoms at the metal-support interface, would be still available to easily hydrogenate $CO_2$ activated on the nearby ceria sites. The number of such "perimeter" atoms, which strongly depends on the mean particle size (in [59], it has been reported to be proportional to $D_p^{-2}$, where $D_p$ is the metal particle diameter) becomes very important in determining catalytic activity. Hence, the specific activity value shown at 908000 cm$^3$ h$^{-1}$ g$_{cat}^{-1}$ by the 1.5NiCe_ST sample, which is about 14 times higher than that of the ST$_{IWI}$ sample, can be ascribed to the large difference in the number of the Ni atoms at the perimeter of the Ni$^0$ nanoparticles.

### 4.3.4. Conclusions

As expected, both the ST and ST$_{IWI}$ mixed oxides series were found to be very active and selective towards methanation after a $H_2$-pretreatment at mild conditions (400 °C for 1 h), while the lower conversion observed for NiO confirmed the pivotal role of ceria in the reaction mechanism. Unlike to what observed for the $x$NiCe_HT series, for the ST samples, NiO

nanocrystals of about 4 nm in size were obtained, highlighting the better capacity of the soft-template method in ensuring a very high NiO dispersion irrespective of Ni loading. Such small nanocrystals did not suffer of significative growth after the reduction pretreatment ($Ni^0$ crystals of ca. 7 nm were formed), confirming that the presence of strong interactions with the ceria support prevent the occurrence of severe sintering phenomena. Once again, the deposition of Ni by the impregnation technique led to the formation of larger NiO nanocrystals, whose diameter was found to increase with the increase in Ni loading. $Ni^0$ crystallites of more than 30 nm in size were then originated by their agglomeration during the reduction at 400 °C. Confirming what observed for 0.5NiCe_HT and 0.5NiCe_HT$_{IWI}$, in spite of the significantly different $Ni^0$ crystal size, comparable $CO_2$ conversion values were observed for the *x*NiCe_ST and *x*NiCe_ST$_{IWI}$ catalysts at the standard reaction conditions. As for the IWI catalysts, although very similar $Ni^0$ crystal sizes were estimated for HT$_{IWI}$ and ST$_{IWI}$ samples with comparable Ni content, a higher catalytic activity was obtained by using CeO$_2$_ST as the support, probably because of the presence of smaller ceria nanoparticles compared to CeO$_2$_HT.

At variance with the ST$_{IWI}$ catalysts, the ST samples were generally found to show superior performances at increasing space velocities. At the highest SV value, $CO_2$ conversion values of 60 and 50 mol% were observed for 4.0NiCe_ST and 1.5NiCe_ST, respectively, which were much more higher than the value (3 mol%) shown by 1.5NiCe_ST$_{IWI}$. A comparison between the 1.5NiCe_ST and 1.5NiCe_ST$_{IWI}$ catalysts was also performed, under different reaction conditions, in terms of specific activity, calculated as molecules$_{(CO2,transformed)}$ $m_{(Ni^0)}^{-2}$ $s^{-1}$. At 72000 cm$^3$ h$^{-1}$ g$_{cat}^{-1}$, despite the higher value of the metal surface area of the 1.5NiCe_ST, they showed comparable catalytic activities both at 250 and 300 °C. These results confirm that $H_2$ activation on $Ni^0$ nanocrystals is not the critical step for a high catalytic activity at such conditions, once more pointing out the important role of the ceria support in the reaction pathway. By contrast, a much higher value of specific activity was shown by 1.5NiCe_ST at the highest value of space velocity. The proposed explanation is that, in these conditions, only the highly uncoordinated Ni atoms at the metal-support interface, whose number strongly depends on the mean particle size, remain available to hydrogenate $CO_2$ activated on the nearby ceria sites. Therefore, large $Ni^0$ nanocrystals, which ensure a good catalytic performance at the usual experimental conditions, appear not adequate in preserving a high catalytic activity in a wide range of reaction conditions.

## 4.4. The role of the support on the activity of Ni-based catalysts

In the previous paragraphs, the high catalytic performance of the $NiO/CeO_2$ catalysts was proved. The results clearly showed that ceria plays a pivotal role both as a support and as a promoter, being able to positively affect the reducibility of the catalysts and favour the activation of $CO_2$. To better emphasise the influence of ceria on the activity of Ni-based catalysts, $CO_2$ methanation was also performed on a $NiO/\gamma$-$Al_2O_3$ catalyst prepared by *Incipient Wetness Impregnation* (IWI) method, being $\gamma$-alumina the most investigated and used support on an industrial-scale. For this catalyst, named NiAl_IWI, a content of Ni equal to 25 wt% ($g_{Ni}/g_{cat}$) was chosen in order to compare its properties and catalytic performance with those of $1.0NiCe\_HT_{IWI}$ and $1.0NiCe\_ST_{IWI}$, which have a very similar Ni content (24.1 and 23.7 wt%, respectively).

### 4.4.1. Characterisation of fresh NiAl_IWI

#### 4.4.1.1. Chemical composition, structural and textural characterisation

In Tab. 4.9, the chemical composition as well as the structural and textural properties of the NiAl_IWI catalyst and $\gamma$-$Al_2O_3$ support are reported.

**Tab. 4.9.** Chemical composition, structural and textural properties of fresh NiAl_IWI and $\gamma$-$Al_2O_3$.

| Sample | $g_{Ni}/g_{cat}$ (%) | Crystal phases | Crystal size $D_c$ (nm) | $S_{BET}$ (m² g⁻¹) | $V_p$ (cm³ g⁻¹) |
|---|---|---|---|---|---|
| $\gamma$-$Al_2O_3$ | - | $\gamma$-$Al_2O_3$ | 4 | 188 | 0.48 |
| NiAl_IWI | 25.0 | NiO; $\gamma$-$Al_2O_3$ | 19; 4 | 123 | 0.29 |

*XRD*

The pertinent WA XRD results for NiAl_IWI are shown in Fig. 4.34, where the diffractogram of the commercial $\gamma$-$Al_2O_3$ (PDF card 29-0063) support is also reported. The typical reflections of the NiO phase are clearly observable in the pattern of NiAl_IWI, for which an average crystallite size of 19 nm has been calculated (Tab. 4.9). This value is similar to that found for $1.0NiCe\_HT_{IWI}$ and $1.0NiCe\_ST_{IWI}$ catalyst (23 and 20 nm, respectively), suggesting that the NiO dispersion mainly depends on the preparation method rather than by the nature of the support.
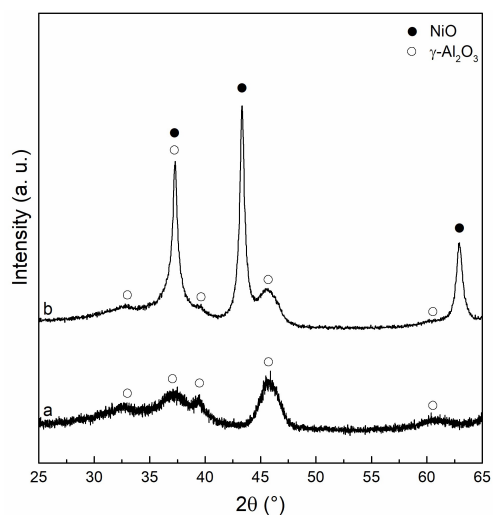
**Fig. 4.35.** Wide angle XRD patterns of commercial $\gamma$-Al$_2$O$_3$ (a) and NiAl_IWI (b).

## *N₂ adsorption/desorption*

The physisorption results of NiAl_IWI is reported in Fig. 4.36. The NiAl_IWI catalyst as well as the pure $\gamma$-Al$_2$O$_3$ support exhibit a type IVa isotherm, and PSD curves which shows a quite narrow peak centred at about 8 nm. It is worth noting that a decrease in surface area of about 35 % is observed as consequence of the impregnation procedure; this value is quite similar to the surface area reduction observed in the case of 1.0NiCe_HT$_{IWI}$ and 1.0NiCe_ST$_{IWI}$ (33 and 36 %, respectively), confirming that, the Ni content being equal, the dispersion of NiO depends exclusively on the method used for the synthesis.
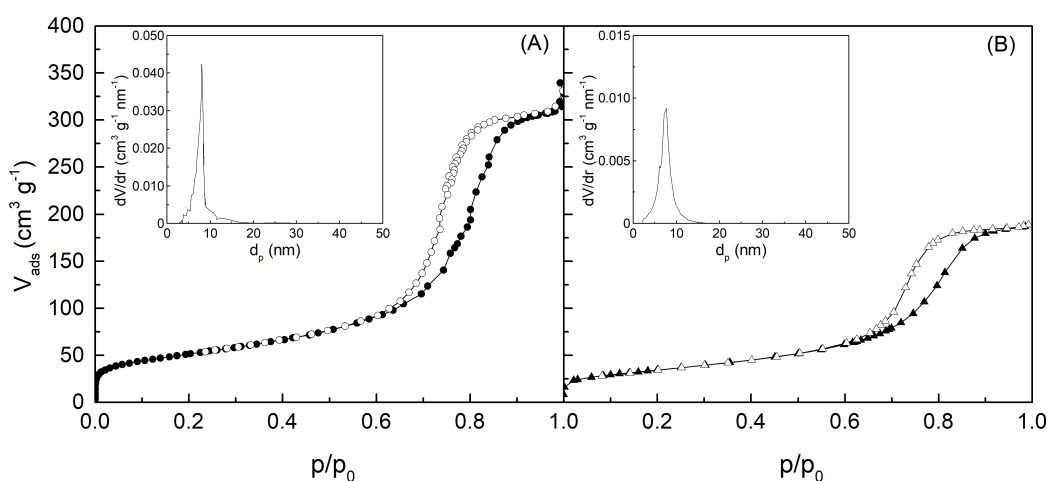


**Fig. 4.36.** N$_2$ physisorption isotherms and pore size distribution (inset) of (A) $\gamma$-Al$_2$O$_3$ and (B) NiAl_IWI.

### 4.4.1.2. H₂-TPR

TPR profile of NiAl_IWI (Fig. 4.37) shows the presence of two distinct peaks centred at 335 and 550 °C, respectively, and also the presence of a shoulder at temperature above 750 °C. According to [60,61], three main types of reducible NiO species can be identified on alumina-supported Ni catalysts: α-, β-, and γ-types. Free nickel oxide species with no or weak interactions with the support (α$_1$- and α$_2$-type species) are responsible for peaks located at lower temperatures (below 500 °C), while mild-temperature peaks (500-740 °C) are originated by the reduction of β$_1$- and β$_2$-type species (with stronger nickel oxide-alumina interactions), which would correspond to reducible NiO in Ni-rich and Al-rich mixed phases, respectively [[60,61]. Thus, the peak at 335 °C in the TPR profile of NiAl_IWI can be reasonably ascribed to α-type NiO, while the peak centred at 550 °C is instead indicative of the presence of β-type NiO species. A comparison between the TPR profiles of NiAl_IWI, 1.0NiCe_HT$_{IWI}$, and 1.0NiCe_ST$_{IWI}$ (Figs. 4.37, 4.12, and 4.25, respectively), clearly indicate that, respect to ceria, alumina is not able to effectively promote the reduction of NiO, making needed more severe pretreatment conditions.
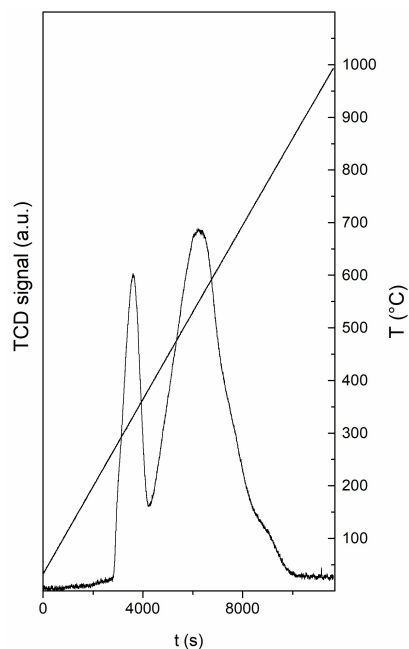


**Fig. 4.37.** H₂-TPR profile of NiAl_IWI.

## 4.4.2. Structural characterisation after H₂ pretreatment at 400 °C for 1 h

WA XRD results of the NiAl_IWI catalyst submitted to the H₂ pretreatment at 400 °C are shown in Fig. 4.38. Besides signals attributable to the γ-Al₂O₃ support, peaks typical of the $Ni^0$ phases and unreduced NiO are clearly visible in the XRD pattern, confirming that the complete reduction of nickel oxide can be only obtained at temperature above 400 °C.
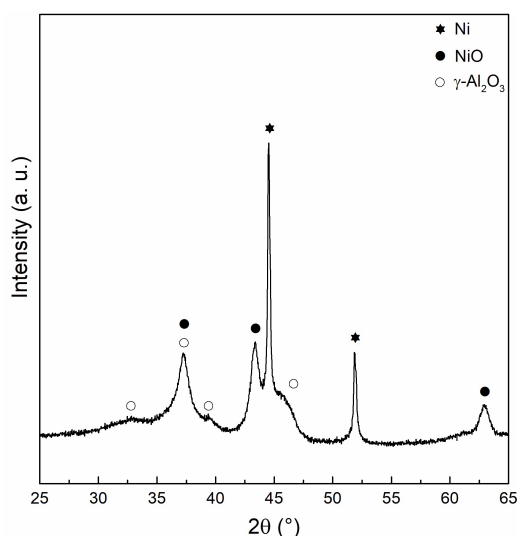


**Fig. 4.38.** Wide angle XRD patterns of reduced NiAl_IWI.

In addition, a marked increase in the size of $Ni^0$ nanocrystals (46 nm) in comparison with that of the original NiO crystallites (19 nm) is observed, in contrast with the more limited growth for the 1.0NiCe_HT$_{IWI}$ and 1.0NiCe_ST$_{IWI}$ catalysts (from 23 and 20 nm to 34 and 34 nm, respectively). This results clearly show that ceria, compared with alumina, is more efficient in preventing sintering phenomena, thus guaranteeing a higher $Ni^0$ dispersion.

## 4.4.3. Catalytic results

### 4.4.3.1. Comparison of the catalytic performance of NiAl_IWI and 1.5NiCe catalysts

CO₂ conversion for the NiAl_IWI, 1.0NiCe_HT$_{IWI}$, and 1.0NiCe_ST$_{IWI}$ catalysts are reported in Fig. 4.39. The results are referred to catalytic tests performed at 300 °C and

atmospheric pressure, by using $0.050$ g of catalyst and a $H_2/CO_2$ molar ratio equal to $4.3$ mol mol$^{-1}$ (space velocity, SV = $72000$ cm$^3$ h$^{-1}$ g$_{cat}^{-1}$). As well as for $1.0NiCe\_HT_{IWI}$ and $1.0NiCe\_ST_{IWI}$, also NiAl\_IWI was found to be stable within 6 h on stream and shows a $CH_4$ selectivity very close to 100 mol%.
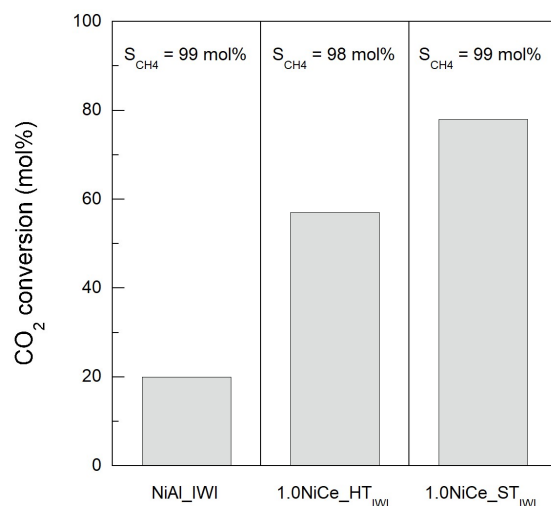


**Fig. 4.39.** $CO_2$ conversion for the NiAl\_IWI, $1.0NiCe\_HT_{IWI}$, and $NiCe\_ST_{IWI}$ after $H_2$ pretreatment at 400 °C.

Compared to $1.0NiCe\_HT_{IWI}$ and $1.0NiCe\_ST_{IWI}$, NiAl\_IWI exhibits a significant lower conversion (20 mol%), demonstrating that $CeO_2$ promotes the catalytic activity of Ni-based catalysts better than $\gamma$-$Al_2O_3$. In addition, since in the previous paragraphs the key role of $CeO_2$ in the activation of $CO_2$ was discussed, a temperature programmed desorption (TPD) run on $\gamma$-$Al_2O_3$ was also performed. A comparison between the amounts of adsorbed $CO_2$, calculated for $\gamma$-$Al_2O_3$ ($0.04 \times 10^{-2}$ mmol$_{CO2}$ g$_{cat}^{-1}$) and for $CeO_2\_HT$ ($6.8 \times 10^{-2}$ mmol$_{CO2}$ g$_{cat}^{-1}$), manifestly indicates that a remarkable lower concentration of basic sites able to activate $CO_2$ is present when alumina is used as the support.

### 4.4.4. Conclusions

In view of the above, and also by considering the TPR and XRD results, the high catalytic activity of the NiCe catalysts with respect to NiAl\_IWI can be reasonably ascribed to the capacity of $CeO_2$ in promoting the reducibility of NiO and assuring a better dispersion of $Ni^0$ after the reduction pretreatment, as well as in providing a higher concentration of basic sites which are responsible for carbon dioxide adsorption and activation.

## References

[1] J. Gao, Y. Wang, Y. Ping, D. Hu, G. Xu, F. Gu, F. Su, *RSC Adv*. 2 (2012) 2358.

[2] X. Su, J. Xu, B. Liang, H. Duan, B. Hou, Y. Huang, *J. Energy Chem.* 25 (2016) 553.

[3] S. Ronsch, J. Schneider, S. Matthischke, M. Schluter, M. Gotz, J. Lefebre, P. Prabhakaran, S. Bajohr, *Fuel* 166 (2016) 276.

[4] P. Frontera, A. Macario, M. Ferraro, P. Antonucci, *Catalyts* 7 (2017) 59.

[5] M.A.A. Aziz, A.A. Jalil, S. Triwahyono, A. Ahmada, *Green Chem.* 17 (2015) 2647.

[6] W. Wang, J. Gong, *Front. Chem. Sci. Eng.* 5 (2011) 2.

[7] J.B Powell, S.H. Langer, *J. Catal*. 94 (1985) 566.

[8] D. C. Upham, A. R. Derk, S. Sharma, H. Metiu, E. W. McFarland, *Catal. Sci. Technol.* 5 (2015) 1783.

[9] Z. Kowalczyk, K. Stołecki, W. Raròg-Pilecka, E. Miskiewicz, E. Wilczkowska, Z. Karpinski, *Appl. Catal. A Gen.* 342 (2008) 35.

[10] T. Li, S. Wang, D. Gao, S. Wang, *J. Fuel Chem. Technol.* 42 (2014) 1440.

[11] S. Tada, O.J. Ochienga, R. Kikuchi, T. Haneda, H. Kameyama, *Int. J. Hydrogen Energy* 39 (2014) 10090.

[12] S. Sharma, Z. Hu, P. Zhang, E. W. McFarland and H. Metiu, *J. Catal.* 278 (2011) 297.

[13] A. Beuls, C. Swalus, M. Jacquemin, G. Heyen, A. Karelovic and P. Ruiz, *Appl. Catal. B: Environ* 113-114 (2012) 2.

[14] A. Karelovic and P. Ruiz, *Appl. Catal. B: Environ* 113- 114 (2012) 237.

[15] C. Swalus, M. Jacquemin, C. Poleunis, P. Bertrand and P. Ruiz, *Appl. Catal. B: Environ.* 125 (2012) 41.

[16]    S. Ma, W. Song, B. Liu, H. Zheng, J. Deng, W. Zhong, J. Liu, X.Q. Gong, Z. Zhao*, Catal. Sci. Technol.* 6 (2016) 6128.

[17]    J. H. Kwak, L. Kovarik and J. Szanyi, *ACS Catal.* 3 (2013) 2094.

[18]    S. Rahmani, M. Rezaei, F. Meshkania, *J. Ind. Eng. Chem.* 20 (2014) 1346.

[19]    L. He, Q. Lin, Y. Liu, Y. Huang, Y. *J. Energy Chem*. 23 (2014) 587.

[20]    S. Rahmani, M. Rezaei, F. Meshkani, *J. Ind. Eng. Chem.* 20 (2014) 4176.

[21]    M. A. A. Aziz, A. A. Jalil, S. Triwahyono, R. R. Mukti, Y. H. Taufiq-Yap, M. R. Sazegar, *Appl. Catal. B: Environ.* 147 (2014) 359.

[22]    M.A.A. Aziz, A.A. Jalil, A.A.; S. Triwahyono, M.W.A. Saad, *Chem. Eng. J.* 260 (2015) 757.

[23]    F. Wang, M. Wei, D.G. Evans, X. Duan, *J. Mater. Chem. A* 4 (2016) 5773.

[24]    P.A. Ussa Aldana, F. Ocampo, K. kobl, B. Louis, F. Thibault-Starzyk, M. Daturi, P. Bazin, S. Thomas, A.C. Roger, *Catal. Today* 215 (2013) 201.

[25]    F. Rouquerol, J. Rouquerol, K. Sing, P. Llewellyn, G. Maurin, *Adsorption by Powders and Porous Solids, Principles, Methodology and Applications*, Second Edition, Academic Press (2014) Amsterdam.

[26]    Y. Wang, J. Ren, Y. Wang, F. Zhang, X. Liu, Y. Guo, *J. Phys. Chem. C* 112 (2008) 15293.

[27]    M.M. Nair, F. Kleitz, S. Kaliaguine, *ChemCatChem* 4 (2012) 387.

[28]    Y. G. Wang, Y. Y. Xia*, Electrochim. Acta* 51 (2006) 3223.

[29]    Y. Wang, Y. Wang, J. Ren, Y. Mi, F. Zhang, C. Li, X. Liu, Y. Guo, G. Lu, *J. Solid State Chem.* 183 (2010) 277.

[30]    P. Boizumault Moriceau, A. Pennequin, B. Grzybowsaka, Y. Barbaux, *Apll. Catal A: Gen.* 245 (2003) 55.

[31]    N. Yisup, Y. Cao, W. L. Feng, W. L. Dai, K. N. Fan, *Catal. Lett.* 99 (2005) 207.

[32]    Y. M. Liu, L. C. Wang, M. Chen, J. Xu, Y. Cao, H. Y. He, K. N. Fan, *Catal. Lett.* 130 (2009) 350.

[33]    W.H. Weber, K.C. Bass, J.R. McBride, *Phys. Rev. B* 48 (1993) 178.

[34]    J.E. Spanier, R.D. Robinson, F. Zheng, S.W. Chan, I.P. Herman, *Phys. Rev. B* 64 (2001) 245407.

[35]    T. Taniguchi, T. Watanabe, N. Sugiyama, A.K. Subramani, H. Wagata, N. Matsushita, M. Yoshimura, *J. Phys. Chem. C*, 113 (2009) 19789.

[36]    A. Nakajima, A. Yoshihara, M. Ishigame, *Phys. Rev. B* 50 (1994) 13297.

[37]    Z. Wu, M. Li, J. Howe, H.M. Meyer III, S.H. Overbury, *Langmuir* 26 (2010) 16595.

[38]    N. Mironova, A. Kuzmin, I. Steins, J. Grabis, I. Sildos, M. Pärs, *J. Phys. Conf. Ser.* 93 (2007) 012039.

[39]    G.R. Rao, *Bull. Mater. Sci*. 22 (1999) 89.

[40]    Y. Wei, H. Wang, K. Li, X. Zhu, Y. Du*, J. Rare Earths* 28 (2010) 357.

[41]    T.V. Sagar, N. Sreelatha, G. Hanmant, M. Surendar, N. Lingaiah, K.S. Rama Rao, C.V.V Satyanarayana, I.A.K. Reddy, P.S. Sai Prasad, *RSC Adv* 4 (2014) 50226.

[42]    B. Nematollahi, M. Rezaei, E. Nemati Lay, *Int. J. Hydrogen Energy* 40 (2015) 8539.

[43]    Y. Li, B. Zhang, X. Tang, Y. Xu, W. Shen, *Catal. Commun*. 7 (2006) 380.

[44]    F. Ocampo, B. Louis, A. C. Roger, *Appl. Catal. A: Gen.* 369 (2009) 90.

[45]    F. Ocampo, B. Louis, A. Kiennemann, A.C. Roger, *IOP Conf. Ser. Mater. Sci. Eng.* 19 (2011) 012007.

[46]    G. Zhou, H. Liu, K. Cui, A. Jia, G. Hu, Z. Jiao, Y. Liu, X. Zhang, *Appl. Surf. Sci.* 383 (2016) 248.

[47]    J. Ashok, M.L. Ang, S. Kawi, *Catal. Today* 281 (2017) 304.

[48]    Q. Pan, J. Peng, T. Sun, S. Wang, S. Wang, *Catal. Commun.* 45 (2014) 74.

[49]    L.G. Appel, J.G. Eon, M. Schmal, *Catal. Lett.* 56 (1998) 199.

[50]    M. Daturi, C. Binet, J.C. Lavalley, H. Vidal, J. Kaspar, M. Graziani, G. Blanchard, *J. Phys. Chem.* 95 (1998) 2048.

[51]    P. Kumar, P. With, V.C. Srivastava, K. Shuka, R. Gläser, I.M. Mishra, *RSC Adv* 6 (2016) 110235.

[52]    M. Nizio, A. Albarazi, S. Cavadias, J. Amouroux, M.E. Galvez, P. Da Costa, *Int. J. Hydrogen Energy* 41 (2016) 11584.

[53]    G. Garbarino, P. Riani, L. Magistri, G. Busca, *Int. J. Hydrogen Energy* 39 (2014) 11557.

[54]    Y.-J. Wang, J.-M. Ma, M.-F. Luo, P. Fang, M. He, *J. Rare Earths* 25 (2007) 58.

[55]    M.-F. Luo, J.-M. Ma, J.-Q. Lu, Y.-P. Song, Y.-J. Wang, *J. Catal.* 246 (2007) 52.

[56]    Z. Liu, B. Chu, X. Zhai, Y. Jin, Y. Cheng, *Fuel* 95 (2012) 599.

[57]    P. Riani, G. Garbarino, M.A. Lucchini, F. Canepa, G. Busca, *J. Mol. Catal. A: Chem.* 383 (2014) 10.

[58]    L.E.A. Berlouis, C. Jubin, B.G. McMillan, J. Morrow, M.D. Spicer, L.P. Tang, O. Bordelanne, M. Weston, *Phys. Chem. Chem. Phys.* 9 (2007) 6032.

[59]    M. Cargnello, V.V.T. Doan-Nguyen, T.R. Gordon, R.E. Diaz, E.A. Stach, R.J. Gorte, P. Fornasiero, C.B. Murray, *Science* 341 (2013) 771.

[60]    D. Hu, J. Gao, Y. Ping, L. Jia, P. Gunawan, Z. Zhong, G. Xu, F. Gu, F. Su, *Ind. Eng. Chem. Res.* 51 (2012) 4875.

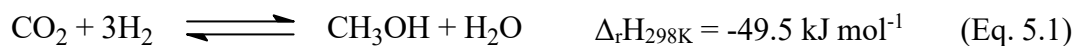[61]    A. Alihosseinzadeh, B. Nematollahi, M. Rezai, E.N. Lay, *Int. J. Hydrogen Energy* 40 (2015) 1809.

# Chapter V

# *CO$_2$ conversion to methanol*

## 5.1. Introduction

CO₂ chemical recycling to methanol is attracting growing attention from the scientific community as it probably represents the best option to meet the requirements for a sustainable future. The concept of "*Methanol Economy*", proposed by the Nobel Laureate George Olah, underlines how exploiting carbon dioxide to produce methanol through sustainable reduction routes will help to reduce $CO_2$ emissions while preserving natural sources, such as oil, natural gas, and coal, for the future generations. This prominent role of methanol for an economically and environmentally sustainable future is mainly related to the importance that, through the $CO_2$ catalytic conversion, it can cover in the energetic sector (cf. 1.3.3); indeed, methanol is able to be used directly as a fuel for internal combustion engines or as the intermediate for the production of DME (more suitable to be used in diesel engines) and of hydrocarbons by *Methanol to Gasoline* processes [1,2].

The main reactions involved in the methanol production by $CO_2$ hydrogenation are the direct reduction of carbon dioxide to methanol (Eq. 5.1) and the reverse water gas shift (RWGS), through which CO and $H_2O$ are formed (Eq. 5.2).

$$CO_2 + 3H_2 \rightleftharpoons CH_3OH + H_2O \qquad \Delta_r H_{298K} = -49.5 \text{ kJ mol}^{-1} \qquad \text{(Eq. 5.1)}$$

$$CO_2 + H_2 \rightleftharpoons CO + H_2O \qquad \Delta_r H_{298K} = +41.2 \text{ kJ mol}^{-1} \qquad \text{(Eq. 5.2)}$$

The $CO_2$ conversion to methanol is an exothermic reaction that takes place with a decrease in the number of moles, thus making the process favoured by low temperature and high pressure.

Currently, methanol is produced from syngas by using Cu/ZnO-based catalysts, at 250-300 °C and pressures ranging from 50 to 100 bar. In this process, a $CO_2$ concentration up to 30% of the total carbon content has been found to be critical to get high yields, since $CO_2$, rather than CO, is considered as the main carbon source for methanol production. [3-5]. As a matter of fact, it has been reported that CO can lead to the formation of methanol only through its preliminary reaction with water to give $CO_2$ and $H_2$ (Water Gas Shift reaction), which in turn can react to produce additional methanol [6,7]. On the other hand, a higher $CO_2$ concentration can be responsible for a detrimental effect on the process performance, since the

large amount of water, produced both through the main hydrogenation reaction to methanol and the Reverse Water Gas Shift, is able to promote the sintering of the main active phases, resulting in a loss of catalytic activity.

Thus, though methanol synthesis through $CO_2$ hydrogenation is becoming a technologically mature process, several advancements are still needed, mostly in the development of efficient catalysts able to guarantee high methanol selectivity and poor tendency to deactivation. Although several interesting studies have been recently reported on the use of Pd as the main active component [8], Cu-based mixed oxides still remain the best option as efficient catalysts for the methanol synthesis.

## 5.1.1. Cu-based catalysts

Just like in the industrial process from syngas, Cu/ZnO-based mixed oxides are the most studied catalysts for converting $CO_2$ into methanol, due to their relatively high activity and $CH_3OH$ selectivity.

A huge number of studies have been carried out to investigate the nature and the role of the Cu and ZnO sites in the reaction mechanism, but some controversies still remain open [8,9]. Nevertheless, it is a consolidated fact that the synergy between Cu and ZnO is crucial to promote reactants activation and to guarantee high catalytic performance, since there are clear evidences that the activity of the binary catalysts is remarkably higher than that obtained using only Cu or ZnO [10,11]. Both $Cu^0$ and $Cu^+$ species have been reported as active sites for $CO_2$ hydrogenation to methanol. Some papers have indicated metallic copper atoms as the main active sites, since catalytic activity was found to strictly depend on the $Cu^0$ surface area [12-14]. Other authors have instead reported that $Cu^+$ species are the only ones responsible for the activity, the addition of promoters, such as ZnO and elements of the IA group, being particularly beneficial thanks to their ability of increasing $Cu^+$ concentration [10,15-17]. ZnO has been reported to play the dual role of active species and promoter in the Cu/ZnO-based catalysts, since its structure is characterised by the presence of oxygen vacancies, which can actively participate to the activation of carbon dioxide and hydrogen [9,18]. The presence of ZnO in the Cu-based catalysts has also been found to promote the dispersion of the Cu particles, limiting the sintering phenomena which can be considered as the main cause of catalyst deactivation. In addition, ZnO has been proved to be particularly useful in the presence of poisoning species

such as $H_2S$, since it is able to form zinc sulphide through a thermodynamically favoured reaction [19]. The synergistic effect between Cu and ZnO in two-component Cu/ZnO systems has been proposed to promote the activation of $CO_2$ and $H_2$ and to induce the spill-over of activated -H species between the different activation sites, favouring methanol formation by promoting hydrogenation of the reaction intermediates [20,21].

Despite the numerous studies carried out in the last decades dealing with the understanding of the reaction mechanism, the thorough description of the reaction pathway still remains a matter of active debate. Most researchers agree to consider the formate intermediate (HCOO*) as the first hydrogenated species formed through the synergistic cooperation between the Cu and ZnO active sites, which in turn leads to the formation of $CH_3O^*$ and finally of methanol through subsequent hydrogenation steps [18,22,23]. In $CO_2$ hydrogenation, formate species are considered to play a key-role both in $CH_3OH$ and CO formation (cf. Eqs 5.1 and 5.2), where monodentate and bidentate intermediates are involved in the direct synthesis of methanol and RWGS, respectively [18]. However, some uncertainties persist in establishing the complete reaction scheme and the limiting-rate steps, which is why further studies would be needed.

Currently, the main drawbacks in the use of classical Cu/ZnO catalysts for $CO_2$ conversion to methanol remain related to the large amount of water produced in both methanol synthesis and RWGS reaction. In fact, water generally has a detrimental effect on the catalysts, since it favours both Cu and ZnO crystallization, leading to their sintering and thus to catalyst deactivation [5,24].

In view of the above, it is clear that, in order to make methanol production from $CO_2$ more competitive than the classical route from syngas, catalysts formulation needs to be further improved to increase the stability of the active components as well as the activity at lower temperatures.

In this regard, several researchers have focused their attention on the use of different supports and promoters, as well as on the effect of different preparation methods. Alumina is probably the most used support for Cu/ZnO based catalysts, as it enhances both the thermal and chemical stability of the main active components. $Al_2O_3$ can also be considered as a promoter, since its presence can favour the dispersion of the active phases and allow both the enrichment and stabilization of $Cu^+$ species during the reduction and reaction processes [9]. A huge number of papers have been published dealing with the preparation of $Cu/ZnO/Al_2O_3$ ternary materials.

Since the catalytic performance strictly depends on the dispersion and interaction of the components, several synthesis methods have been proposed for their preparation. Among these, the coprecipitation method results the most used, with the final catalyst properties depending on the choice of the oxide precursors and precipitation conditions [8]. In particular, the appropriate adjustment of pH, temperature, and aging time have been reported as critical parameters to get ternary materials with high catalytic performance [25,26]. The assistance of microwave irradiation during precipitation and aging steps was also reported to effectively enhance the catalyst activity and stability [27]. Cu/Zn/Al hydrotalcites obtained through coprecipitation methods were reported as suitable precursors for copper-based catalysts, since the versatility in introducing different cation species in the layered structure of the hydrotalcite precursor permits to achieve high dispersion and stability of the active components [28,29]. Generally, coprecipitation methods are performed starting from nitrate precursors and Na-based precipitating agents, whose incomplete removal before the calcination step can favour the sintering of the active phases, with detrimental effects on the catalytic performance. In this light, an accurate washing step before calcination as well as the use of Na-free precipitating agents were reported to be advantageous [30,31].

Besides $Al_2O_3$, $ZrO_2$ has been extensively studied as a support for Cu/ZnO based catalysts, because of its high stability under reducing or oxidizing atmosphere, and the lower hydrophilicity with respect to alumina [8,9]. In addition, the presence of $ZrO_2$ enhances the Cu dispersion and stability, due to the establishment of strong metal-support interactions, and can also have a positive effect in the methanol production thanks to its ability to promote the $CO_2$ activation at the $Cu/ZrO_2$ interface [32,33]. Controversies exist on the influence of the crystallographic structure of zirconia on catalytic activity, with both tetragonal and amorphous phases being reported to improve catalytic performance [34,35]. There are several papers relating to the preparation of ternary Cu/Zn/Zr materials by coprecipitation, which show the importance of aging time in the fine-tuning of the catalysts properties [36,37]. A very good catalytic behaviour was shown by $Cu/ZnO/ZrO_2$ materials prepared through a surfactant-assisted coprecipitation procedure, thanks to which effective Cu-Zn and Cu-Zr interactions were obtained [38].

In addition to those just discussed, other promoters and supports have been investigated in the recent past. Among them, $CeO_2$ has attracted the interest of researchers due to its beneficial role in different $CO_2$ conversion processes [39]. In this regard, Graciani *et al*. have

shown that Cu/CeO$_2$ catalysts have a very promising catalytic activity; the authors also reported evidence of a reaction mechanism involving OCOH species rather than formate species as intermediates [40].

## 5.1.2. Future perspectives and work purpose

To develop highly active and highly stable Cu-based catalysts, besides a better understanding of the nature of active sites and of the reaction mechanism, the use of unconventional synthesis procedures, appropriately designed to maximize surface area, Cu dispersion and Cu-promoters interactions, have to be the key points for future research.

For this purpose, two different series of Cu-based catalysts were prepared and used for converting CO$_2$ into methanol. The first series was prepared by the "*via-hydrotalcites*" method, while the second one was obtained by means of the "*Soft-Template*" strategy. In both cases, the chemical composition of the catalysts was opportunely modified for a preliminary investigation of the influence of different promoters and supports, such as ZnO, Al$_2$O$_3$, ZrO$_2$, and CeO$_2$, on the catalytic behaviour. A comparison of the catalytic activity of the synthesized samples with that of a commercial Cu-based catalyst was also performed. The obtained preliminary results are discussed in the following.

## 5.2. Results and discussion

### 5.2.1. Characterisation of $z$CuO/$y$ZnO/$w$Al$_2$O$_3$/$v$ZrO$_2$/$u$CeO$_2$ from hydrotalcites

#### 5.2.1.1. Structural characterisation of hydrotalcitic precursors

In Fig. 5.1, the XRD results for the $z$Cu/$y$Zn/$w$Al/$v$Zr/$u$Ce hydrotalcites are reported. All the patterns show the presence of the typical peaks ascribable to the hydrotalcite-like phase [28,29], indicating that the materials were successfully prepared. However, a decrease in intensity of the signals is observed as a result of the partial substitution of Al$^{3+}$ with the Zr$^{4+}$ and Ce$^{3+}$ cations (patterns b,c, and d). According to the literature [41], this evidence points out that the introduction of cations with different oxidation state and ionic radius with respect to Al$^{3+}$ causes some distortion in the layer structure, thus affecting the crystallinity of the

hydrotalcite. A careful analysis of the patterns also shows that peaks with very low intensity at 2θ values of 35.5° and 38.7°, ascribable to the CuO phase (PDF 80-1917), are present for all the samples, highlighting the partial segregation of copper as oxide particles. In addition, very broad signals with low intensity indicative of the presence of the CeO₂ phase (PDF card 81-0792) can also be observed in the case of the 2Cu/1Zn/0.7Al/0.3Ce and 2Cu/1Zn/0.7Al/0.15Ce/0.15Zr hydrotalcites (patterns c and d), which seems to suggest the incomplete incorporation of Ce in the layered structure.
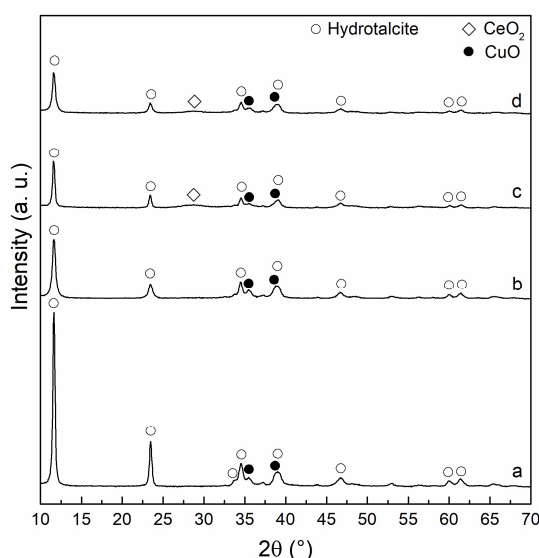


**Fig. 5.1.** XRD patterns of the Cu-based hydrotalcites: 2Cu/1Zn/1Al (a); 2Cu/1Zn/0.7Al/0.3Zr (b); 2Cu/1Zn/0.7Al/0.3Ce (c); 2Cu/1Zn/0.7Al/0.15Zr/0.15Ce (d).

### 5.2.1.2. Chemical composition, structural and textural characterisation

The chemical composition of the $z$Cu/$y$Zn/$w$Al/$v$Zr/$u$Ce_Htl mixed oxides, obtained by calcination at 500°C of the hydrotalcites precursors, is reported in Tab. 5.1. It can be noted that the experimental values are in good agreement with the theoretical ones for all the samples, pointing out the efficiency of the "*via-hydrotalcites*" synthesis procedure.

**Tab. 5.1.** Chemical composition of the *z*Cu/*y*Zn/*w*Al/*v*Zr/*u*Ce catalysts.

| Sample | Molar composition |
|---|---|
| 2Cu/1Zn/1Al_Htl | 2Cu/0.94Zn/0.92Al |
| 2Cu/1Zn/0.7Al/0.3Zr_Htl | 2Cu/1.02Zn/0.84Al/0.25Zr |
| 2Cu/1Zn/0.7Al/0.3Ce_Htl | 2Cu/1.01Zn/0.77Al/0.31Ce |
| 2Cu/1Zn/0.7Al/0.15Zr/0.15Ce_Htl | 2Cu/1.02Zn/0.78Al/0.13Zr/0.17Ce |

The structural and textural properties of the *z*Cu/*y*Zn/*w*Al/*v*Zr/*u*Ce_Htl mixed oxides catalysts are summarized in Tab. 5.2 and shown in Figs. 5.2 and 5.3, respectively.

**Tab. 5.2.** Structural and textural features of the *z*Cu/*y*Zn/*w*Al/*v*Zr/*u*Ce catalysts.

| Sample | Crystal phases | Crystal size $D_c$ (nm) | $S_{BET}$ ($m^2\ g^{-1}$) | $V_p$ ($cm^3\ g^{-1}$) |
|---|---|---|---|---|
| 2Cu/1Zn/1Al_Htl | CuO; ZnO | 11; [a]n.d. | 42 | 0.18 |
| 2Cu/1Zn/0.7Al/0.3Zr_Htl | CuO; ZnO | 11; [a]n.d. | 64 | 0.38 |
| 2Cu/1Zn/0.7Al/0.3Ce_Htl | CuO; CeO₂ | 11; [a]n.d. | 49 | 0.39 |
| 2Cu/1Zn/0.7Al/0.15Zr/0.15Ce_Htl | CuO; CeO₂ | 11; [a]n.d. | 66 | 0.41 |

[a]n.d.: not determined.

## *XRD*

The diffraction patterns of all the *z*Cu/*y*Zn/*w*Al/*v*Zr/*u*Ce_Htl (Fig. 5.2) show the typical signals ascribable to the CuO phase, for which a mean crystallites size of 11 nm has been estimated (Tab. 5.2). In addition, peaks with very low intensity associated to the presence of the ZnO phase (PDF card 75-0576) can be observed for all the patterns, even though not clearly defined due to the superimposition with the more evident ones of CuO. By comparing the peaks of CuO and ZnO, clearly emerges the poorer dispersion of CuO, in agreement with the presence of segregated copper oxide observed for the hydrotalcite precursors. For all the prepared samples, no peaks associated with the presence of $Al_2O_3$ phases are visible, probably due to its predominant amorphous character; the absence of peaks ascribable to the $ZrO_2$ phase in the 2Cu/1Zn/0.7Al/0.3Zr_Htl and 2Cu/1Zn/0.7Al/0.15Zr/0.15Ce_Htl catalysts can be justified accordingly (patterns b and d). By converse, in the case of the 2Cu/1Zn/0.7Al/0.3Ce_Htl and

2Cu/1Zn/0.7Al/0.15Zr/0.15Ce_Htl catalysts (patterns c and d) broad signals associated with the presence of $CeO_2$ are visible, suggesting a higher crystallinity degree with respect to $Al_2O_3$ and $ZrO_2$.
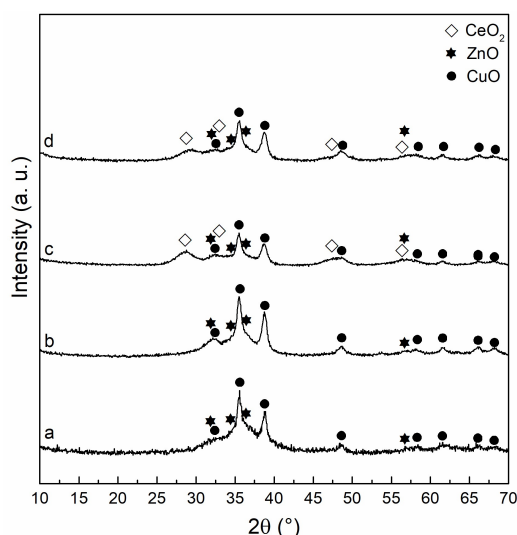


**Fig. 5.2.** XRD patterns of the *z*Cu/*y*Zn/*w*Al/*v*Zr/*u*Ce_Htl catalysts: 2Cu/1Zn/1Al_Htl (a); 2Cu/1Zn/0.7Al/0.3Zr_Htl (b); 2Cu/1Zn/0.7Al/0.3Ce_Htl (c); 2Cu/1Zn/0.7Al/0.15Zr/0.15Ce_Htl (d).

*N₂ adsorption/desorption*

N₂ physisorption results for all the samples are reported in Fig. 5.3. According to [42], all physisorption curves can be classified as type IIb adsorption/desorption isotherms; the presence of the narrow hysteresis loop (type H₃) can be associated with interparticle capillary condensation due to the presence of plate-shaped particles. The surface area values (S$_{BET}$) are in the range 44-66 m$^2$ g$^{-1}$ (Tab. 5.2) and reveal that the presence of Zr in substitution of Al positively affects the surface development of the materials. All the catalysts show a bimodal pore size distribution, with a narrow contribution for diameters below 5 nm and a very large one centred at about 34 nm.
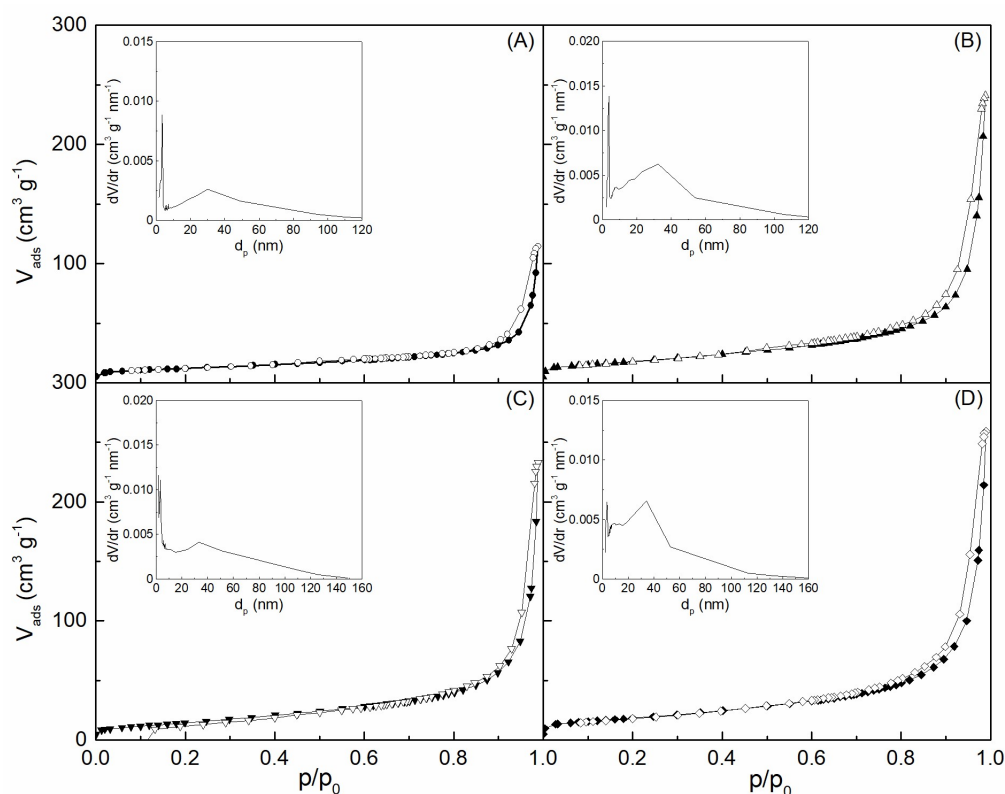
**Fig. 5.3.** $N_2$ adsorption/desorption isotherms and pore size distribution (inset) of the $z$Cu/$y$Zn/$w$Al/$v$Zr/$u$Ce_Htl catalysts:  (A) 2Cu/1Zn/1Al_Htl;  (B) 2Cu/1Zn/0.7Al/0.3Zr_Htl;  (C) 2Cu/1Zn/0.7Al/0.3Ce_Htl; (D) 2Cu/1Zn/0.7Al/0.15Zr/0.15Ce_Htl.

### 5.2.1.3. H₂-TPR

TPR profiles of the $z$Cu/$y$Zn/$w$Al/$v$Zr/$u$Ce_Htl catalysts are presented in Fig. 5.4. All the reduction curves exhibit a broad peak, characterised by the overlapping of distinct contributions, which clearly indicate the presence of different reducible species. Since ZnO, $Al_2O_3$, and $ZrO_2$ have been reported to be not reduced within the temperature range of the TPR analysis (50-400 °C) [43-46], the reducibility of 2Cu/1Zn/1Al_Htl and 2Cu/1Zn/0.7Al/0.3Zr_Htl (Fig. 5.4, profiles a and b) can be ascribed to the sole presence of different CuO species. Conversely, in the case of 2Cu/1Zn/0.7Al/0.3Ce_Htl and 2Cu/1Zn/0.7Al/0.15Zr/0.15Ce_Htl the reduction of $CeO_2$ to some extent cannot be excluded; indeed, though the reduction of pure ceria has been reported to take place at temperature higher than 350 °C (cf. Fig. 4.24), some authors have reported that $CeO_2$ interactions with CuO species can enhance its reducibility at lower temperatures [47,48].
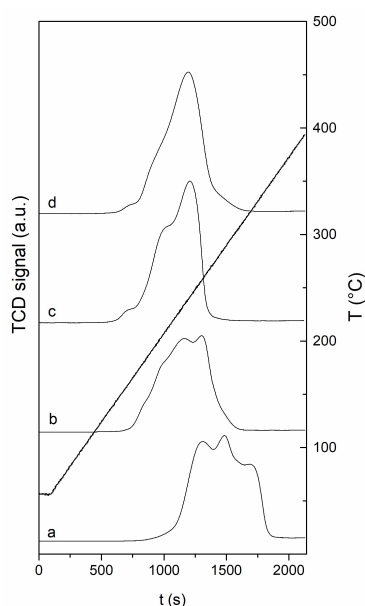
**Fig. 5.4.** TPR profiles of the *z*Cu/*y*Zn/*w*Al/*v*Zr/*u*Ce_Htl catalysts: 2Cu/1Zn/1Al_Htl (a); 2Cu/1Zn/0.7Al/0.3Zr_Htl (b); 2Cu/1Zn/0.7Al/0.3Ce_Htl (c); 2Cu/1Zn/0.7Al/0.15Zr/0.15Ce_Htl (d).

The TPR curve of 2Cu/1Zn/1Al_Htl (Fig. 5.4, curve a) shows a peak in the temperature range of 180-350 °C, which results by the overlapping of three well visible contributions centred at 260, 287, and 323 °C, respectively. According to [49], the highest temperature feature can be ascribed to the reduction of large CuO particles, that comprehensibly require more severe temperature conditions; the low-temperature contributions can instead be reasonably assigned to CuO species with different dispersion degrees, for which the reduction temperature has been reported to rise with the increase in the particles size [50]. Accordingly, the reduction of different CuO species can be proposed to be responsible also for the different contributions observable in the TPR profiles of the other Htl materials, though the profile of 2Cu/1Zn/07Al/0.3Zr_Htl appears more complicated, probably due to a more heterogeneous dispersion of reducible CuO.

Compared to 2Cu/1Zn/1Al_Htl, for all the other Htl catalysts the reduction peaks are shifted towards a lower temperature range (about 140-310 °C), indicating that Al substitution with both Zr and Ce positively affects the reducibility of the CuO phase, in agreement with what reported by other authors [45,48]. Since the estimated mean size of CuO nanoparticles is 11 nm for all the samples (Tab. 5.2), such differences in the reduction temperature range may

be ascribed to the establishment of effective Cu-Zr and Cu-Ce electronic interactions, which promote CuO reducibility, rather than to a different CuO dispersion.

## 5.2.2. Characterisation of *Soft-Templated zCuO/yZnO/uCeO₂*

### 5.2.2.1. Chemical composition, structural and textural characterisation

In Tab. 5.3, the chemical composition and the structural and textural properties of the $z$Cu/$y$Zn/$u$Ce_ST catalysts are reported. Also in this case, the good agreement between the experimental (determined by ICP-AES) and theoretical composition shows that the samples were successfully prepared.

**Tab. 5.3.** Chemical composition, structural properties, and textural features of the $z$Cu/$y$Zn/$u$Ce_ST samples.

| Sample | Molar composition | Crystal phases | Crystal size $D_c$ (nm) | $S_{BET}$ (m² g⁻¹) | $V_p$ (cm³ g⁻¹) |
|---|---|---|---|---|---|
| 2Cu/1Ce_ST | 2Cu/1.1Ce | CuO; Cu₂O, CeO₂ | 22; 17; 4 | 142 | 0.36 |
| 2Cu/1Zn/1Ce_ST | 2Cu/1.2Zn/1.1Ce | CuO; ZnO; CeO₂ | 25; 109; 3 | 66 | 0.11 |

*XRD*

The XRD patterns of the 2Cu/1Ce_ST and 2Cu/1Zn/1Ce_ST catalysts are reported in Fig. 5.5. The typical reflections of the CuO phase are observable for both the samples, for which the estimated average size of CuO crystallites was 22 and 25 nm, respectively. Besides those of CuO, wide peaks ascribable to the CeO₂ phase are also visible, from which a very small mean nanocrystal diameter has been calculated (4-3 nm). In the case of 2Cu/1Ce_ST, the peaks centred at about 36.4° and 42.3° can be ascribed to the presence of the Cu₂O phase, for which a mean nanoparticle size of about 17 nm has been estimated. Interestingly, these signals completely disappear in the case of 2Cu/1Zn/1Ce_ST, suggesting that $Cu^{2+}$ species are stabilised by the presence of ZnO. It is worth to underline that the presence of the sole CuO phase in the case of 2Cu/1Zn/1Ce_ST explains the higher intensity of the corresponding peaks with respect to 2Cu/1Ce_ST, for which, despite the higher Cu content (wt%), also the presence of Cu₂O has been observed. Very narrow signals ascribable to the ZnO phase are observed for

the 2Cu/1Zn/1Ce_ST sample, indicating the existence of large particles of such oxide, for which a mean crystallite size of 109 nm has been estimated. These results highlight that the ST preparation method, while permitting the formation of small CuO and $CeO_2$ nanoparticles, does not seem so effective in ensuring a good dispersion of ZnO, which, as a consequence, may only poorly interact with the other components of the catalyst.
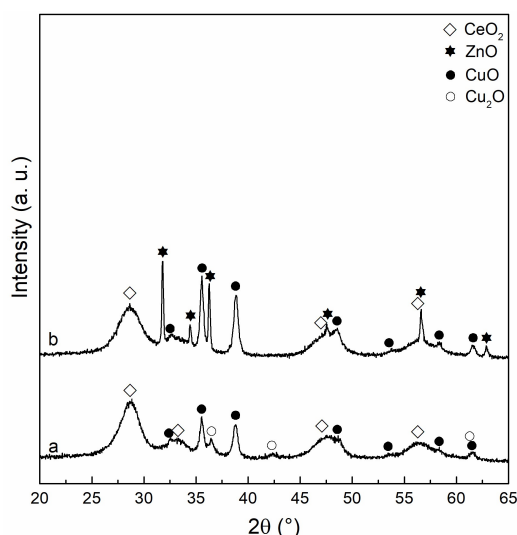


**Fig. 5.5.** XRD patterns of the *z*Cu/*y*Zn/*u*Ce_ST catalysts: 2Cu/1Ce_ST (a); 2Cu/1Zn/1Ce_ST (b).

## *N₂ adsorption/desorption*

N₂ physisorption results of 2Cu/1Ce_ST and 2Cu/1Zn/1Ce_ST samples are reported in Fig. 5.6. For both the samples the curves can be classified as type IVa isotherms, which are typical of mesoporous solids. A comparison between the textural properties of the 2Cu/1Ce_ST and 2Cu/1Zn/1Ce_ST samples (Tab. 5.3), reveals that the presence of ZnO causes a clear decrease in surface area; since the porosity of the ST samples depends on the nanoparticles assembly, such decrease may be explained by considering the larger particle size of ZnO in comparison with those of CuO and $CeO_2$ in the 2Cu/1Ce_ST sample. The 2Cu/1Ce_ST catalyst shows a large pore size distribution, in the range 2-30 nm (Fig. 5.6A, inset), in agreement with the presence of a hysteresis loop which extends up to p/p₀ values close to 1. By converse, in spite of the non-homogeneous distribution of the nanoparticles sizes, which should lead to a worse assembly of the different oxide components, the 2Cu/1Zn/1Ce_ST sample exhibits a narrow pore size distribution curve, centred at about 4 nm.
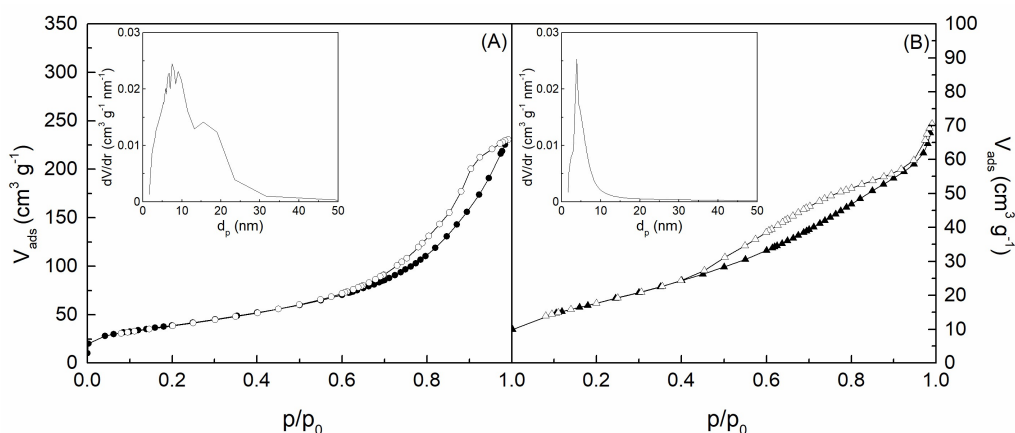
**Fig. 5.6.** N₂ adsorption/desorption isotherms and pore size distribution (inset) of the *z*Cu/*y*Zn/*u*Ce_ST catalysts: (A) 2Cu/1Ce_ST; (B) 2Cu/1Zn/1Ce_ST.

### 5.2.2.2. H₂-TPR

H₂-TPR results for the two Cu-based ST samples are showed in Fig. 5.7. Both the TPR profiles are characterized by a broad reduction peak in the temperature range 175-280 °C and a small contribution at low temperatures (120-175 °C), mainly ascribable to the presence of different CuO reducible species, though the reduction of ceria to some extent cannot be excluded. According to the literature [45], the reduction of pure CuO occurs at temperatures higher than 290 °C. In agreement with other authors [51], the present results suggest that the presence of CeO₂ positively affects the reducibility of the CuO species, confirming what previously observed for the catalysts synthesized by the *"via-hydrotalcites"* method.
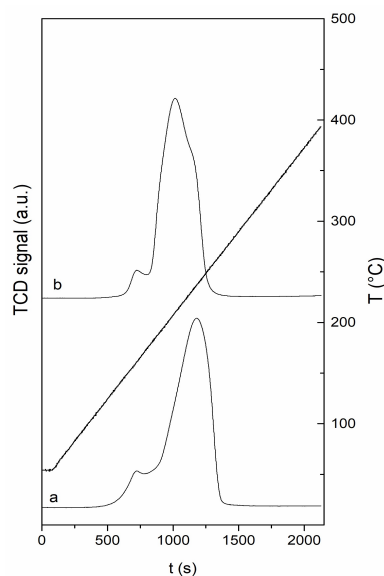


**Fig. 5.7.** TPR profiles of the *z*Cu/*y*Zn/*u*Ce_ST catalysts: 2Cu/1Ce_ST (a); 2Cu/1Zn/1Ce_ST (b).

According to the literature [52], in the case of 2Cu/1Ce_ST (Fig. 5.7, profile a), the low-temperature feature centered at 160 °C can be associated with the reduction of highly dispersed CuO particles, while the contribution at higher temperature (237 °C) can be ascribed to larger CuO particles less interacting with ceria. For the 2Cu/1Zn/1Ce_ST sample (Fig. 5.7, profile b), the main peak is centred at lower temperatures (210 °C) and shows a well identifiable shoulder facing the high temperature region. Interestingly, the shift of the temperature of maximum $H_2$-consumption at lower values for the sample containing ZnO seems to suggest that Cu-Zn interactions strong enough to promote CuO reduction are established, despite the large mean size of the ZnO particles (Tab. 5.3), which hinders the formation of a high CuO/ZnO interface.

## 5.2.3. Catalytic results

Catalytic results for the $z$Cu/$y$Zn/$w$Al/$v$Zr/$u$Ce_HTl and $z$Cu/$y$Zn/$u$Ce_ST samples are summarised in Tab. 5.4. The results obtained by using a commercial Cu-based catalyst (Alfa Aesar), named Cu$_{comm}$, are also reported for comparison. All the catalysts were found to be stable within 48 h on stream. The main reaction products are $CH_3OH$, CO, and $H_2O$, resulting from the direct conversion of $CO_2$ to methanol and the Reverse Water Gas Shift (RWGS) reaction.

**Tab. 5.4.** Catalytic results for the $z$Cu/$y$Zn/$w$Al/$v$Zr/$u$Ce_Htl and $z$Cu/$y$Zn/$u$Ce_ST catalysts. Reaction condition; T = 250 °C; P = 30 bar; $m_{cat}$ = 0.450 g; SV = 44000 cm³ h⁻¹ $g_{cat}$⁻¹; $H_2$/$CO_2$ = 3.0 mol mol⁻¹

| Sample | $CO_2$ conversion (mol%) | $CH_3OH$ selectivity (mol%) | $CH_3OH$ productivity ($mg_{CH3OH}$ h⁻¹ $g_{cat}$⁻¹) |
|---|---|---|---|
| 2Cu/1Zn/1Al_Htl | 8.0 | 34 | 384 |
| 2Cu/1Zn/0.7Al/0.3Zr_Htl | 9.2 | 31 | 404 |
| 2Cu/1Zn/0.7Al/0.3Ce_Htl | 5.2 | 37 | 271 |
| 2Cu/1Zn/0.7Al/0.15Zr/0.15Ce_Htl | 7.7 | 35 | 383 |
| 2Cu/1Ce_ST | 2.5 | 19 | 68 |
| 2Cu/1Zn/1Ce_ST | 1.6 | 47 | 106 |
| Cu$_{comm}$ | 14.8 | 36 | 756 |

The $z$Cu/$y$Zn/$w$Al/$v$Zr/$u$Ce_Htl samples show a promising catalytic performance, though significantly lower conversions in comparison with the commercial catalyst are observed.

2Cu/1Zn/0.7Al/0.3Zr_Htl shows a slightly higher methanol productivity compared to 2Cu/1Zn/1Al_Htl and 2Cu/1Zn/0.7Al/0.15Zr/0.15Ce_Htl, while a remarkable decrease is observed for 2Cu/1Zn/0.7Al/0.3Ce_Htl (Tab. 5.4). By a closer inspection, the results seem to indicate that $CO_2$ conversion and $CH_3OH$ selectivity depend on the presence of Zr and/or Ce. Indeed, it can be seen that the partial substitution of Al with Zr leads to an increase in conversion, which is accompanied by a decrease in $CH_3OH$ selectivity. Conversely, the presence of Ce promotes $CH_3OH$ selectivity at the expense of $CO_2$ conversion. Such effect is particularly evident for the catalyst with the highest Ce content (2Cu/1Zn/0.7Al/0.3Ce_Htl), which shows the worse catalytic performance. These evidences are in accordance with findings reported by other authors [53,54], who ascribed the decrease in $CO_2$ conversion in the presence of ceria to its low efficiency in preserving good textural properties and high Cu dispersion after the reduction pretreatments. On the other hand, the increase in $CH_3OH$ selectivity can be explained by the promoting effect that $CeO_2$ plays in the adsorption and activation of $CO_2$, which leads to an increase in the concentration of formate intermediates at the Cu/promoter interface and therefore to the favourable formation of methanol. In agreement with the literature [53], the obtained results suggest that an appropriate combination between $ZrO_2$ and $CeO_2$ might lead to a synergistic effect through which the achievement of high catalytic performance would be possible.

Compared to both $Cu_{comm}$ and $z$Cu/$y$Zn/$w$Al/$v$Zr/$u$Ce_Htl catalysts, the $z$Cu/$y$Zn/$u$Ce_ST samples show a remarkably poorer catalytic performance. The low conversion values of the ST catalysts (Tab. 5.4) may be explained by the presence of high Ce contents; however, by taking into account the promoting effect of $CeO_2$ on methanol formation, the selectivity value of 19 mol% shown by the 2Cu/1Ce_ST catalyst is somehow surprising. Such result may be explained by the absence of the ZnO phase on this sample, confirming the well-recognised essential role of ZnO in improving the activity of Cu. Interestingly, despite the lower $CO_2$ conversion, the 2Cu/1Zn/1Ce_ST catalyst shows a significantly higher methanol productivity, due to a marked improvement in selectivity (47 mol%), which is even higher than that observed for $Cu_{comm}$ and $z$Cu/$y$Zn/$w$Al/$v$Zr/$u$Ce_Htl catalysts. Unfortunately, the large

particles size of zinc oxide observed on this sample (Tab. 5.3), which limits the Cu-ZnO interactions, is most probably responsible for its low catalytic activity.

## 5.3. Conclusions

Although incomplete, the catalytic results, obtained so far on the *z*Cu/*y*Zn/*w*Al/*v*Zr/*u*Ce_HT and *z*Cu/*y*Zn/*u*Ce_ST catalysts, highlight as the composition (in terms of relative amounts of the main active phases and presence of promoters) and the preparation methods can strongly influence the activity of the Cu-based catalysts.

Compared to the commercial catalyst, the Htl samples have shown promising performance, indicating that using hydrotalcites as precursors for Cu-based catalysts can represent an efficient synthesis strategy. Zirconia and ceria were found to favour $CO_2$ conversion and $CH_3OH$ selectivity, respectively, suggesting that by optimizing their relative concentration, a high catalytic activity could be obtained as a result of the synergistic effect between these two components.

As for the ST samples, the preliminary results on the 2Cu/1Ce_ST sample have clearly demonstrated the importance of the promoting effect of ZnO. Unfortunately, the ST method has not been able to guarantee an efficient Cu-Zn interaction, as evidenced by the large size of ZnO particles formed on 2Cu/1Zn/1Ce, thus explaining its poor catalytic activity.

In order to develop new catalytic systems with an improved catalytic performance, a better understanding of the role of zirconia and ceria in the reaction mechanism, as well as in the promotion of textural properties and Cu-dispersion should be attained. Besides further investigation of the catalytic activity in different operating conditions, this also requires additional characterisation of the samples after preparation, reduction pretreatment and catalytic testing.

## *References*

[1]     G.A. Olah, A. Goeppert, G.K.S. Prakash*, Beyond Oil and Gas: the methanol Economy*, WILEY-VHC (2006) Weinheim.

[2]     G.A. Olah, A. Goeppert, G.K.S. Prakash, *J. Org. Chem.* 74 (2009) 487.

[3]     A. Rozovskii, *Russ. Chem. Rev.* 58 (1989) 41.

[4]     M. Saito, T. Fujitani, M. Takeuchi, T. Watanabe, *Appl. Catal. A: Gen.* 138 (1996) 311.

[5]     G. Centi, S. Perathoner, *Catal. Today* 148 (2009) 191.

[6]     V.E. Ostrovskii, *Catal. Today* 77 (2002) 141.

[7]     G. Ertl, H. Knözinger, F. Schüth, J. Weitkamp, *Handbook of Heterogeneous Catalysis*, WILEY-VCH (1997) Weinheim.

[8]     A. Alvarez, A. Bansode, A. Urakawa, A.V. Bavykina, T.A. Wezendonk, M. Makkee, J. Gascon, F. Kapteijn, *Chem. Rev.* 117 (2017) 9804.

[9]     X.-M. Liu, G.Q. Lu, Z.-F. Yan, J. Beltramini, *Ind. Eng. Chem. Res.* 42 (2003) 6518.

[10]    R.G. Herman, K. Klier, G.W. Simmons, B.P. Finn, J.B. Bulko, *J. Catal.* 56 (1979) 407.

[11]    E.L Kunkes, F. Studt, F. Abild-Pedersen, R. Schlögl, M. Behrens, *J. Catal.* 328 (2015) 43.

[12]    G.C. Chinchen, P.J. Denny, J.R. Jennings, M.S. Spencer, K.C. Waugh, *Appl. Catal.* 36 (1988) 1.

[13]    J. Nakamura, T. Uchijima, Y. Kanai, T. Fujitani, *Catal. Today* 28 (1996) 223.

[14]    Y. Choi, K. Futagami, T. Fujitani, J. Nakamura, *Appl. Catal. A: Gen.* 208 (2001) 163.

[15]    J. Szanyi, D.W Goodman, *Catal. Lett.* 10 (1991) 383.

[16]    Y. Kanai, T. Watanabe, T. Fujitani, T. Uchijima, J. Nakamura, *Catal. Lett.* 38 (1996) 157.

[17]    R.A. van Santen, P.W.N.M. van Leeuwen, J.A. Moulijn, B.A. Averill, *Catalysis: An Integrated Approach*, ELSEVIER (1997) Amsterdam.

[18]    J. Tabatabaei, B.H. Sakakini, K.C. Waugh, *Catal Lett.* 110 (2006) 77.

[19]    M.V. Twigg, M.S. Spencer, *Appl. Catal. A: Gen.* 212 (2001) 161.

[20]    R. Burch, S.E. Golunski, M.S. Spencer, *J. Chem. Soc., Faraday Trans.* 86 (1990) 2683.

[21]    F. Arena, G. Mezzatesta, L. Spadaro, G. Trunfio, *Latest Advances in the Catalytic Hydrogenation of Carbon Dioxide to Methanol/Dimethylether. In Transformation and utilization of Carbon Dioxide,* Springer (2014) Berlin.

[22]    L.C. Grabow, M. Mavrikakis, *ACS Catal.* 1 (2011) 365.

[23]    S. Kattel, P.J. Ramirez, J.G. Chen, J.A. Rodriguez, P. Liu, *Science* 355 (2017) 1296.

[24]    J. Wu, M. Saito, M. Takeuchi, T. Watanabe, *Appl. Catal. A: Gen.* 218 (2001) 235.

[25]    C. Baltes S. Vukojevic, F. Schuth, *J. Catal.* 258 (2008) 334.

[26]    H. Jung, H.; D.-R. Yang, O.-S. Joo, K.-D. Jung, *Bull. Korean Chem. Soc.* 31 (2010) 1241.

[27]    H. Fan, H. Zheng, Z. Li, *Front. Chem. Eng. China* 4 (2010) 445.

[28]    P. Gao, F. Li, F. Xiao, N. Zhao, N. Sun, W. Wei, L. Zhong, Y. Sun, *Catal. Sci. Technol.* 2 (2012) 1447.

[29]    S. Kühl, A. Tarasov, S. Zander, I. Kasatkin, M. Behrens, *Chem. Eur. J.* 20 (2014) 3782.

[30]    M. Behrens, S. Kißner, F. Girsgdies, I. Kasatkin, F. Hermerschmidt, K. Mette, H. Ruland, M. Muhler, R. Schlogl, *Chem. Commun.* 47 (2011) 1701.

[31]    G. Prieto, K.P. de Jong, P.E. de Jongh, *Catal. Today* 215 (2013) 142.

[32]    R.A. Koeppel, A. Baiker, A. Wokaun, *Appl. Catal. A: Gen.* 84 (1992) 77.

[33]    Y.W. Suh, S.H. Moon, H.K. Rhee, *Catal. Today* 63 (2000) 447.

[34]    K. Samson, M. Sliwa, R.P. Socha, K. Gora-Marek, D. Mucha, D. Rutkowska-Zbik, J.-F. Paul, M. Ruggiero-Mikolajczyk, R. Grabowski, J. Sloczynski, *ACS Catal.* 4 (2014) 3730.

[35]   T. Witoon, J. Chalorngtham, P. Dumrongbunditkul, M. Chareonpanich, J. Limtrakul, *Chem. Eng. J.* 293 (2016) 327

[36]   R. Raudaskoski, M.V. Niemelä, R.L. Keiski, *Top. Catal.* 45 (2007) 57.

[37]   E. Frei, A. Schaadt, T. Ludwig, H. Hillebrecht, I. Krossing, *ChemCatChem* 6 (2014) 1721.

[38]   L. Li, D. Mao, J. Yu, X. Guo, *J. Power Sources* 279 (2015) 394.

[39]   F. Mei, M. Wei, D.G. Evans, X. Duan, *J. Mater. Chem. A* 4 (2016) 5773.

[40]   J. Graciani, K. Mudiyanselage, F. Xu, A.E. Baber, J. Evans, S.D. Senanayake, D.J. Stacchiola, P. Liu, J. Hrbek, J.F. Sanz, J.A. Rodriguez, *Science* 345 (2014) 546.

[41]   J.J. Yu, Y. X. Tao, C.C. Liu, Z.P. Hao, Z.P. Xu, *Environ. Sci. Technol.* 41 (2007) 1399.

[42]   F. Rouquerol, J. Rouquerol, K. Sing, P. Llewellyn, G. Maurin, *Adsorption by Powders and Porous Solids, Principles, Methodology and Applications*, Second Edition, Academic Press (2014) Amsterdam.

[43]   K.-D. Jung, O.-S. Joo, S.-H. Han, *Catal. Lett.* 68 (2000) 49.

[44]   Y. Zhang, J. Fei, Y. Yu, X. Zheng, *Energ. Conver. and Manage.* 47 (2006) 3360.

[45]   N.F.P. Ribeiro, M.M.V.M. Souza, M. Schmal, *J. of Power Sources* 179 (2008) 329.

[46]   S. Hajduk, V.D.B.C. Dasireddy, B. Likozar, G. Dražić, Z.C. Orel, *Appl. Catal. B: Env.* 211 (2017) 57.

[47]   P. Zimmer, A. Tscho¨pe, R. Birringer, *J. Catal.* 205 (2002) 339.

[48]   F. Mariño, B. Schönbrod, M. Moreno, M. Jobbágy, G. Baronetti, M. Laborde, *Catal. Today* 133-135 (2008) 735.

[49]   X. Guo, D. Mao, G. Lu, S. Wang, G. Wu, *J. Catal.* 271 (2010) 178.

[50]   S. Zhang, W. Huang, X. Qiu, B. Li, X. Zheng, S. Wu, *Catal. Lett.* 80 (2002) 41.

[51]   X. Tang, B. Zhang, Y. Li, Y. Xu, Q. Xin, W. Shen, *Catal. Today* 93-95 (2004) 191.

[52]    T.N. Afonasenko, P.G. Tsyrul'nikov, T.I. Gulyava, N.N. Leont'eva, N.S. Smirnova, D.I. Kochubei, O.O. Mironenko, D.A. Svintsitskii, A.I. Boronin, Y.S. Kotolevich, E.A. Suprun, A.N. Salanov, *Kinet. Catal.* 54 (2013) 59.

[53]    G. Bonura, F. Arena, G. Mezzatesta, C. Cannilla, L. Spadaro, F. Frusteri, *Catal. Today* 171 (2011) 251.

[54]    F. Arena, G. Mezzatesta, G. Zafarana, G. Trunfio, F. Frusteri, L. Spadaro, *J. Catal.* 300 (2013) 141.

# *Conclusions and Perspectives*

In this thesis, three different processes aimed at the conversion of $CO_2$ to cyclic carbonates, methane, and methanol were studied. For each process, suitable solid catalysts were synthesised, extensively characterised, and used in order to study their catalytic properties in different reaction conditions.

Imidazolium-based catalysts were prepared by a one-pot immobilisation procedure by using three Al-SBA-15 supports having different Si/Al molar ratios. Characterisation results clearly showed that functionalisation was successfully performed, and that the imidazolium amount increased along with the Al content. All the prepared materials were found highly active in the conversion of both epichlorohydrin and styrene oxide, showing very high TON values at all the investigated reaction conditions. However, further studies, focused on a better understanding of the influence of both the Si/Al molar ratio and the functionalisation degree on the catalytic performance, are necessary. For this purpose, new catalytic tests have to be performed on ad-hoc synthesised Imi-catalysts. Unlike styrene oxide, epichlorohydrin was found to favour the detachment of the imidazolium moieties more weakly bonded to the supports; however, leaching phenomena were observed to occur only during the first catalytic run, showing that the prepared catalysts can be used in multiple catalytic cycles. In light of the good results obtained so far, additional catalytic tests should be performed in a wider range of reaction conditions, in order to evaluate the suitability of these materials to be used in industrial applications.

$CO_2$ methanation was studied on $NiO/CeO_2$ mixed oxides, prepared by using two different unconventional synthesis procedures. A first series was prepared by using the "*Hard-Template*" method, while the second one was obtained by means of the "*Soft-Template*" strategy. All the prepared catalysts were found very active and selective toward methanation. The pivotal role of ceria both as promoter and active component was clearly observed; in fact, besides to improve the reducibility and the dispersion of NiO species, ceria is also responsible for the activation of $CO_2$ through the formation of oxygenated intermediates. In addition, the presence of strong Ni-Ce interactions was found to be crucial in ensuring a high catalytic performance also in unfavourable reaction conditions. Indeed, only the highly uncoordinated

Ni atoms at the metal-support interface, whose number depends on the mean particle size, are able to activate the $H_2$ required to reduce $CO_2$ activated on the nearby ceria sites. Currently, work is in progress to study the catalytic behaviour of the Soft-Templated $NiO/CeO_2$ samples in the simultaneous hydrogenation of $CO_2$ and CO to methane, with the aim of evaluating their versatility for different $CO_2$ sources and syngas compositions.

CO₂ hydrogenation to methanol was studied by using two different series of Cu-based catalysts, prepared by using hydrotalcitic precursors and the "*Soft-Template*" approach, respectively. The influence of different supports and promoters such as ZnO, $Al_2O_3$, $ZrO_2$, and $CeO_2$ on the catalytic performance was investigated. Promising catalytic results were observed by using the catalysts obtained by the hydrotalcitic precursors. Zirconia and ceria were found to favour $CO_2$ conversion and $CH_3OH$ selectivity, respectively, suggesting that a synergistic effect could be obtained by optimizing their concentrations. Although not satisfactory, the catalytic results obtained by using the Soft-Templated Cu-based samples confirmed the crucial role of efficient Cu-ZnO interactions in determining a high catalytic performance. In view of the above, a more in-depth study of the role of zirconia and ceria in the reaction mechanism, as well as in the promotion of textural properties and Cu dispersion, is necessary. It will allow the development of new materials with improved catalytic activity through the optimization of their composition and the identification of the most appropriate synthesis strategies to maximize the synergistic effect between the different components.